Eindhoven University of Technology

MASTER

Ammonia release from fast pyrolysis of MDF

van de Garde, J.L.B.

Award date:
2006

Link to publication

Ammonia release from fast pyrolysis of MDF

J.L.B. van de Garde
Supervisor: dr.ir. M.J. Prins

University of Technology of Eindhoven
Faculty of Mechanical Engineering
Division Thermo Fluids Engineering
Section Combustion Technology

Abstract

Transition to sustainable energy resources will be necessary in the future, both because fossil fuel reserves are dwindling and out of an environmental viewpoint. Biomass could be a good alternative for electricity generation, for example in grate furnaces.

For finding the optimal operating conditions of a grate furnace for a wide range of fuels, models are needed that predict the formation of NO_x and NO_x precursors. The current models do not suffice, as their results do not match the measurements done on a real grate furnace under similar conditions. To improve the models, accurate measurements are needed.

The pyrolysis product gas needs to be produced under controllable conditions. Therefore, a set up has been built which uses a heated grid reactor. This stainless steel reactor houses a metal wire mesh, which can be heated up by passing a current through it. The power source is software controlled, which enables accurately setting of heating up rate, final temperature and hold time. For measuring the gas composition, a Perkin Elmer Spectrum GX dual source FTIR spectrometer is used.

With the set-up built for this project such accurate measurements under controlled conditions are possible. The varying pyrolysis conditions and the fuels that have been pyrolysed allow for first order estimation of the release rate of ammonia. For both MDF and urea an increase in ammonia yield with increasing temperature is observed, up to a temperature where the yield reaches a maximum. The highest achieved yield was at 800^OC for MDF and at 700^OC for urea. Decrease in ammonia yield may be explained by thermal decomposition of ammonia, formation of NH_i radicals by pyrolysis of ammonia, the presence of catalytic effects of nickel or by secondary reactions which consume ammonia.

A simple first order model, proposed by D.B. Anthony, et al. is given by

$$\frac{dV}{dt} = k(V^* - V),$$

with V the volatiles release at time t, and V^* the amount of volatiles released at time t = ∞. The model parameters which give acceptable results are a maximum ammonia yield V^* of 0.25 wt%, an activation energy E of 153 [kJ/mol] and an apparent frequency factor k_0, also known as pre-exponential factor, of 7×10^7 [1/s]. The value for the activation energy is actually for ammonia release from *Miscanthus Giganteus* under slow pyrolysis conditions [30], but the results for ammonia release from MDF seem to be acceptable.

Contents

Chapter 1   Introduction

§1.1   Background

The roots of the modern environmental movement may be traced to attempts in late nineteenth century Europe and North America to expose the costs of environmental negligence and widespread air and water pollution. Only after the Second World War a wider awareness emerged, especially with the 1972 report "Limits to Growth" [1] by the Club of Rome and the 1987 report by the Brundtland Commission, "Our common future" [2]. The definition of sustainable development given by the Brundtland Commission says that "Sustainable development is development that meets the needs of the present without compromising the ability of future generations to meet their own needs." This means, for example, that natural resources may not be depleted. The current use of fossil fuels is a good example of non-sustainable development: resources are being depleted, and on top of that there is an increased greenhouse effect, imbalancing the climate.

With dwindling fossil fuel reserves and changing climate, the need for sustainable energy resources is evident. One such a resource could be biomass. Biomass is part of the short carbon cycle, which means that carbon that is emitted by conversion of biomass was chemically bound in that biomass not so long ago. This makes biomass a CO_2-neutral resource in that it does not raise the CO_2 level in the atmosphere. By contrast, the carbon emitted by conversion of fossil fuels was bound millions of years ago and the climatic balance that was established afterwards is now being threatened by our release of this carbon in a very short time span, by causing an increased greenhouse effect.
Biomass encompasses a very broad spectrum of organic materials, from wood to grasses, from manure to municipal waste. Some material streams from industry can also be considered as biomass, and when such a stream is considered waste by the industry, this stream could be used as a low cost fuel for generating electricity and heat.

Biomass as a fuel has been subject of intensive study since it became clear to a wide audience around the 1970's that the Earth has finite resources and we need to take care of what we do with those resources and to the Earth. One of the problems that have not yet been tackled, is the emission of nitrogen- and nitrous-oxides (called NO_x) from biomass power plants. At high temperatures NO_x can be created from nitrogen in the air that is used for combustion. However, due to the relatively low temperatures in biomass combustion the NO_x emissions are mainly created by formation of ammonia and hydrogen cyanide from the nitrogen that is chemically bound in the fuel, the so called fuel-NOx, in the decomposition step of the combustion process. Most of the NOx emission consists of NO, which reacts to NO_2 in the atmosphere and can then further react with water to form nitric acid, HNO_3, which causes acid rain. NO_2 can undergo photochemical reaction with volatile organic compounds in the atmosphere to form smog, and N_2O is a direct greenhouse gas.

§1.2   Research objectives

The emission of NO_x is bound to certain upper limits by legislation. Because of the adverse characteristics of these emissions and the growing global demand for energy, these limits will probably go down in the future which makes it more difficult to meet the requirements. Because

of this, research is done in a European project by several partners, such as the Eindhoven University of Technology TU/e and Graz University of Technology TUG. The main objective of the so called OPTICOMB (OPTImization and design of biomass COMBustion systems, [3]) project is to increase the flexibility of biomass combustion plants with respect to the fuel input and to reduce their harmful emissions. Within the OPTICOMB project one of the tasks assigned to the TU/e and TUG is to characterise NO_x precursors from the biomass fuel layer.

In general, combustion is a complex phenomenon with al kinds of processes taking place simultaneously. This is even more true for biomass, because biomass is basically a mix of components that all have their own properties. The problem at hand is that emissions that are being measured in experiments do not agree with those calculated in simulations with the current models for NO_x formation. One down side of the current models is that they assume that the char that remains after the decomposition process, also known as pyrolysis, consists of carbon only, which is only true for the extreme case of carbonization. More often other substances will also be left in the char, such as oxygen and some nitrogen. To improve these models, accurate measurements under known conditions are needed. From these measurements the necessary model parameters may be obtained. The model presented by D.B. Anthony, et al. for rapid devolatilization of coal [4] may be suited for biomass too.
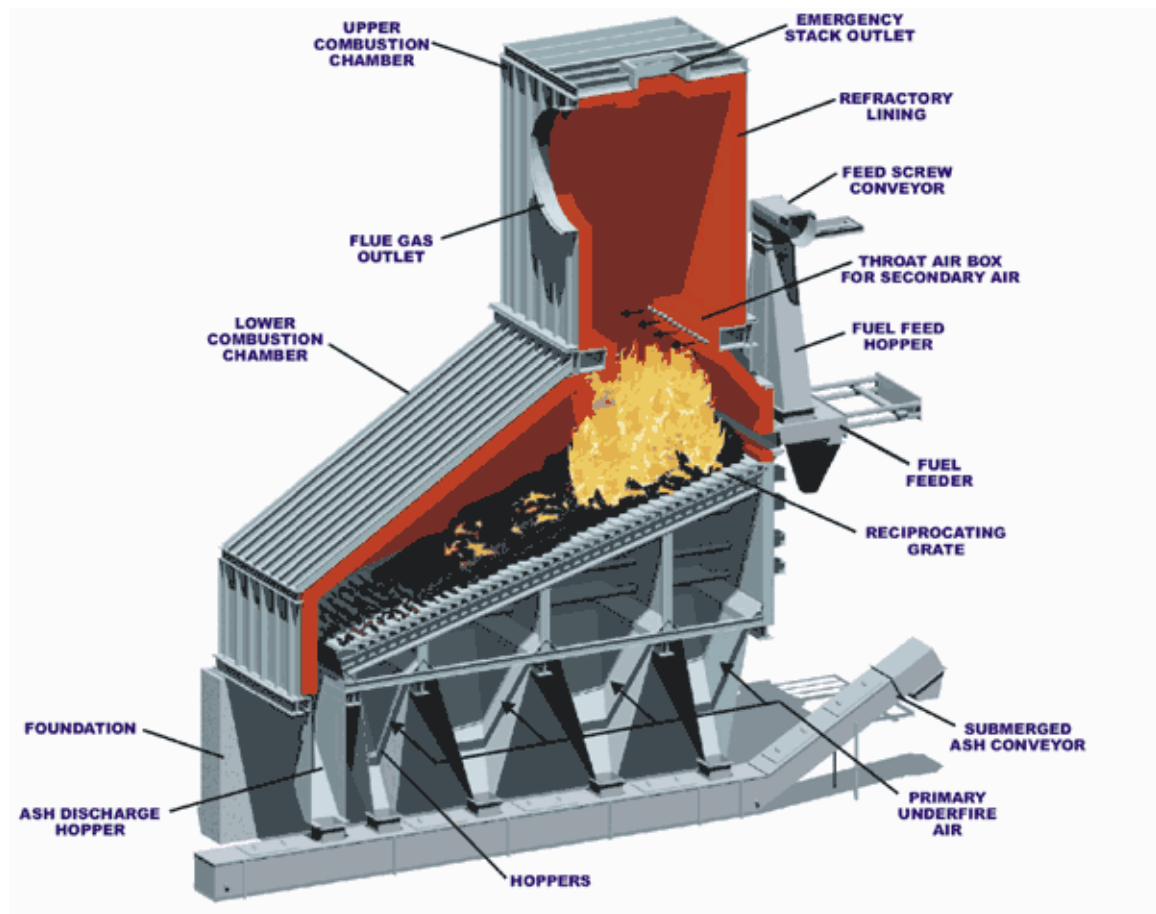

Figure 1.1: Cross sectional view of a grate furnace, current state of art in biomass conversion. [5]

The goal of this project is to

> *Determine ammonia (NH₃) release rates from biomass, by offline measurement of ammonia in biomass pyrolysis product gas using FTIR.*

The pyrolysis product gas can be created under varying conditions so that the determined release rate is applicable to a broad range of pyrolysis conditions. The release rates can be used for the pyrolysis sub-model in 3D CFD of thermal processing equipment for the OPTICOMB project.

§1.3 Approach

This project is the continuation of previous research by M. Geurds [6]. He studied slow pyrolysis of biomass using a tube furnace. One of the problems with slow pyrolysis is that the products that are formed and their quantities differ from those formed during fast pyrolysis. Since it is fast pyrolysis that takes place in biomass power plants it is only natural, keeping the OPTICOMB project in mind, to study fast pyrolysis. For this reason the tube furnace that was used before is replaced with a so-called heated grid reactor. The grid reactor is a stainless steel reactor with a metal grid inside. This grid is heated up by means of passing an electric current through it. This enables the accurately setting of heating rate and final temperature, and much larger heating rates can be studied, in the order of 1000K/s in stead of a few K/s which is typical for the tube furnace. With a heated grid reactor the weight loss of a sample during the heating up period is much smaller, and reaction kinetics can be studied much better.

A well known methods for determining a gas composition is Fourier transform infra red spectroscopy (FTIR). This method uses an infra red (IR) source and modulates the IR beam using a beam splitter, one fixed mirror and one moving mirror. The beam then passes through the gas to be measured. Certain frequencies of the IR beam will be absorbed by the gas molecules while other frequencies are not. The absorption of certain frequencies gives information on the components in the gas. The expected amounts of ammonia in the pyrolysis product gas are in the order of several hundred parts per million, ppm. For accurate measurements it is therefore important to measure the absorption peaks of ammonia at the frequencies where their absorption is strongest. Another problem that M. Geurds had was that he could not perform the gas composition measurements in that range. Due to the material of the beam splitter so much of the IR beam was absorbed below a certain frequency that accurate measurements were no longer possible. Therefore, the beam splitter was replaced by one of a different material which enables measurement in the optimal region for ammonia.

In this report the pyrolysis process and relevant related topics are discussed in chapter 2. In chapter 3 the FTIR measuring device and its principles are treated, and a way to theoretically determine an absorption spectrum is presented. Chapter 4 deals with the set-up that is used for the experiments and describes the method used for the measurements. The results of the experiments are presented and discussed in chapter 5, and finally chapter 6 summarises the conclusions and gives recommendations for future work.

Chapter 2   Biomass pyrolysis

§2.1   Definition

The process of pyrolysis is usually defined as the devolatilization or decomposition of a substance under the influence of heat in an inert, i.e. oxygen free, atmosphere. What remains after decomposition is a certain amount of char and, depending on the exact circumstances under which pyrolysis took place, more or less condensable and non-condensable gases of varying composition. The most important parameters that determine which products are formed and in what amounts are the type of fuel used and the pyrolysis temperature, but heating rate, particle size and surrounding pressure also play a role.

§2.2   What is biomass?

The term biomass comprises a large group of substances which can be narrowed down by defining biomass as all plant-like matter. With this definition substances such as manure are not considered, and to a certain extent all plant-like matter has the same composition, which makes it easier to work with this definition.

Biomass has three main components, namely cellulose, hemicellulose and lignin. Cellulose is a linear polymer with a degree of polymerization (DP) of up to 10,000 six-carbon anhydroglucose sugar units. Hemicelluloses are chemically similar to cellulose but consist of 100 to 200 heterogeneously linked six-carbon and five-carbon anhydro sugars. Lignins appear to be primarily random, three dimensional polymers of 4-propenyl phenol (p-coumaryl alcohol), 4-propenyl-2-methoxy phenol (guaicyl alcohol) and 4-propenyl-2,5-dimethoxy phenol (syringyl alcohol). The ratio of these phenols depends on which plant species is considered and its environmental conditions [7].

The three main components of biomass, i.e. cellulose, hemicellulose and lignin, are known to consist of hydrogen, carbon and oxygen atoms only. So, if the biomass would consist of these three main components only, there would be a much smaller NO_x problem because there is no nitrogen in the biomass. Unfortunately there is always some nitrogen in biomass, for example in the form of chlorophyll and amino acids, from less than 0.1 wt% for most woods to about 4 wt% for some peats [8,9], which will always lead to NO_x precursor formation (HCN and NH_3) and eventually NO_x itself.

§2.3   Pyrolysis of biomass

In the Western world it is difficult to imagine nowadays that mankind has not always fulfilled its demand for energy with fossil fuels. It is sometimes said that fire is the cornerstone of civilization. Whether or not this is true may be debated, but gaseous and liquid (fossil) fuels certainly have become the foundation of our age of technology. Many processes that are used commonly now would be impossible without refined fuels, and all processes would be less efficient, less convenient and more polluting. Probably civilization will survive the exhaustion of fossil fuels in one form or another, but modern technology will be crippled unless we find a substitute [10].

Using biomass as an energy source can hardly be called a new idea. Mankind has used wood for heating and preparing food since its dawn and an estimated one third of the global population still does so. During the Second World War, when fossil fuels were scarce and hard to come by all over Europe, gasification of biomass was used to generate the fuels needed to operate vehicles [10].

Pyrolysis takes place under inert conditions, but even in combustion or gasification of biomass the pyrolysis process plays a very important role. This is because the heat generated by combustion or gasification is partly conducted into the fuel and there heats up the fuel in the absence of oxygen, resulting in pyrolysis of the fuel.

The products of pyrolysis of biomass can be divided into three groups, namely gases, tar and char. The exact amounts will differ for different kinds of biomass and the exact conditions under which pyrolysis took place. A semi-global mechanism that is commonly used for describing the products formed by decomposition of one of the main components of biomass, namely cellulose, is the modified Broido-Shafizadeh mechanism [11],

$$CELLULOSE \begin{array}{c} \overset{k_1}{\nearrow} TAR \\ \underset{k_2}{\searrow} \nu_C CHAR + \nu_G GAS \end{array} \qquad (2.1)$$

The two parallel competitive reactions have reaction rates k_1 for tar formation (which, for cellulose, consists mainly of levoglucosan) and k_2 for char and gases formation. These reaction rates are dependent on the pyrolysis conditions, and experiments can be carried out to obtain these reaction rates.

Under different pyrolysis conditions the biomass will behave differently. Slow, fast and flash pyrolysis can be distinguished. Under slow pyrolysis conditions, with heating rates of around 1 K/s, and residence times ranging from several minutes or hours to days, three zones can be seen in the weight loss versus time graph. This graph is also called thermo gravimetry (TG) graph and is depicted in figure 2.1 for black walnut. When heating up commences, first the biomass is dried causing an initial weight loss. Than around 200^OC the first decomposition zone starts with the devolatilization of the hemicelluloses. When the temperature reaches 300^OC most of the hemicelluloses have disappeared, as can be seen from the derivative thermo gravimetric (DTG) graph. The second zone is ascribed to cellulose for temperatures between 300^OC and 350^OC, this is where the DTG graph has a maximum due to the small temperature range of cellulose decomposition. Finally, lignin decomposes gradually over the range of 250^OC to 500^OC, which accounts for the last part of the graph before only char and ash remain.

Fast pyrolysis operates with higher heating rates, up to 10,000K/s and typically has a shorter residence time of up to a couple of seconds. Because of the increased heating rate it becomes more difficult to distinguish between the three decomposition zones for hemicellulose, cellulose and lignin mentioned earlier. Fast pyrolysis best characterizes the processes in a typical biomass grate furnace, although in the case of a grate furnace the secondary reactions that may occur after the initial pyrolysis step will also have an influence on the final product yield.

Flash pyrolysis operates at heating rates upward of 10,000K/s. The residence time is typically one second or less. Although the reaction products formed may be similar to those formed in fast and slow pyrolysis of the same biomass, their yields differ a lot.

The exact composition of biomass pyrolysis product gas depends on the type of biomass used, the heating rate and coupled to that the particle size, the final pyrolysis temperature, the hold time (i.e. the amount of time the biomass is held at the final temperature) and the ambient pressure.
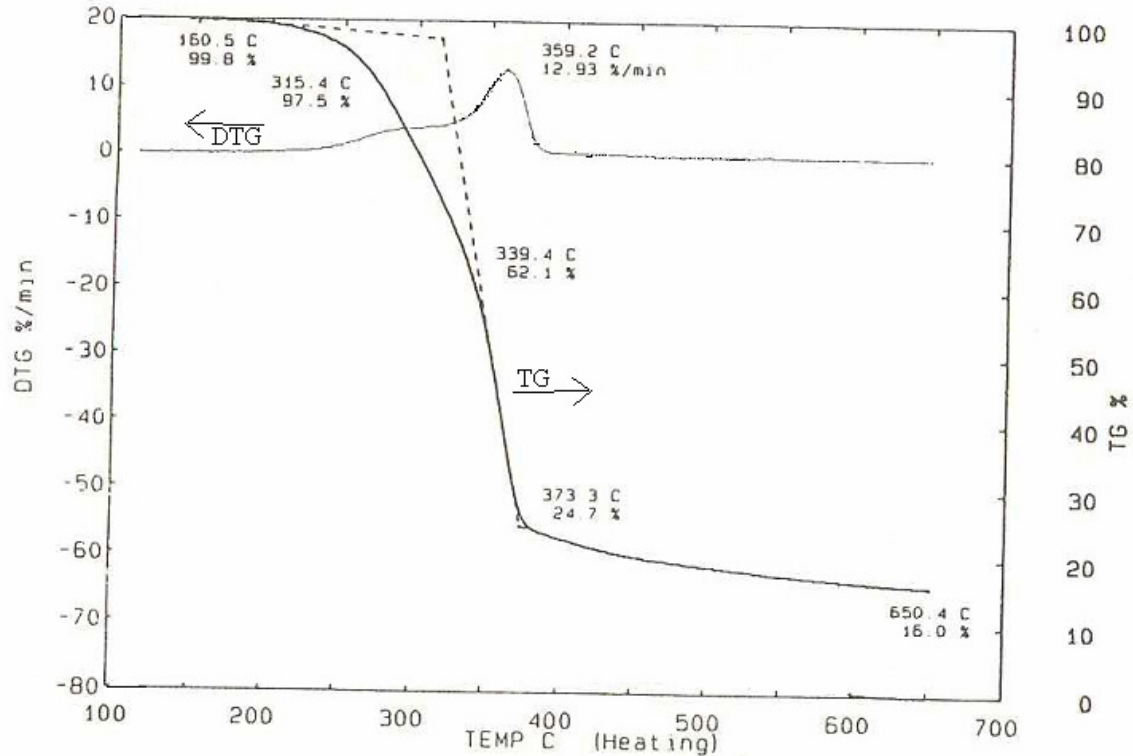
Figure 2.1: Typical weight loss graph (TG, right vertical axis) for black walnut (*Juglans Nigra,* hardwood) under slow heating conditions. Also shown is the derivative thermo gravimetric graph (DTG), which shows the weight loss in percentage per minute (left vertical axis). Picture from "*Thermal data for natural and synthetic fuels*", by S. Guar and T.B. Reed, (1998).

§2.4 NO$_x$ formation mechanism

Emission of nitrogen oxides and nitrous oxide from industrial processes and power plants is a major environmental concern. The NO$_x$ emissions are created by either fixation under very high temperatures of nitrogen from the combustion air or by oxidation of nitrogen that is chemically bound in the fuel.

Common solid fuel combustion technologies are pulverized fuel combustion (PFC), combustion on grates (GC) and fluidized bed combustion (FBC). In for instance pulverized coal burning equipment low NO$_x$ emissions are achieved by means of using low-NO$_x$ burners or over-fire air injection, by injection of a reducing agent which causes selective non-catalytic reduction of NO or reburning, or by catalytic flue gas cleaning. However, these methods may not be viable for biomass, which is often burned on a grate. GC methods, and also FBC methods, preclude the use of low-NO$_x$ burners. Trace components such as alkali metals in the flue gas also render the use of catalytic deactivation inapplicable [9].

Thermal NO$_x$ formation
When molecular nitrogen in the combustion air is fixated by means of the high temperatures involved in the combustion process this is called thermal NO$_x$ formation. The reactions proceed as follows:

8

$$O + N_2 \Leftrightarrow NO + N \tag{2.2}$$
$$N + O_2 \Leftrightarrow NO + O \tag{2.3}$$
$$N + OH \Leftrightarrow NO + H \tag{2.4}$$

The activation energy of the reaction 2.2 is very high and formation of thermal NO is most important at temperatures above 1800K [9]. In typical biomass combustion processes this temperature will not be reached and the contribution of thermal NO to the total NO_x yield is considered very small.

Prompt NO_x

The exact path of formation of NO_x by the mechanism called prompt NO_x is not yet known, but it seems to be initiated by the attack of the CH radical on the N_2 triple bond [9]. The reactions that occur are

$$CH + N_2 \Leftrightarrow NCN + H \, , \tag{2.5}$$

and for the N_2O mechanism

$$O + N_2 + M \Leftrightarrow N_2O + M \, . \tag{2.6}$$

Dependent of the reaction conditions, the reactive nitrogen compounds that are formed (NCN and N_2O) may be oxidized to NO or be recycled to N_2. The amount of prompt NO_x that is formed also seems to increase with temperature, so for typical biomass combustion processes the effect of prompt NO_x is also thought to be small.

Fuel NO_x

As already mentioned in paragraph 2.2 all biomass contains some amount of nitrogen. More generally it can even be said that all solid fuels contain some organically bound nitrogen, with a few exceptions such as plastic waste. Formation of NO by oxidation of this fuel nitrogen is called fuel NO_x. The overall sequence of reactions is fairly well known, starting with a distribution of fuel-N between volatiles and the char matrix when particle combustion commences. The distribution of nitrogen between char and volatiles, and also the volatile nitrogen composition, depends mainly on the fuel structure and the temperature. For biomass, light nitrogen species (HCN and NH_3) may be emitted from the solid matrix directly. Hydrogen cyanide (HCN) is then oxidized to NO via intermediate amines (compounds derived from ammonia by replacing hydrogen atoms by organic substituents, such as univalent hydrocarbon radicals) or, depending on stoichiometry and fuel-N concentration, converted to N_2 by the recombination of NO with another nitrogen containing species.

Char-N and soot-N may undergo heterogeneous oxidation to form NO and N_2 or it may evolve as light components, such as HCN, under high temperatures. Nitric oxide (NO) may be recycled by hydrocarbon radicals to cyanide or reduced to N_2 by surface reactions on char or soot.

At low temperatures other nitrogen species are detected in the gas phase in significant amounts. Besides HCN, also ammonia (NH_3) and cyanuric acid (HNCO) are released during pyrolysis. The source for NH_3 is presumably the direct cleavage of amino groups and amides. Under these conditions conversion of fuel nitrogen to N_2O may be significant and char-N may contribute too, but the most important source of N_2O appears to be oxidation of HCN [9].

9

§2.5 Model

The goal of this project is not to accurately determine the NO_x formation mechanisms that occur in pyrolysis of biomass, but to find a model that can predict the yield of ammonia from MDF under certain conditions. Therefore the pyrolysis process itself is considered as a black box, and only what goes in, what comes out and the pyrolysis conditions are of interest. The yield from pyrolysis of biomass is mainly dependent on type of biomass used, final pyrolysis temperature, heating rate and hold time. The exact quantities of substances formed during pyrolysis also appear to be influenced by the surrounding pressure and the size of the biomass particles [4]. Ambient pressure during pyrolysis experiments will be atmospheric, similar to that inside a grate furnace. The fuel used will be in powder form, so the particle size is very small in the order of 0.1mm or smaller. Powdered fuel raises the limits of mass and heat transfer inside the fuel, so that the pyrolysis is as close to ideal pyrolysis as possible. For improving biomass power plants and finding their optimum point of operation, models representing this process as accurately as possible are needed. Even though developing this model is not the goal of this project, it is important to keep this model in mind because it is the ultimate goal supported by this project.

Even though reference [4] is actually about devolatitlization of coal, the model developed in this article is thought to be a usable first order approximation for biomass too. The exact process of pyrolysis is complex and it may not be possible to model it exactly. From a limited set of experiments, attempts have been made to correlate devolatilization rates with a first order expression,

$$\frac{dV}{dt} = k(V^* - V).$$ (2.7)

In equation 2.7, V is the mass of volatiles per mass of original biomass, evolved at time t. V^* is the value of V at time t = ∞. Rate constant k is assumed to have an Arrhenius form,

$$k = k_o \exp(-E / RT),$$ (2.8)

where E [kJ/mol] is the activation energy, k_o [1/s] is the apparent frequency factor, R [kJ/K mol] is the ideal gas constant and T [K] the absolute temperature.

Correlations such as equation 2.7 are usually only applicable to the limited range of the experiments they are correlating for, and finding one general set of parameters that describe results of an arbitrary test well is very difficult. For a given set of conditions, values of k may vary by several factors of 10, and E may vary from several kJ/mol to 200 kJ/mol [4]. The requirement of different values for k_o and E for each set of experimental conditions is the main weakness of this first order model.

In biomass that is subjected to pyrolysis, numerous independent chemical reactions take place. These reactions presumably result from the different molecules in biomass as well as their different temperature responses. Similar to equation 2.7 the reaction of a single organic species can typically be described by a simple first order irreversible reaction. For a particular reaction i, this equation can be written as

$$\frac{dV_i}{dt} = k_i (V_i^* - V_i).$$ (2.9)

From this equation the as yet unreleased volatiles can be obtained by integration of the equation and rewriting. First, rewriting gives

$$dV_i = k_i(V_i^* - V_i)dt \leftrightarrow \frac{dV_i}{(V_i^* - V_i)} = k_i dt \;. \tag{2.10}$$

Than, integrating both sides of the above equation gives

$$\int_0^V \frac{1}{(V_i^* - V_i)} dV_i = \int_0^t k_i dt \;. \tag{2.11}$$

In equation 2.11, the limits of the time integral on the right hand side are from time $t = 0$ to arbitrary time t, with $t>0$. At time $t = 0$, there are no volatiles released yet, so the lower bound on the integral on the left hand side of the equation is 0. At time t there is an amount V_i of volatiles released from the biomass, so this is the upper bound. Working out the integral on the left hand side results in

$$\left[-\ln(V_i^* - V_i)\right]_0^V = \int_0^t k_i dt \;. \tag{2.12}$$

Substituting the values of the integral gives

$$-\ln(V_i^* - V_i) + \ln V_i^* = \int_0^t k_i dt \;. \tag{2.13}$$

With some basic calculus rules for logarithms, this becomes

$$\ln\left(\frac{V_i^*}{V_i^* - V_i}\right) = \int_0^t k_i dt \;, \tag{2.14}$$

which can be rewritten to

$$\ln\left(\frac{V_i^* - V_i}{V_i^*}\right) = -\int_0^t k_i dt \tag{2.15}$$

Taking both sides as an exponent and rewriting finally results in

$$V_i^* - V_i = V_i^* \exp\left(-\int_0^t k_i dt\right) \tag{2.16}$$

The term in brackets still holds a time integral because the rate constant is a function of the time-temperature history. This derivation holds for one species only, in this case ammonia, but can be extended to encompass any number of parallel reactions. In Appendix A this extension of the model is made.

Chapter 3   Infra red spectroscopy

Among the numerous methods that can be used for determining a gas composition, the methods called infra red spectroscopy may be the easiest and fastest to work with. With this measuring method the interferogram collected by the spectrometer is changed into an absorption spectrum by Fourier transformation, hence the name Fourier Transform Infra Red spectroscopy (FTIR). In this chapter, first the working principles of infra red (IR) absorption and IR spectroscopy are briefly discussed, as well as the spectrometer itself. Beer's law is briefly treated because this is important for quantitative analysis, and finally calculation of an absorption spectrum is presented.

§3.1   Absorption spectra

The reason that the infrared part of the spectrum is used for FTIR measurements is that most molecules can absorb energy in that range of wavelengths, roughly between 750 nm and 1mm. At temperatures above absolute zero all molecules have a vibrating and rotating behaviour. Molecules vibrate at frequencies of approximately 10^{14} cycles per second, and they rotate at frequencies of approximately 10^{11} cycles per second, which roughly corresponds to the frequencies found in the infrared part of the spectrum. [12]
Radiation is able of interact with a molecule when the radiation frequency is equal to one of the eigenfrequencies of the molecule, and when the particle has an electric moment. In practice, this means the particle has to have a dipole moment. Dipole moment is defined as the magnitude of electric charge of two opposite charges, multiplied by the distance between them. When the electrons of a molecule are drawn more strongly to certain atoms than to others, the electrons are divided unequally over the molecule. If this is the case, the molecule is said to be polarised. A polarised molecule is able to absorb a photon of the right frequency, which will then change the dipole moment of the molecule by changing the distance between the charges, e.g. by stretching (changing bond length), bending (changing bond angle), rocking, twisting or wagging. Figure 3.1 illustrates some of these vibration/rotation changes. In this example only oxygen atoms (O) and carbon atoms (C) are depicted, but the names for the vibrations and rotations apply to any couple of atoms.

Homonuclear diatomic molecules, i.e. molecules consisting of two exactly the same atoms such as nitrogen, oxygen and hydrogen, have a charge distribution that is symmetrical about their centre of mass. Hence, homonuclear molecules at normal pressure do not absorb photons, and show no pure vibration or rotation spectrum.
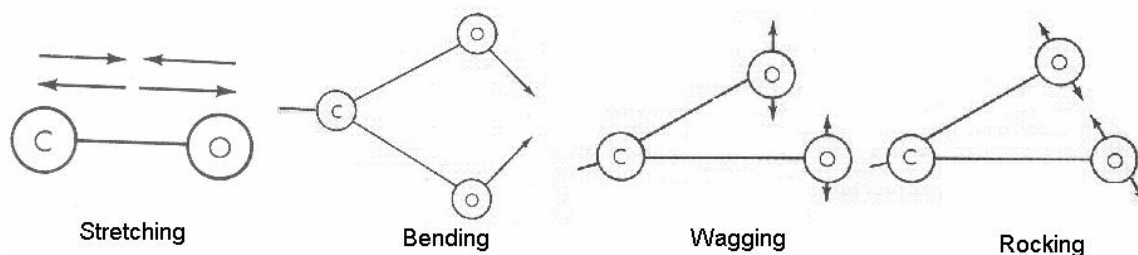

Figure 3.1: Illustration of various vibrational and rotational modes, arrows indicate atom direction of movement [12].

Since different molecules are composed of different atoms they will have different absorption spectra. The location of absorption lines in the spectrum of a molecule depends on the number of atoms in a molecule, which atoms exactly are in the molecule because different atoms have different mass, and the vibrational/rotational state the atoms are in. When there are more atoms in a molecule, there are more bonds between atoms which means there may be more different wavelengths of radiation at which absorption can occur. When looking at an absorption spectrum, for example the one in figure 3.2, it is clear there are regions with absorption and regions without absorption. An absorption band is a wavelength region with absorption, starting from zero absorption and ending at zero absorption. From figure 3.2 it can be seen that hydrogen cyanide (HCN) has three bands in the wavenumber range 500 to 4000 cm^{-1}: the first band is roughly from 600 to 800, the second band from 1300 to 1450 and the third band from 3200 to 3400. This graph has been made with data from the software programme JavaHAWKS. More on computing an absorption graph from the spectral intensity data given by JavaHAWKS can be found in paragraph 3.4.

The reason there are three different bands in figure 3.2 is due to the vibrational levels of the HCN molecule, since the energy differences between vibrational levels are so large. These large vibrational transitions determine the location of the centre of an absorption band. The energy differences in rotational levels are much smaller and appear as fine structure around the vibrational frequency transitions. The absorption lines on the lower wavenumber side of a vibrational transition frequency are called the P-branch, the lines on the upper wavenumber side are called the R-branch [13]. The high peak in the centre of the 600-800 cm^{-1} band is called the Q-branch and is much higher because at this frequency the molecule can undergo rotational transitions without simultaneous vibrational transitions, causing a superposition of all rotational
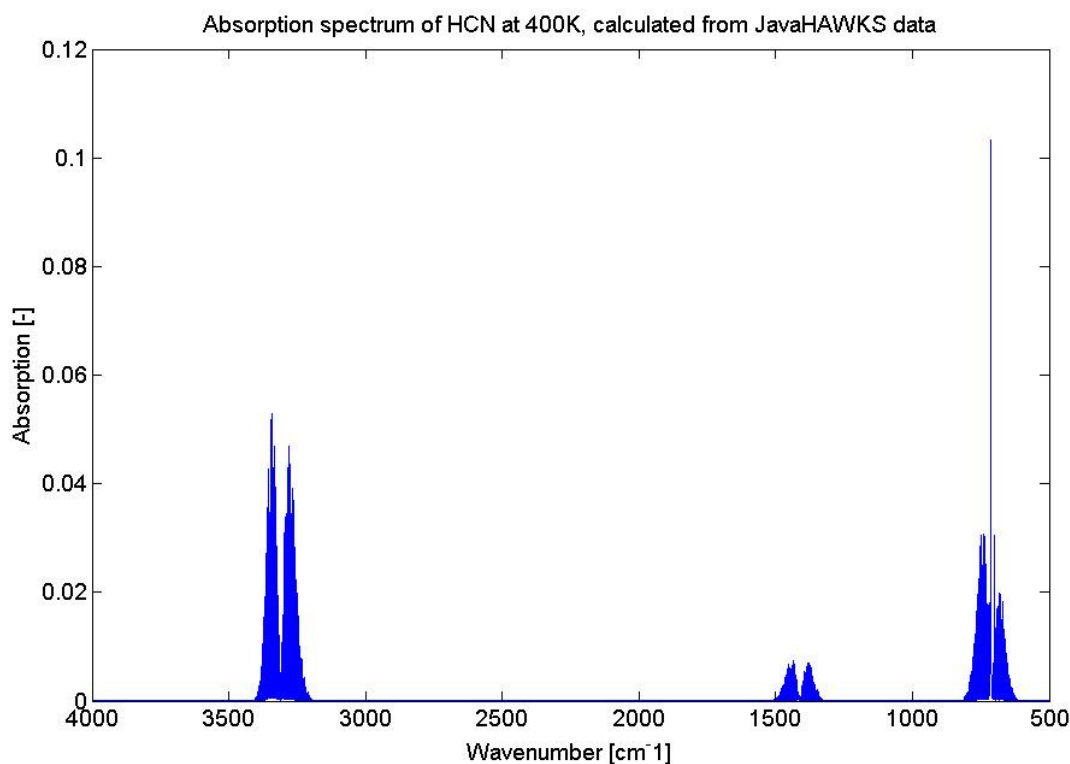

Figure 3.2: Hydrogen cyanide absorption graph (concentration of 200 ppm), calculated from JavaHAWKS [14] spectral line intensity data.

transitions which finally leads to the high absorption peak. More on these branches can be found in Appendix B. Because of the relatively large scale of the graph in figure 3.2 it is difficult to see, but if one were to zoom in on one of the absorption bands the separate absorption lines corresponding to rotational transitions are clearly visible, see figure 3.3.

Another reason an absorption graph looks the way it does is that the presence of different isotopes of the same molecule will show absorption lines around the most abundant isotope. The other isotopes will be present in smaller amounts, so their absorption lines will be smaller, and since their atoms are heavier or lighter they will appear next to the stronger line of the most abundant isotope.

The horizontal axis of figure 3.2 displays wavenumber in units of cm^{-1}. Wavenumber is defined as the number of waves that electromagnetic radiation has in one centimetre. The following equation can be used for conversion between wavelength λ [m] and wavenumber υ [cm^{-1}],

$$\upsilon = \frac{1}{100 \cdot \lambda} \ . \tag{3.1}$$

When for example radiation of wavelength 100μm is considered, the wavenumber is 100 cm^{-1}. The energy of a photon is given by

$$E_{ph} = \frac{h \cdot c}{\lambda} , \tag{3.2}$$

with h the Planck constant ($6.63*10^{-34}$ [m^2kg/s]) and c the speed of light (299 792 458 [m/s]). As equations 3.1 and 3.2 show, a good reason to use wavenumber instead of wavelength for plotting the absorption graph is that wavenumber is proportional to the photon energy whereas wavelength is inverse proportional.

When the temperature of the gas under consideration is changed, the number of molecules in an excited state will also change. This will give rise to more or less absorption at a certain wavenumber where the molecule absorbs radiation. However, when all absorption bands of a particular molecule are considered, the total area underneath the contour of all those bands will stay equal provided that the concentration of species under consideration does not change with temperature. Because of this, FTIR can be a very suitable method for determining the composition of a gas when the temperature of that gas is not necessarily homogeneous.

Theoretically the absorption spectrum of a molecule should consist of sharp lines at certain wave numbers, corresponding to photon energies that may change the dipole moment of a molecule. In practice however, absorption lines are broadened. This broadening can be caused by collisions and mutual interactions between molecules, the finite lifetime of molecules in the excited state or by Doppler effect of thermal motion of the molecules. Of these three causes, collision broadening is the most important one at normal pressures and temperatures. The simplest approach to understanding collision broadening is to assume that interaction between molecule and radiation is momentarily halted upon collision with another molecule, and a minor random phase change is introduced. This causes slight deviations in the frequencies that would be absorbed without the collisions taking place, in effect broadening the absorption peak.

The interactions between molecules depend on their rotational and vibrational state and on the species of other molecules which may be diluting the absorbing molecules. Only at low pressure or high temperature does Doppler broadening become important. Figure 3.3 illustrates pressure
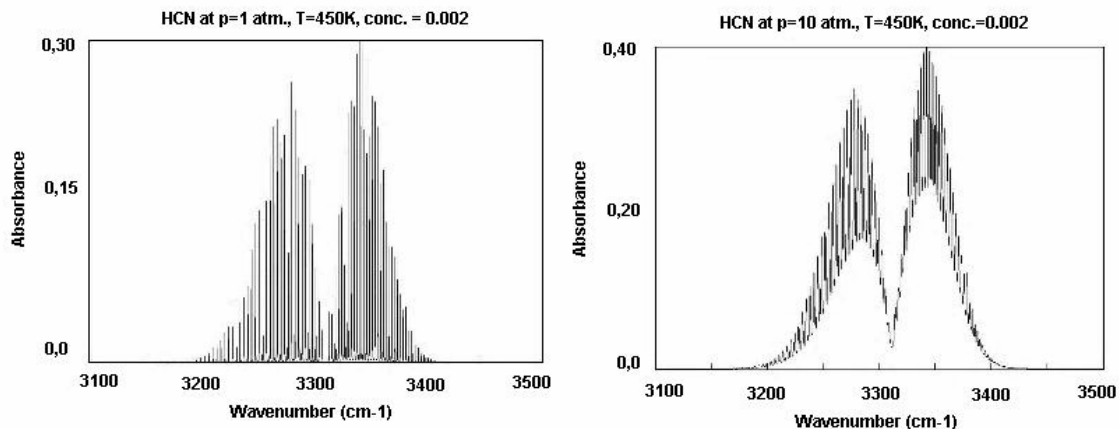
Figure 3.3: Molspec92 simulated plots of HCN absorption at 450K and a pressure of 1 atm. (left) and a pressure of 10 atm. (right).

broadening, again for HCN. The spectra have been calculated with the software programme Molspec92, for a temperature of 450K. In the left graph, the pressure is set at 1 atmosphere, in the right graph it's at 10 atmospheres. The figure shows that the absorption values increase with pressure. This can be explained by an increase in absorption coefficient with increasing pressure. Equation 3.23 shows that k is indeed a function of pressure too. In the extreme case the separate absorption peaks have disappeared altogether and the spectrum shows only one line, connecting all the summits of separate peaks. In appendix C such a spectrum is shown for HCN at 100 atmosphere. Less evident but certainly present, is a slight shift of the peaks to the right as pressure increases, by as much as a few wavenumbers. This may be due to interactions between molecules in different vibrational and rotational states. [15, 16]

§3.2 FTIR spectrometry

Most FTIR machines use the Michelson interferometer, invented in 1891. The interferometer consists of an infrared source, a beam splitter, a moving mirror, a fixed mirror and a J-stop, as shown in figure 3.4. The J-stop ensures a certain degree of parallelism of the IR beam before it enters the interferometer. The beam splitter is made from a material which transmits and reflects the collimated IR beam equally to the moving and the fixed mirror. Both mirrors reflect the incident beam back to the beam splitter, where the separated beams are re-combined. Depending on the wavelength of the radiation and the optical path difference (OPD) introduced by the moving mirror, the beams interfere constructively or destructively. Contrary to reflective infra red spectroscopy, which works at only a small wavenumber range, in FTIR all the source wavelengths are measured simultaneously, which is called the multiplex or Fellgett advantage. The signal that is detected by the detector is now digitised and recorded as a function of the optical path difference, also called retardation δ[cm]. The interferogram intensity $I(\delta)$ of a polychromatic source is a function of OPD and wavenumber and is described by

$$I(\delta) = \int_{-\infty}^{+\infty} B(\upsilon)\cos(2\pi\upsilon\delta)d\upsilon \quad , \tag{3.3}$$

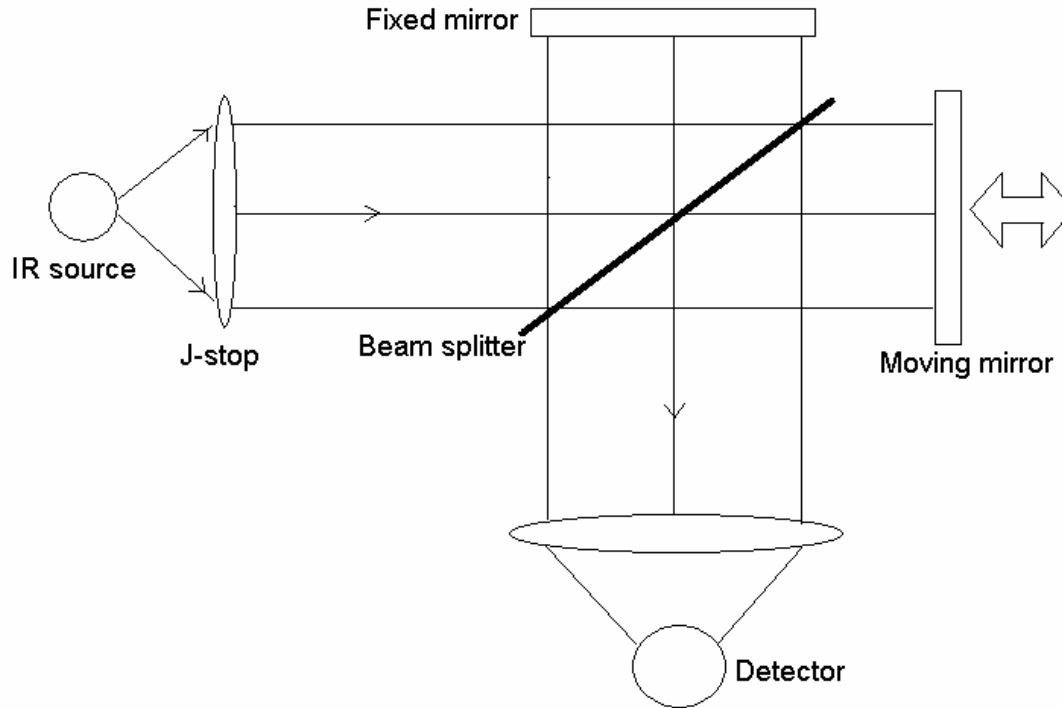where υ is the wavenumber [cm^{-1}] and B the spectral intensity [W/m^{2}cm^{-1}].

15

Figure 3.4: Schematic representation of Michelson interferometer.

When the source that is used for the interferogram is monochromatic, the interferogram intensity $I(\delta)$ is a simple sinusoidal wave, as shown at the top of figure 3.5. When a polychromatic source is used, e.g. the IR source in the FTIR device, the interferogram is a superposition of sinusoidal waves at all wave numbers. For a retardation of zero all sinusoidal waves are totally constructive, producing a centerburst on the interferogram, also seen in figure 3.5 for a continuum source. For other retardation values there will be destructive interference, reducing the intensity of the beam.

Next, Fourier transformation is used on the interferogram to obtain the single beam IR spectrum by making use of the following equation

$$B(\upsilon) = \int_{-\infty}^{+\infty} I(\delta)\cos(2\pi\upsilon\delta)d\delta . \qquad (3.4)$$

As the integration interval of equation 3.4 shows, the optical path difference should run from minus infinity to plus infinity to account for all wavenumbers. Understandably this is not a very practical range, so in practice a discrete Fourier transform (DFT) is used. This reduces equation 3.4 to

$$B(k \cdot \Delta\upsilon) = \sum_{n=0}^{N-1} I(n \cdot \Delta\delta)\cos\left(\frac{2\pi \cdot kn}{N}\right) . \qquad (3.5)$$

In equation 3.5 the continuous variables of wavenumber υ and retardation δ have been replaced by discrete values k and n, respectively. The summation Σ is over the total number of discretised data points N.
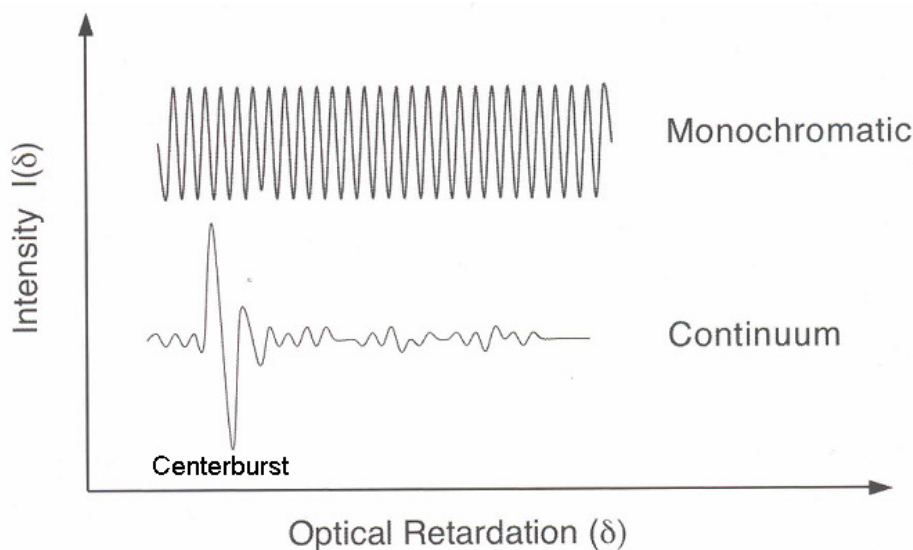
Figure 3.5: Interferogram with centerburst from continuum source and simple sinusoidal wave from a monochromatic source.

The FTIR spectrometer used in experiments is a PerkinElmer Spectrum GX dual source. This spectrometer is categorised as a continuous scan spectrometer and the moving mirror translates at a constant velocity v. The optical path difference at time t of a measurement is than given by $\delta=2vt$. The HeNe laser which is also present inside the FTIR device emits a beam with a known wavelength, about 633 nm. The laser light follows the same path as the IR beam, so every time the modulated light of the laser is measured zero by the detector, the distance the mirror has moved is known (half the wavelength of the laser light). The interferogram data points are digitised at the zero crossings of the laser, which ensures that $I(\delta)$ is measured at precisely equal intervals or mirror positions and it also provides an internal calibration for every scan. This way of wavenumber calibration is very accurate, and is called the Connes advantage. Because of the continuous motion of the mirror, the interferogram $I(\delta)$ becomes an explicit function of time. The Fourier frequency f_F of light at wavenumber v is a function of mirror velocity v and is given by

$$ f_F = 2v\upsilon . \tag{3.6} $$

For time-dependent processes, continuous-scan FTIR may no longer be useful because the temporal Fourier frequencies become convolved with the time-dependence of the process. Also, when using FTIR it is advisable to perform several scans on the same sample, thus increasing the accuracy of the measurement, and than use the averaged values calculated by the machine as the final result. More on taking measurements with the Perkin Elmer Spectrum GX FTIR can be found in Appendix D. Because taking several scans obviously requires more time than taking one scan, continuous FTIR is not very suitable for measurements on gas evolution kinetics, because of the very small time scales involved in kinetics. A step-scan device is faster and could therefore be used, but that kind of machine is not available now and may still be too slow, considering the speed of kinetics. Theoretically, because the FTIR measures in a large range of wave numbers, the contour of all absorption bands of one molecule may be used to determine the component concentration of the gas, as mentioned in the previous paragraph. The intensity of one spectral line may vary with temperature, but the area underneath a band contour should stay the same, as shown in figure 3.6.
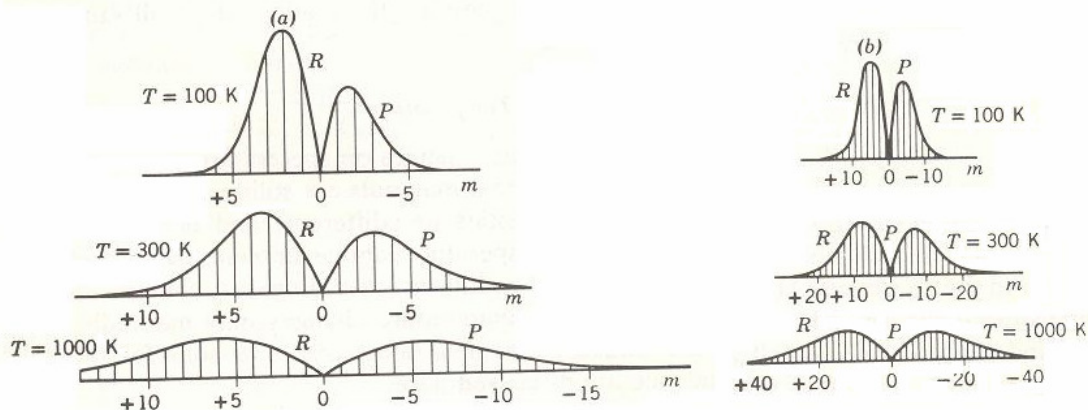
Figure 3.6: Examples of different values for absorption at one absorption band, for increasing temperature and equal amount of absorbing species. The total area, representing the concentration of the molecule, remains equal [12].

Looking at all the absorption bands will ensure that all the states of the molecule under consideration are taken into account, thus giving an accurate value for the concentration. In practice however, this way of determining concentration of a certain species is difficult to use, especially in case of gas mixtures, because of interference of absorption spectra of other species. More about unknown concentration determination can be found in paragraph 3.3. Compared with dispersive spectrometers, an FTIR can reach the same resolution with higher energy throughput because there are no slits. This is called the throughput or Jacquinot advantage. Because of this the same signal-to-noise ratio can be reached by an FTIR in a shorter time. Combined with the Fellgett advantage (all frequencies simultaneously) this is the most important feature of FTIR machines.

§3.3 Quantitative analysis

Theoretically there is a linear relationship between IR absorption and concentration of a certain species, described by Beer's law, often written as

$$A = \varepsilon l c \ , \tag{3.7}$$

where ε is the absorptivity of a molecule at a certain wavelength in $[cm^2/mol]$, l is the pathlength of the IR beam through the sample in $[cm]$ and c is the concentration of the molecule in the gas in $[mol/cm^3]$. The absorptivity ε is a proportionality constant between absorbance and concentration when the pathlength is fixed. The absorptivity changes with wavenumber and molecule under consideration, but under equal conditions it is a physical property of the molecule for a given wavenumber and for a given molecule. In practice, the absorption/concentration relationship is not linear on the entire range of concentrations, especially close to 0 and to 1. This nonlinear behaviour may be explained by molecular interactions. Calibration of the FTIR with gases of which the exact composition is known will prove to what extent the Beer's law is valid and can be used for quantification. Most FTIR software will allow easy change of absorption spectra into transmittance spectra and vice versa. For qualitative comparison it doesn't matter which spectrum is used, but for quantitative analysis it is most convenient to use only absorbance spectra, because absorbance is linear with concentration as stated by Beer's law, see equation 3.7. Appendix E deals with the influence of some spectral modifications and their influence on the final result is discussed [16].

Transmittance is defined as

$$T = \frac{I}{I_0}. \qquad (3.8)$$

In equation 3.8, I is the intensity of a beam that passed through a sample and I_0 is the intensity of the same beam without passing through a sample, also known as background intensity. Absorbance is defined as

$$A = \log(I_0 / I), \qquad (3.9)$$

with *log* the base 10 logarithm. From equations 3.8 and 3.9 it can be seen that

$$A = \log(1/T). \qquad (3.10)$$

Setting equation 3.7 equal to equation 3.10 gives

$$\varepsilon l c = \log(1/T), \qquad (3.11)$$

which results in the following equation when the logarithm is eliminated,

$$T = 10^{-\varepsilon l c}. \qquad (3.12)$$

Equation (3.12) clearly shows that transmittance and concentration do not have a linear relationship, which makes transmittance more difficult to use for quantitative analysis.

§3.4 Calculating absorbance spectra

Obtaining an absorption spectrum can be done by conducting measurements, but when certain parameters are known such an absorption spectrum can also be calculated. A database that contains parameters that may be used in the calculation of absorption spectra is HITRAN (High-resolution TRANsmisson) [14,17]. The goal of HITRAN is to have a theoretically self-consistent set of parameters, while at the same time attempting to maximize the accuracy. The parameters in HITRAN are sometimes direct observations, but most of the parameters are calculated and the result of various quantum-mechanical solutions. There is a lot of information in the HITRAN database and therefore the JavaHAWKS (Java-based HITRAN Atmospheric WorKStation) software programme is used to perform the basic operations on the database, such as filtering by means of frequency, molecule, isotope, band system, etc. JavaHAWKS is also used for plotting the line-by-line or cross-section data, and for various other database management functions [17]. Appendix F gives a quick guide how to work with JavaHAWKS.

By calculating the absorption spectrum of a certain molecule the location of the strongest absorption peaks can be estimated before any experiments have been done, and this speeds up the process of finding the right peaks for quantification. Also, calculations make it easier to identify components that may interfere in a certain wavenumber range and may complicate the quantification process.

The graphs that are computed by the software programme JavaHAWKS are not absorption spectra. Absorbance does not have a unit, whereas the units on the vertical axis of the JavaHAWKS graphs are $[cm^{-1}/(molecule\ cm^{-2})]$, which is called the spectral line intensity. The spectral line intensity data can be used to calculate the absorption spectrum of a certain species. This is done in the following way [18].

Radiative transfer theory [19] for the two states of vibrational-rotational systems can be used to define the spectral line intensity as

$$S_{\eta\eta'} = \frac{h\nu_{\eta\eta'}}{c} \cdot \frac{n_\eta}{N}\left(1 - \frac{g_\eta n_{\eta'}}{g_{\eta'} n_\eta}\right) B_{\eta\eta'} \quad , \tag{3.13}$$

in which h is Planck's constant [ergs s], $\upsilon_{\eta\eta'}$ is the spectral line intensity transition frequency $[cm^{-1}]$, c is the speed of light [cm/s], n_η and $n_{\eta'}$ $[cm^{-3}]$ are the populations of the lower and upper states respectively, N is the molecular number density $[cm^{-3}]$, g_η and $g_{\eta'}$ [-] are the state statistical weights (including electronic, vibrational, rotational and nuclear statistics). Finally, $B_{\eta\eta'}$ $[cm^3/(ergs\ s^2)]$ is the Einstein coefficient for induced absorption.

One of the parameters that is obtained from the JavaHAWKS output file is the weighted transition-moment squared Я$_{\eta\eta'}$ [Debye^2 = 10^{-36} ergs cm^3], which is defined by

$$Я_{\eta\eta'} = \frac{1}{g_\eta}\sum_{\varsigma\varsigma'}\left|R_{(\eta\varsigma)\cdot(\eta'\varsigma')}\right|^2. \tag{3.14}$$

The Einstein coefficient $B_{\eta\eta'}$ is related to the weighted transition-moment squared Я$_{\eta\eta'}$ by

$$Я_{\eta\eta'} = \frac{3h^2}{8\pi^3} B_{\eta\eta'} 10^{36}. \tag{3.15}$$

Assuming local thermodynamic equilibrium, the population partition between states is governed by Boltzmann statistics at ambient temperature T [K]. Thus, two terms in equation 3.13 can be rewritten:

$$\frac{n_\eta}{N} = \frac{g_\eta \exp(-c_2 E_\eta/T)}{Q(T)} \quad \text{and} \quad \frac{g_\eta n_{\eta'}}{g_{\eta'} n_\eta} = \exp\left(\frac{-c_2 \nu_{\eta\eta'}}{T}\right). \tag{3.16}$$

In these equations the second radiation constant $c_2 = hc/k = 1.4388$ [cm K] and E_η $[cm^{-1}]$ is the lower state energy. The total internal partition sum $Q(T)$ [-] is given by

$$Q(T) = \sum_\eta g_\eta \exp(-c_2 E_\eta/T). \tag{3.17}$$

Rewriting and substituting 3.15 and 3.16 into 3.13 at the reference temperature T_{ref} (296 K for JavaHAWKS) and introducing the natural terrestrial isotopic abundance I_a finally gives the equation for the spectral line intensity used in JavaHAWKS, which is

$$S_{\eta\eta'}(T_{ref}) = \frac{8\pi^3}{3hc} v_{\eta\eta'} \frac{I_a g_\eta \exp(-c_2 E_\eta / T_{ref})}{Q(T_{ref})} \left[1 - \exp(-c_2 v_{\eta\eta'} / T_{ref})\right] Я_{\eta\eta'} 10^{-36}. \qquad (3.18)$$

This means that the units of spectral line intensity $S_{\eta\eta'}$ are [cm^{-1}/(molecule cm^{-2})]. This definition of spectral line intensity is used by HITRAN, and subsequently by JavaHAWKS.

When the spectral line intensity is calculated with JavaHAWKS, it needs to be converted to absorbance to be able to compare measurement data with the HITRAN database. First, expressions are given which can be used to correct the spectral line intensity $S_{\eta\eta'}$ for temperatures differing from the HITRAN default temperature of 296 K and for pressures other than the default 1 atmosphere. Than, the relation between $S_{\eta\eta'}$ and absorbance is given.

The equation that corrects the line intensity for temperature is given by

$$S_{\eta\eta'}(T) = S_{\eta\eta'}(T_{ref}) \frac{Q(T_{ref})}{Q(T)} \frac{\exp(-c_2 E_\eta / T)}{\exp(-c_2 E_\eta / T_{ref})} \frac{\left[1 - \exp(-c_2 v_{\eta\eta'} / T)\right]}{\left[1 - \exp(-c_2 v_{\eta\eta'} / T_{ref})\right]}. \qquad (3.19)$$

The third term on the right hand side in the above equation accounts for the Boltzmann populations, the fourth term for the effect of stimulated emission.

Next, the line halfwidth at half maximum can be corrected for temperature and pressure. The pressure broadened line halfwidth $\gamma(p,T)$ for a gas at pressure p [atm], temperature T [K] and partial pressure p_s [atm] is calculated with

$$\gamma_{(P,T)} = \left(\frac{T_{ref}}{T}\right)^n \left(\gamma_{air}(p_{ref}, T_{ref})(p - p_s) + \gamma_{self}(p_{ref}, T_{ref}) p_s\right). \qquad (3.20)$$

In this equation γ_{air} [cm^{-1}/atm] is the air-broadened halfwidth at half maximum at T_{ref} = 296 K and p_{ref} = 1 atm., and γ_{self} [cm^{-1}/atm] is the self broadened halfwidth at half maximum. Both parameters are transition dependent. The coefficient of temperature dependence of the air-broadened half width, n, is (in absence of other data) assumed to be equal to that of the self-broadened halfwidth.

Due to different pressure than atmospheric, the transition frequency $v_{\eta\eta'}$ may shift. This can be calculated by

$$v_{\eta\eta'}^* = v_{\eta\eta'} + \delta(p_{ref}) p. \qquad (3.21)$$

In equation 3.21, δ [cm^{-1}/atm] is the air-broadened pressure shift at T_{ref} and p_{ref} and is transition dependent.

In an absorbing gas, the spectral line is broadened about the transition wave number $v_{\eta\eta'}$ and this spread can be represented by the normalized line shape function $f(v, v_{\eta\eta'}, T, p)$ [1/cm^{-1}]. When pressure broadening dominates, and a Lorentz profile is assumed, the following expression can be used for the normalised line shape function,

$$f(\nu,\nu_{\eta\eta'},T,p) = \frac{1}{\pi} \frac{\gamma(p,T)}{\gamma(p,T)^2 + [\nu - (\nu_{\eta\eta'} + \delta(p_{ref})p)]^2} . \qquad (3.22)$$

The monochromatic absorption coefficient $k_{\eta\eta'}(\nu,T,p)$ [1/(molecule cm^{-2})] at wavenumber ν [cm^{-1}] due to this transition is given by

$$k_{\eta\eta'}(\nu,T,p) = S_{\eta\eta'}(T)f(\nu,\nu_{\eta\eta'},T,p) . \qquad (3.23)$$

The absorbance can now be obtained by multiplying the absorption coefficient $k_{\eta\eta'}(\nu,T,p)$ by the number density of absorbing molecules per unit path length N [molecule cm^{-3}] and the path length b [cm], giving

$$A = Nbk_{\eta\eta'}(\nu,T,p) , \qquad (3.24)$$

which is dimensionless, as it should be.

The number density of absorbing molecules per unit path length N is calculated using

$$N = \frac{p_s \cdot N_A}{R \cdot T} , \qquad (3.25)$$

with p_s [atm] the substance partial pressure, N_A [molecule/mol] Avogadro's number, R [cm^3 atm/mol K] the universal gas constant and T the gas temperature [K].

The above derivation (equations 3.13 through 3.25) is only valid for local thermodynamic equilibrium (LTE). Under non-LTE conditions the partition of population between states no longer follows the Boltzmann statistics and equations 3.16 are no longer valid. The line intensities under these conditions may be obtained directly from the weighted transition-moment squared Я$_{\eta\eta'}$ [18] or by correcting the HITRAN calculated intensity $S_{\eta\eta'}(T_{ref})$ [20]. The latter method is described in Appendix G.

§3.5 Validation of calculated spectrum of ammonia

To illustrate the method that has been treated in the previous paragraph for calculating an absorption spectrum with JavaHAWKS data and to verify that the result is indeed an absorption spectrum, the spectrum of ammonia is computed and compared with a measured spectrum.

There are many columns in a typical JavaHAWKS output file, which are not all needed to perform the necessary calculations. Because the Matlab software package has a problem with some of the rows in the unaltered JavaHAWKS output file (the number of columns is not always equal for every row), the data that is not needed is discarded. What remains is a matrix of eight columns, listing the spectral line intensity transition frequency $\nu_{\eta\eta'}$, the spectral line intensity $S_{\eta\eta'}$, the weighted transition-moment squared Я$_{\eta\eta'}$, the air-broadened halfwidth at half maximum γ_{air} , the self broadened halfwidth at half maximum γ_{self} , the lower state energy E_η and the coefficient of temperature dependence of the air-broadened half width n_{air}, respectively. A typical HAWKS
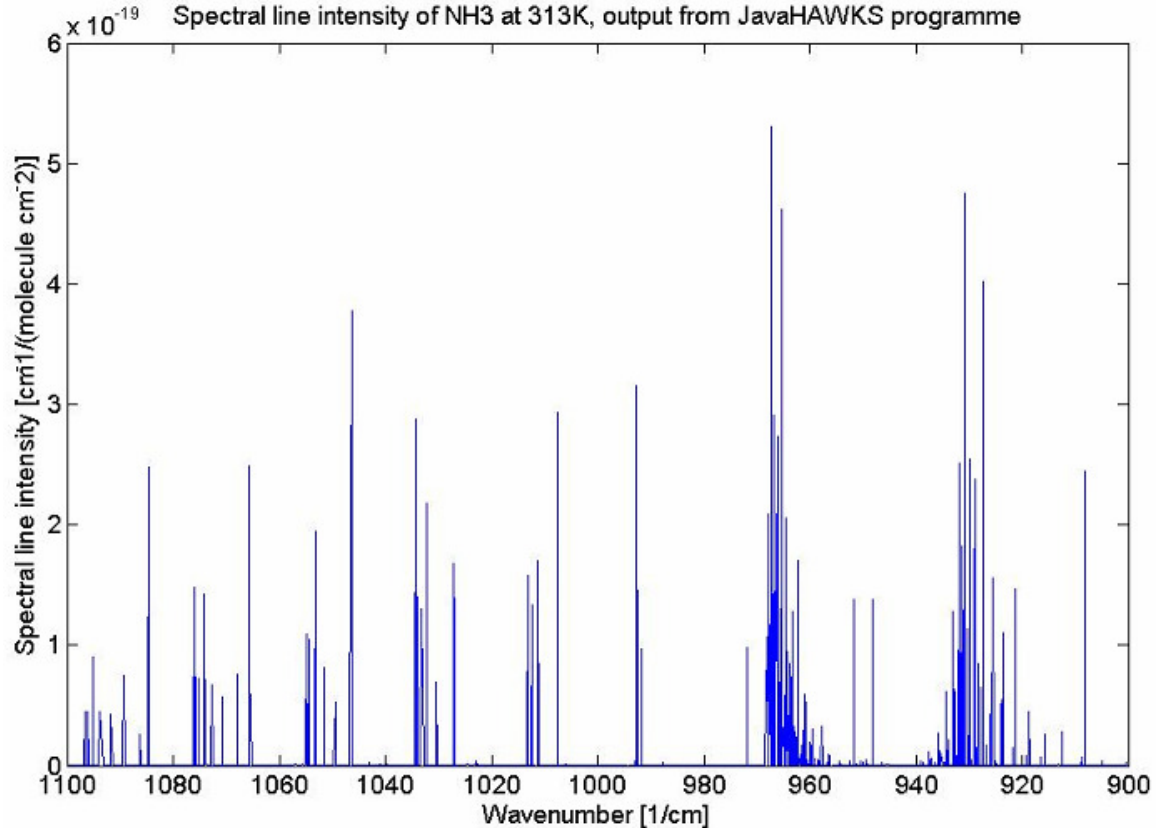
Figure 3.7: Spectral line intensity as function of wavenumber, from JavaHAWKS programme.

graph for ammonia is visualised in figure 3.7, which shows the spectral line intensity as a function of wavenumber. Note the higher density of spectral intensity lines around 930 and 965 cm^{-1}, which will result in broadening of the absorption lines.

The transition wavenumber $v_{\eta\eta'}$ has an influence on all wavenumbers in the range under consideration, described by a Lorentzian profile. Figure 3.8 shows the Lorentzian line profile for the transition near wavenumber 1004 cm^{-1}. Note how the base of the peak becomes broader as it gets closer to the horizontal axis. Multiplying this profile by the spectral line intensity $S_{\eta\eta'}$ [cm^{-1}/(molecule cm^{-2})] gives the spectral intensity of that particular transition.

By calculating the effect of each transition on the entire range of wavenumbers under consideration, and then summing all these effects one obtains the absorption coefficients for each wavenumber in that range, as shown in figure 3.9 for ammonia between 900 and 1100 cm^{-1}. Note the small values on the vertical axis. Among other parameters, Avogadro's number is used in the calculation of absorption from the values in figure 3.9, as can be seen in equations 3.24 and 3.25.
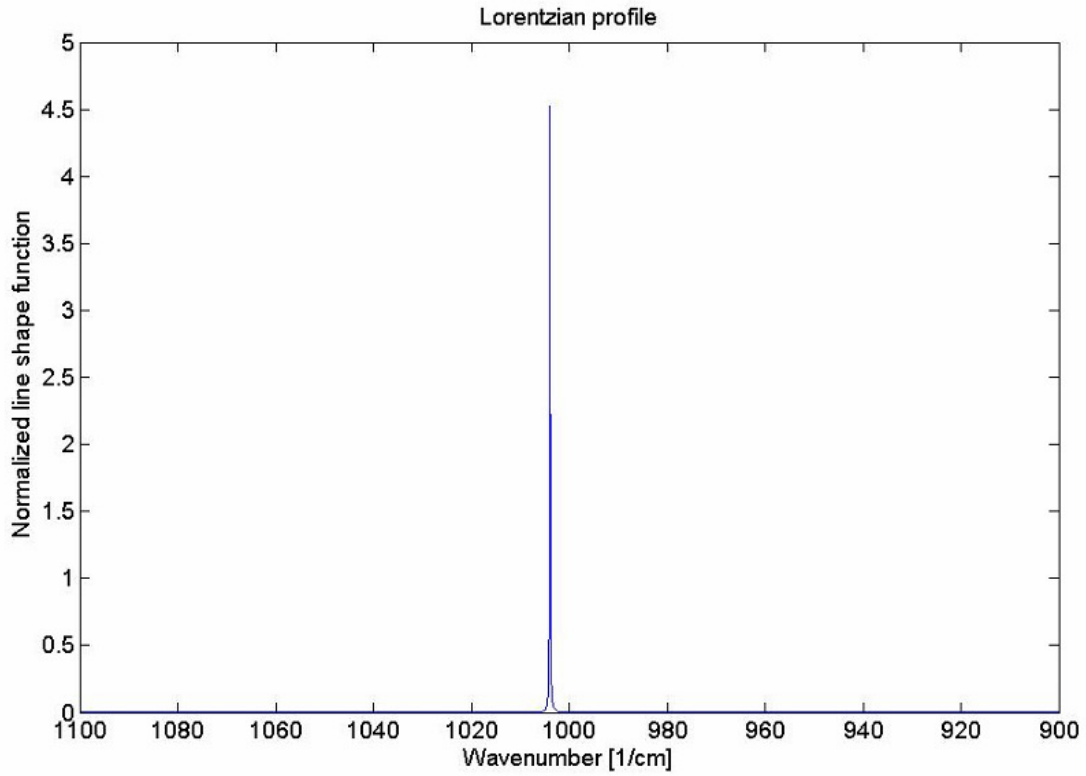
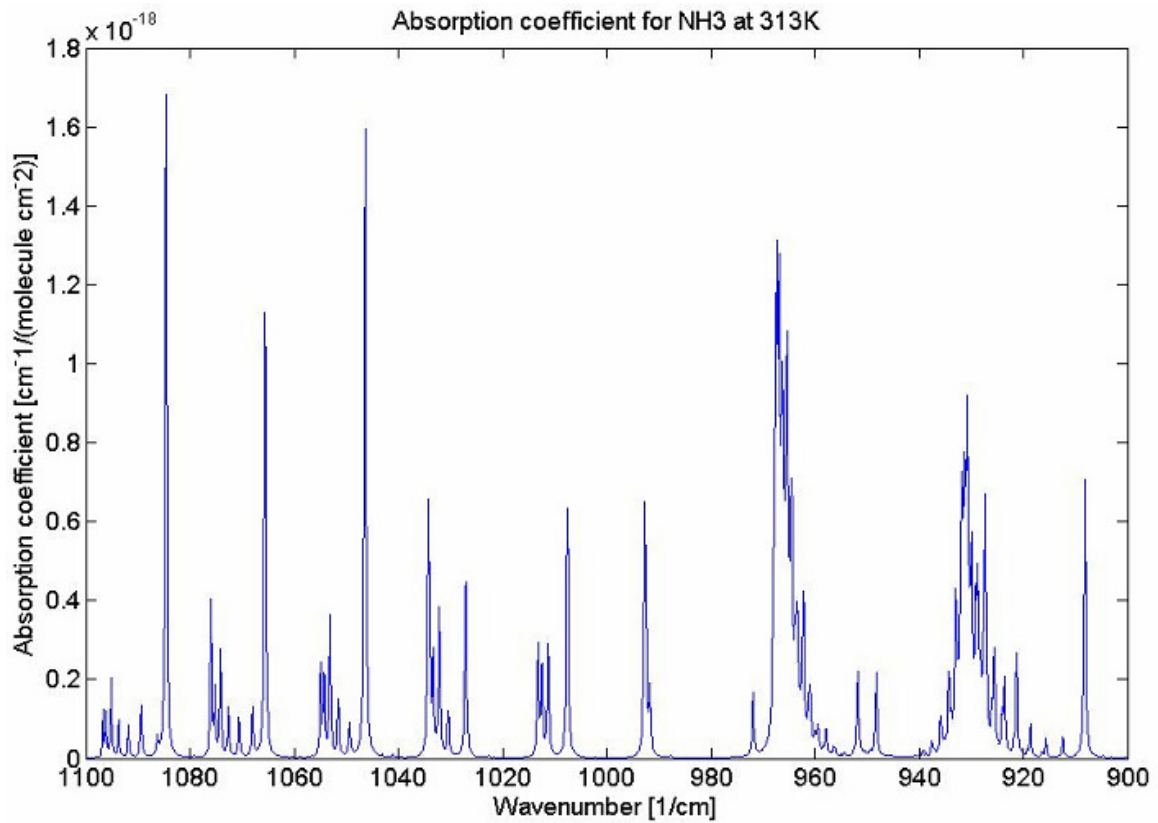Figure 3.8: Example of Lorentzian line shape near 1004 cm^{-1}.

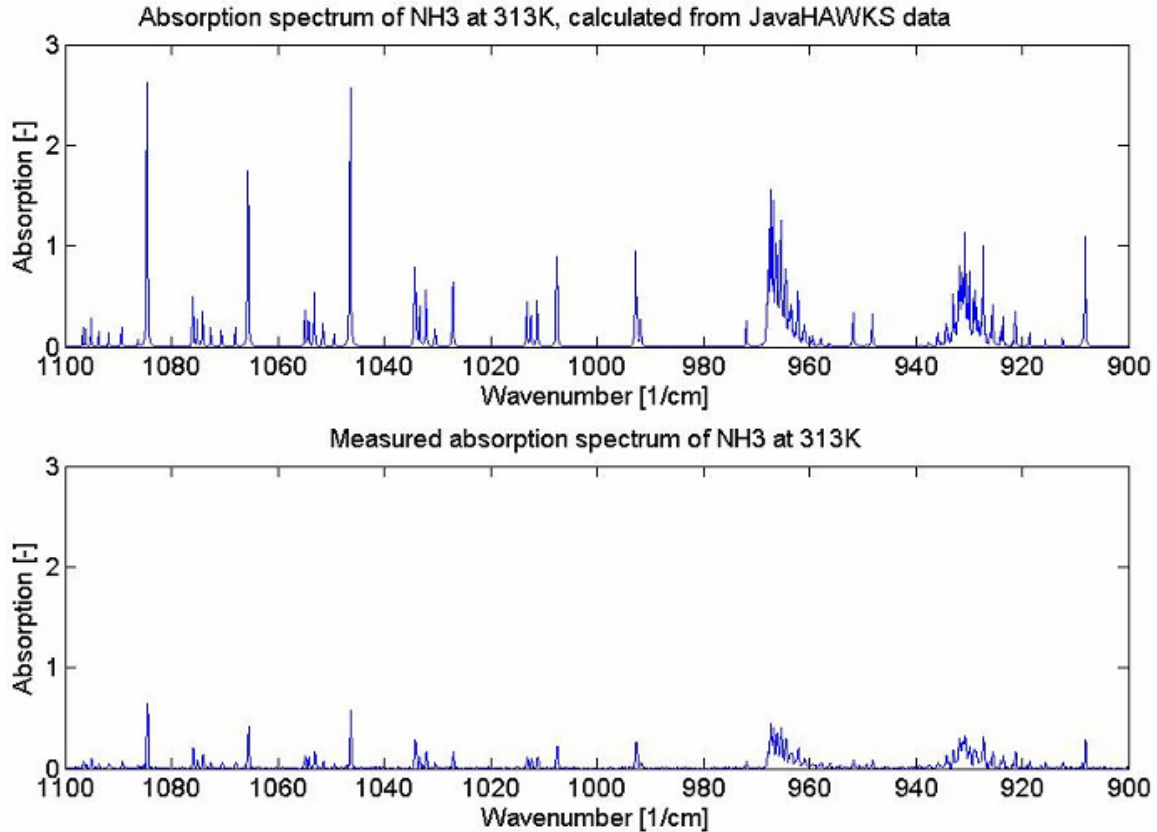Figure 3.9: Absorption coefficients for ammonia at 313K between 900 and 1100 cm^{-1}.

Figure 3.10: Ammonia absorption spectrum, calculated from JavaHAWKS data (top) and measured (bottom).

Next, the absorption is calculated by multiplying the absorption coefficients from figure 3.9 with the number density of corresponding absorbing substance and the path length through that substance. The resulting absorbance graph is shown in figure 3.10 and compared to an absorption spectrum of ammonia that is measured in Eindhoven, using a calibration gas consisting of ammonia and nitrogen. The shape of the graphs looks alike so the qualitative comparison is good. However, it is clear that quantitatively the spectra do not match and the values of the calculated spectrum are about a factor four higher than the measured spectrum.

On closer examination the peaks of the calculated spectrum are much thinner than the ones in the measured spectrum. This is not a surprise, since the spectrum is made up of peaks that are the result of calculations, and can therefore be very well defined. In the measured spectrum the lowest value of the resolution of the FTIR spectrometer bounds the width of the peaks to a certain minimum value. Because the area underneath a peak is a measure for the amount of absorbing molecule, a broader peak will be lower for the same amount of absorbing molecule. Fortunately the calculated spectrum can be corrected for this problem by using equation 3.20. To do this the width of a peak at half height of a single absorption peak is compared. Only single peaks away from other peaks should be compared, because absorption peaks that are very close together will also create peak broadening which is not due to limitations in the instrument used but simply a coalescence of two or more Lorentzian profiles. Upon comparison of the peak width at half height it turns out that the calculated peaks are about a factor two too thin. Therefore the pressure broadened line halfwidth $\gamma(p,T)$ is multiplied by two. Now the peak width is comparable, and the calculated peaks are consequently a factor two lower than shown in figure 3.10.
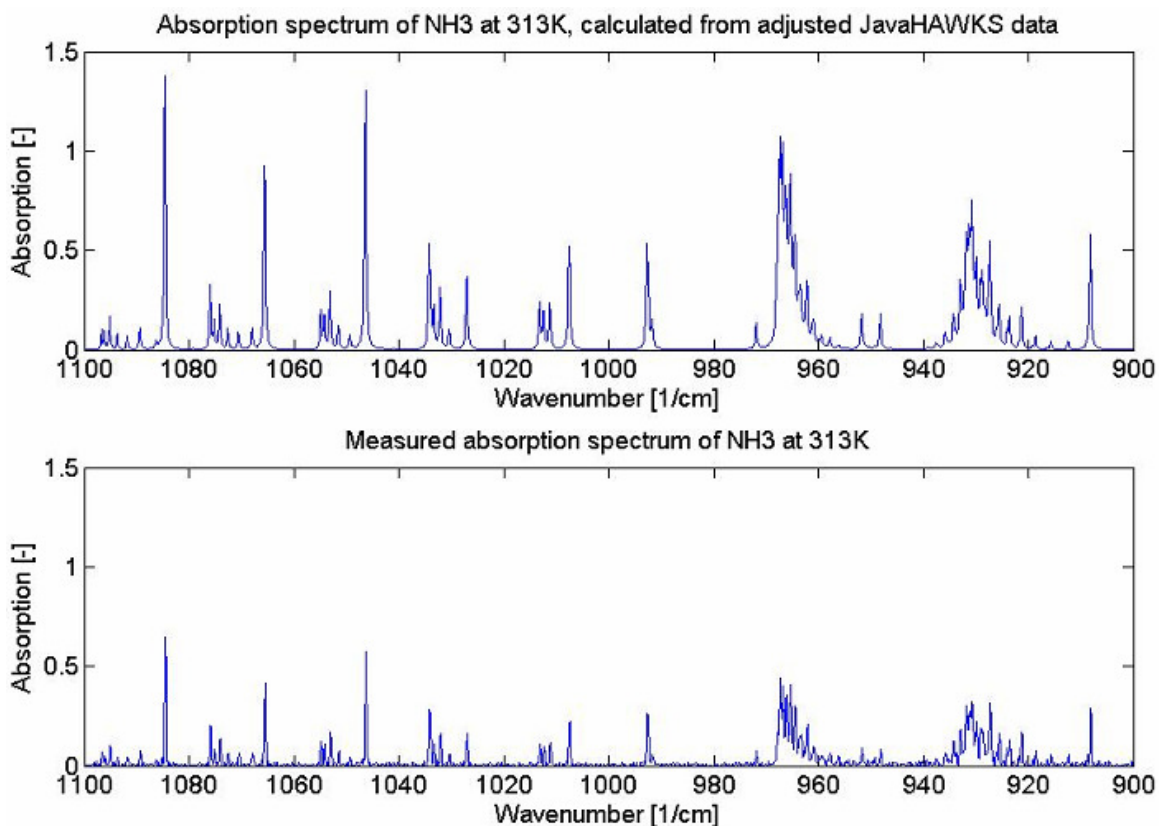
25

Figure 3.11: Ammonia absorption spectrum calculated from adjusted JavaHAWKS data (top) and measurements (bottom).

The two graphs in figure 3.11 still look a lot alike, but now their values also show a better match. The values still differ a factor of about two. This difference can be explained by the fact that the temperature of the calibration gas was not measured specifically but is assumed to be equal to that indicated by the thermocouple inside the grid reactor, approximately 313K. At different temperatures the height of an absorption peak will differ, so any deviation from this temperature will result in a slightly different spectrum since the distribution over different states of the molecules will also shift.

The calibration gas used for this validation is specified to have an ammonia concentration of 2053 ppm, ±2%. This value is therefore used in the calculated spectrum. However, the exact value may be slightly lower since the stability of the gas mixture had expired. New measurements with a gas mixture with a stability that has not yet expired are recommended. These measurements could not be carried out by the author because the delivery time for new gas mixtures did not allow it. Finally, the FTIR is not an ideal machine, so there will always be differences in the comparison of the results of a measurement and calculation, as shown in figure 3.11.

Chapter 4   Experimental methods and validation

§4.1 Set-up

When this project started there was a set-up present at the TU/e which uses a heated grid reactor and a tunable diode laser for measuring relative concentrations of, for instance, CO from pyrolysis of wood powder [21]. This set-up has been modified by D. Deen [22] to enable measurement of ammonia release rate. For measurement of absolute ammonia concentrations a similar set-up using a heated grid reactor is built, but this set up uses an FTIR spectrometer for measuring the gas composition. With a heated grid reactor the pyrolysis parameters of interest can easily be investigated, and therefore such a reactor is used in this project. Figure 4.1 shows a cross section of the reactor used in the experiments. The walls of the reactor are made from stainless steel, with windows at the left and right ends to allow the infrared beam of the FTIR to pass through the reactor, and three smaller windows in the middle to be able to see the grid. The beam splitter inside the FTIR optical compartment was made of calcium-fluoride (CaF_2), but has been replaced by a beam splitter of potassium-bromide (KBr) to be able to investigate the wave number range where ammonia absorbs most strongly. Of course, all optical components will have to allow the IR beam to pass without absorbing too much of the beam. Besides the beam splitter the beam also passes through a window in the side of the optical compartment and through the FTIR windows of the grid reactor. According to the manual of the FTIR machine the window in the side of the FTIR optical compartment is optimised for the working range of the machine. Measuring a background scan proves this to be correct, only below 400 cm^{-1} is absorption by optical components so great that accurate measurements are no longer possible. The FTIR windows in the grid reactor will also have to be made of a suitable material. Potassium-bromide can not be used because it is a hygroscopic material and would decay by exposure to air. A material with the required optical characteristics that is not hygroscopic is zinc-selenide. The FTIR windows in the grid reactor are therefore made of zinc-selenide (ZnSe), which allows measurements down to 370cm^{-1}, so the region where ammonia absorbs most strongly (roughly 900 to 1100 cm^{-1}) can also be investigated.
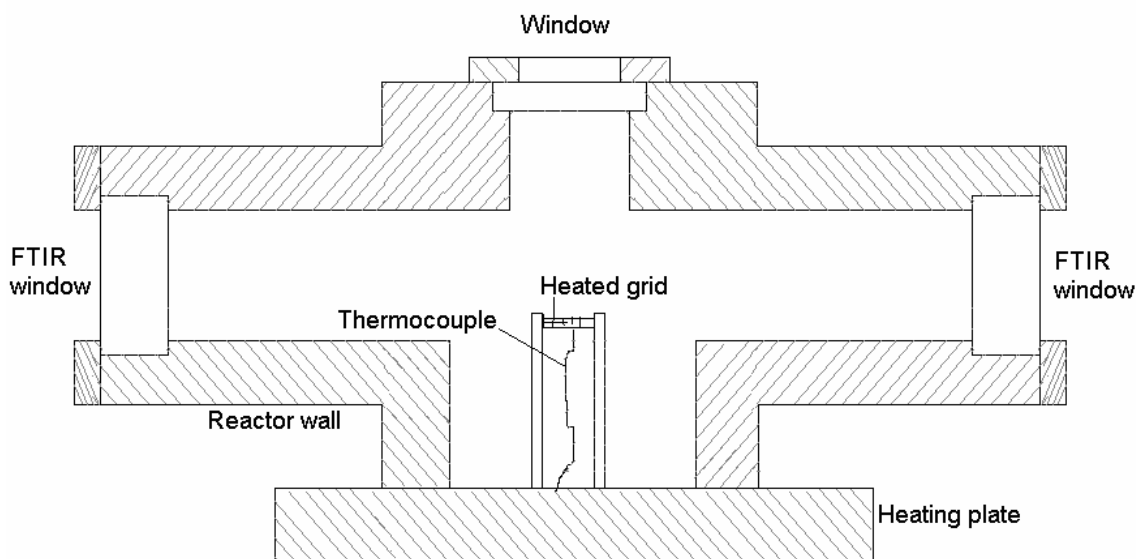

Figure 4.1: Schematic cross section of the heated grid reactor used for experiments.

The small grid inside the reactor is made from metal, usually stainless steel is used but an alternative is to use a platinum grid. By passing a current through the grid, the grid can be heated up quickly, hence the name heated grid. When a small amount of biomass is put onto the grid, it is assumed that this will also heat up quickly. When the atmosphere inside the reactor is made inert by purging with an inert gas, heating of a small amount of biomass will result in pyrolysis ofthe biomass. The pyrolysis product gas will escape from the solid particles and spread through the reactor, after which a measurement on the gas composition can be done by the FTIR. The optical path inside the reactor is now 163.0 mm, from the inside of one FTIR window to the inside of the next. The volume of the reactor has been determined to be about 100.8 cm^3.

The grid temperature is an important variable to know, because the pyrolysis product gas composition will depend mainly on the biomass used for pyrolysis, the heating rate of the particles and the pyrolysis end temperature. For temperature measurement, a thermocouple is welded to the grid by the TFE-workshop. In Appendix H some practical aspects can be found on welding thermocouples to the grid. Now, the biomass particles can be pyrolysed under different measurable conditions to see what the effect is of varying conditions on the release of ammonia from a sample.

The entire grid reactor is mounted on top of a heating plate. With this heating plate the reactor walls are heated to about 105^0C, which will prevent condensation of water vapour and some tars that are formed during the pyrolysis process. Because of the Kalrez® and Viton® O-rings mounted inside the reactor to prevent leakage in case of over- or under-pressure, exceeding the before mentioned 105^0C is not advisable, since the thermocouple that is used in the control loop for the reactor temperature is mounted in the middle of the reactor. As a consequence the temperature at the top and ends of the reactor will be slightly below that indicated by the thermocouple, whereas the temperature at the base of the reactor will be higher. The melting temperature of Kalrez is about 250^OC, that of Viton about 200^OC. When the reactor is heated up too quickly these temperatures may be exceeded in the bottom part of the reactor, causing the O-rings to fail. The power source does not give a continuous current to the cooking plate, but is pulsed by being switched on and off every second. This means that the reactor takes a little bit longer to heat up, but now the heat has more time to conduct through the material, and doesn't get very hot near the cooking plate while still being cold further away from it. The temperature of the reactor is measured with a K-type thermocouple of diameter 2 mm at a position about halfway its height. This position is chosen because it is thought to give a good indication of the mean reactor wall temperature. Proper heating up of the reactor walls takes about two hours.

In picture 4.2 the set-up as it has been built in the Biomass Laboratory of the TU/e is depicted with the different components indicated.

Gas composition measurements are done using a Perkin Elmer Spectrum GX dual source FTIR spectrometer. This machine was purchased by the university in 1999 and has been used in many projects for the interferometer and detector, using an external IR source. For this project the machine has been serviced by a Perkin Elmer engineer who updated the software and replaced the internal IR source. Also, the original CaF_2 beamer splitter has been replaced by a KBr beam splitter, extending the wavenumber range down to 370 cm^{-1}.

For powering the grid a software controlled power source has been designed in collaboration with and built by the GTD, the general technical service of the TU/e. Inside the box that is the power source there are three main components: a Delta power source, a mini PC and a Keithley data
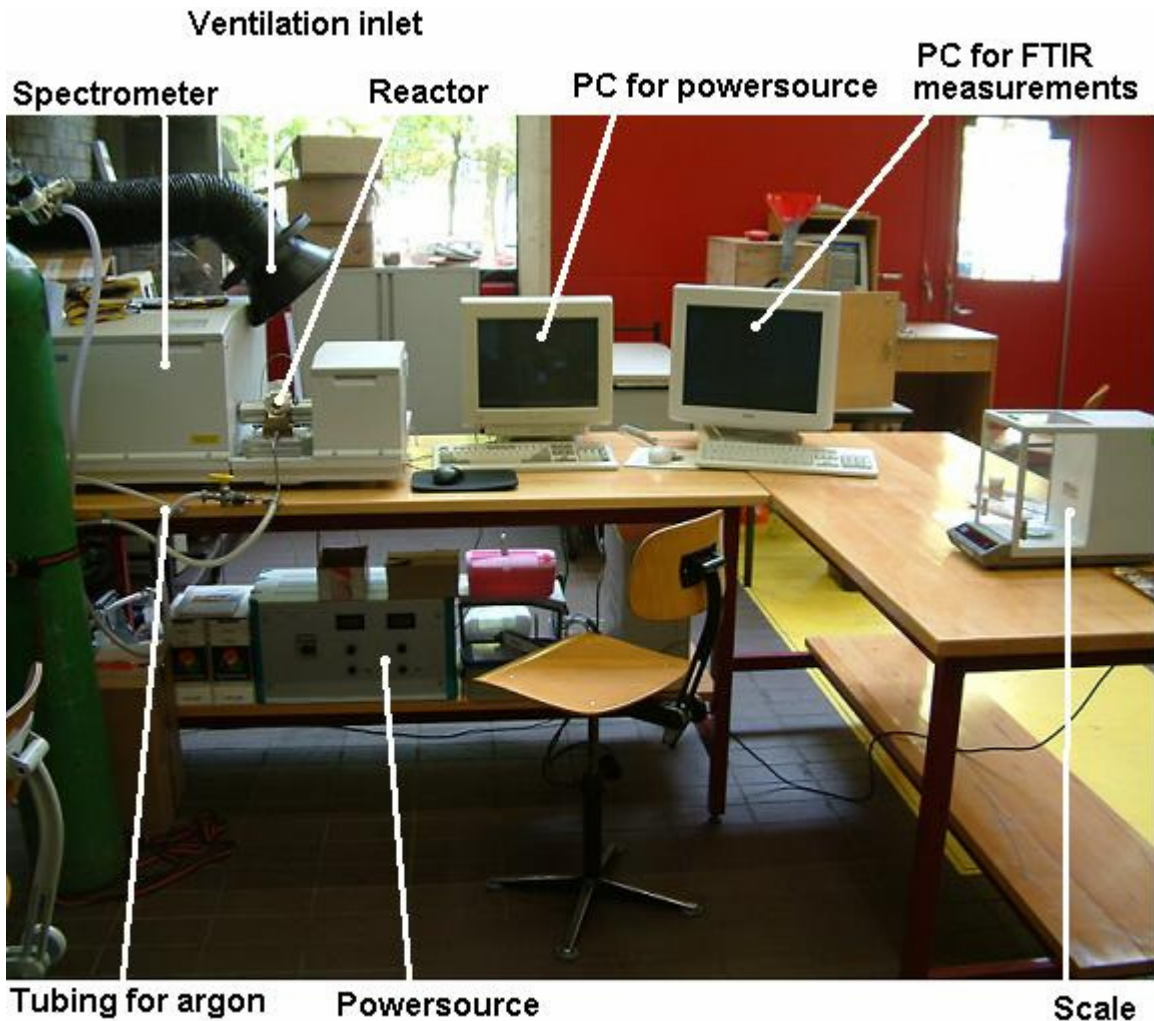
Figure 4.2: Picture of the set-up that has been built in the Biomass laboratory of the TU/e for this project.

acquisition module. The Delta power source is a type S 6-40, with a voltage range of 0 to 6 Volts and a current range of 0 to 40 Amperes [23].

For reading the thermocouple that is fixed to the grid a Keithley module is used. The KUSB_3108 has cold junction compensation (CJC) and a reading rate of 50 kS/s (kilo sample per second) or 50 kHz. More specifications on the Keithley module can be found in Appendix I.
Finally a mini-PC is built into the box of the power source. The task of the mini-PC is to control the Delta power source. Because the control loop needs to be very quick to ensure that the grid reaches the desired temperature quickly enough without (too much) overshoot, the choice has been made to use this mini-PC for the control job only, ensuring a quick response.

The University of Technology of Delft has a set-up for conducting pyrolysis experiments, which looks a lot like the set-up that has been built in Eindhoven. Before the set-up in Eindhoven was built, some experiments have been conducted in Delft to gain experience and to see if anything had been forgotten for the set-up in Eindhoven. The experience gained in Delft greatly reduced the time required to build the set-up for this project and have it up and running.

§4.2 Experimental method

One problem encountered during measurements was that the ammonia concentration decreases in time. The reason for this decrease could not be found, it is certainly not a leak in the gas cell or reactor, nor is it solving of ammonia in water, but the same problem is observed at the University of Delft. To be able to work reproducibly a method for conducting experiments is used, similar to the method used at the TU Delft. This method is described below.

First, the reactor needs to be at an elevated temperature to prevent water vapour condensation and reduce tar condensation. The reactor walls are heated by a cooking plate built into the bottom of the reactor wall. The Labview software that controls the grid can also be used for controlling the

Table 4.1: PID control and set point values used for heating of the grid reactor

Setpoint 2	Set at desired temperature (here, $105^{O}C$)
Output high	2,0
Output low	0,0
Set point 2 (Temperature)	105
PID settings	
Proportional gain K_c	0.50
Integral time T_i [min]	2.00
Derivative time T_d [min]	0.00

reactor wall heating. The reactor is heated by the cooking plate to a temperature of $105^{O}C$ with a control loop that uses PID-control. The reactor wall temperature is not a uniform temperature because the cooking plate is in the bottom and the reactor is not insulated, but exposed to its surroundings. The settings of the Labview software are shown in table 4.1.

The next step is to weigh a small amount of sample to be pyrolysed. The weight needs to be known because the amount of volatiles released from the sample will also depend on the amount of sample. When the reactor is warmed up, the sample can be placed onto the grid and the reactor can be closed again. To be able to conduct pyrolysis experiments the atmosphere inside the reactor needs to be inert. Therefore the reactor is purged with argon for 5 minutes. With the biomass already inside the reactor care needs to be taken with purging the reactor. The purging pressure should not exceed 0.5 bar because at higher pressures the sample may be blown off of the grid.

After the reactor is purged a background scan is taken with the FTIR, the heating rate and grid temperature can be set and when scanning of the background has finished, the set-up is ready for the actual pyrolysis experiment. The software PID control and set point values for the stain less steel grid are shown in table 4.2. The gas inside the reactor is preferably as homogeneous as possible, but only convection due to the warm product gases can be used for obtaining such a homogeneous gas. This may therefore take a prohibitively long time, keeping in mind that the ammonia inside the reactor decreases in time. The time between switching on the grid and the start of the FTIR sample measurement is therefore exactly one minute, ensuring a more or less homogeneous gas composition but also the least decrease in ammonia concentration. After the FTIR sample measurement the gas inside the reactor can be released into a ventilation shaft, and a new amount of sample can be weighed and placed onto the grid for a new experiment.
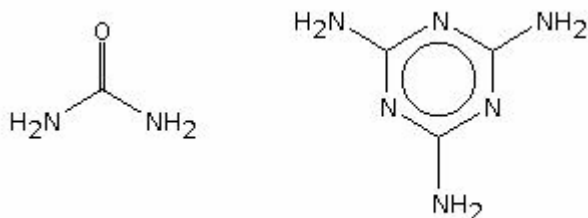
Figure 4.3: The chemical structure of urea (left) and melamine (right).

Table 4.2: Software settings for the grid control

Setpoint 1	Set at desired temperature
Current limit	25 [A]
Output high	6 [V]
Output low	0 [V]
PID	
Proportional gain K_c	0.10
Integral gain T_i [min]	0.001
Derivative gain T_d [min]	0.00

The samples that have been used are MDF, urea and melamine. MDF sawdust is an industrial waste stream that could be used for generating electricity in a more sustainable way. In experiments MDF is used in powder form to increase heat transport during the heating up period compared to larger pieces of MDF, so that the assumption can be made that the grid temperature and the temperature of the particles on the grid is practically the same. Because of a resin that is used in MDF the amount of nitrogen is relatively large, which makes MDF a suitable fuel for use in this project. See table 5.1 for an ultimate analysis of MDF.

Urea and melamine are used as model compounds. As already explained, biomass is a very complex substance. This makes it unsuitable to use right away in any model that links the amount of nitrogen in a fuel to certain combustion conditions and corresponding emissions of nitrogen containing species. The chemical name for urea is CH_4N_2O, that of melamine is $C_3H_6N_6$. The chemical structures of both substances are depicted in figure 4.3. Because the composition of these substances is known exactly and is not very complex, these substances are thought to be suitable to use for the grate furnace model when it is being developed. When the furnace model works correctly for these substances it can be extended for use on more difficult compounds, such as biomass.

§4.3 Calibration

As can be seen from equation 3.7, the amount of infrared absorption by a certain component will be proportional to the amount of component in a gas mixture. To be able to determine the concentration of a component in a gas mixture, for example pyrolysis product gas, a calibration curve will need to be made first. For this calibration curve the path length, the pressure and the temperature of the calibration gases has to be equal to the conditions under which the unknown concentration will be determined. Therefore, the reactor is purged with a calibration gas of known composition for 5 minutes, and the reactor walls are heated to the temperature they will have during experiments, approximately 105^0C. Similar to the pyrolysis experiments the infrared spectrum is taken by the FTIR machine exactly one minute after purging of the reactor with a

calibration gas has stopped. With the spectrum of the calibration gas and a background spectrum, the spectrum of just the component of interest, in this case ammonia, can be made by subtracting the background from the calibration gas spectrum. The result is a spectrum which shows only the absorption lines of the ammonia in the calibration gas, and those of atmospheric water vapour and carbon dioxide because the IR beam can not be shielded from the air.

When this procedure is done several times for one calibration gas and for several calibration gases, a graph like the example in figure 4.4 can be made, relating the absorption to the concentration of a certain species. Preferably the concentrations used for the curve are not multiples of each other. As a rule of thumb, for each component N that needs to be detected, the concentration/absoption curve should be made with at least $2*N+2$ different calibration gases. In figure 4.4 on the horizontal axis the species concentration is set out, on the vertical axis is the absorbance. The crosses represent data points, the line is a least squares fit which can now be used to determine the concentration in an unknown gas. In case Beer's law, equation 3.7, is applicable, the slope of the graph is equal to εl and simply dividing the absorbance by εl will give the unknown concentration.
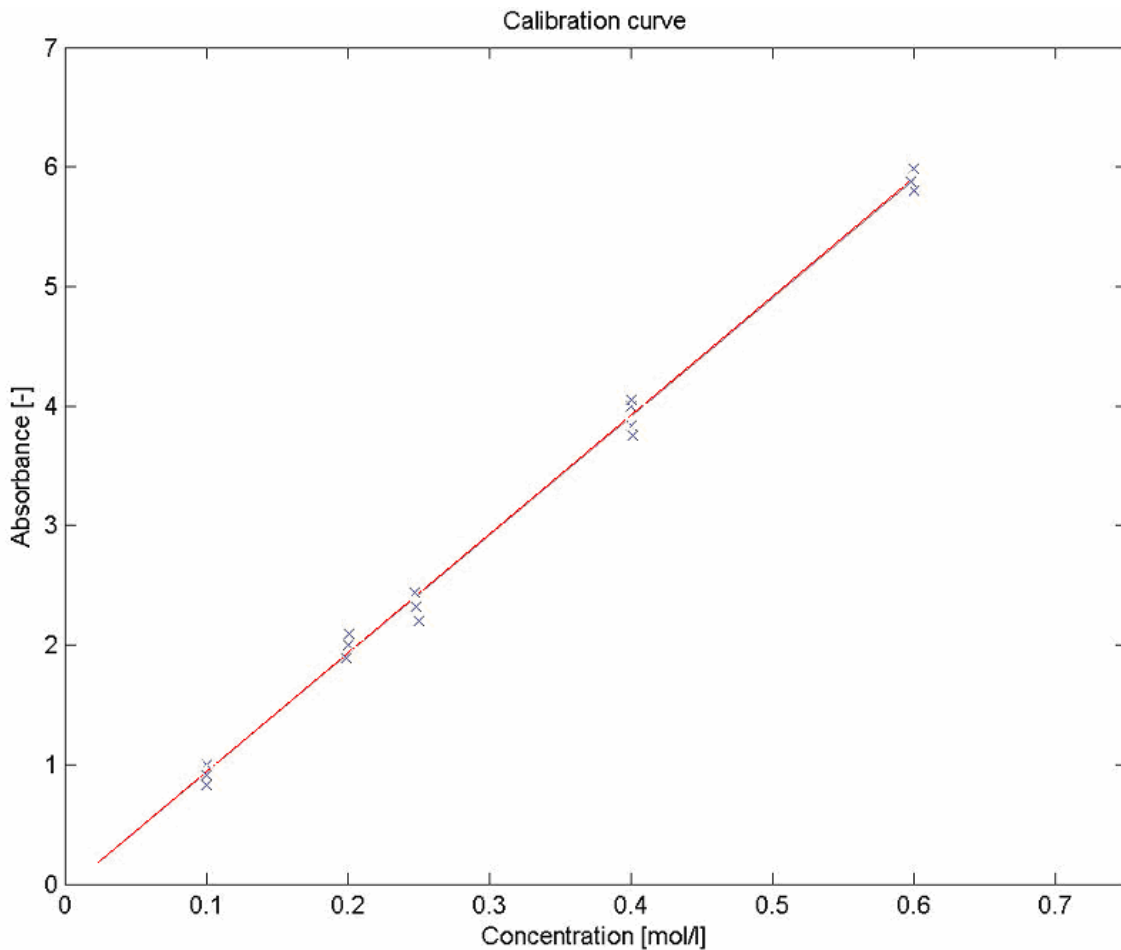

Figure 4.4: Example of a (fictitious) calibration curve relating concentration and absorbance.

Table 4.3: Data on the ammonia calibration gases used for quantification. Indications in % and ppm are to be interpreted as ideal parts per volume. All indications of volume are related to STP(1013 mbar, 273.15 K)

Composition	Accuracy in NH_3 content
202 ppm NH_3, rest N_2	±5% (±10 ppm)
1037 ppm NH_3, rest N_2	±2% (±21 ppm)
2053 ppm NH_3, rest N_2	±2% (± 41 ppm)

An unknown concentration can only be determined as accurately as allowed by the accuracy of the standards that were used for the calibration measurements. Table 4.3 shows data on the calibration gases that have been used.

The quantification of unknown concentrations is automated using Spectrum Quant +, a software package that comes with the FTIR used for this project, and it essentially does the same thing as described in this section but than for all peaks in a specified range, in the case of ammonia for the range 750 to 1300 cm^{-1}. With the Quant + software this is determined to be the optimal range, because the peaks in this range are the highest and they change with concentration.

Chapter 5　　Results and discussion

In this chapter the results of experiments conducted for this project are presented. First the results of pyrolysis of the model compounds urea and melamine are treated, than the results for MDF. In the second paragraph the results are discussed and conclusions are drawn, and the third paragraph deals with the simple first order model for ammonia release rate.

§ 5.1　Results

Urea

Figure 5.1 shows measured ammonia yield from pyrolysis of urea under varying conditions. Each *X* in the figure represents a measurement and the lines are least squares fits through the measurements. Urea contains about 46wt% nitrogen, but it does not have enough hydrogen to form only ammonia, see figure 4.3. In stead when urea decomposes it forms ammonia (NH_3) and iso-cyanic acid (HNCO). If all urea decomposes to form NH_3 and HNCO than a simple calculation using the molar masses of these substances shows that urea should yield 28.4wt% ammonia. This is indicated in figure 5.1 by the dotted line at the top of the figure.
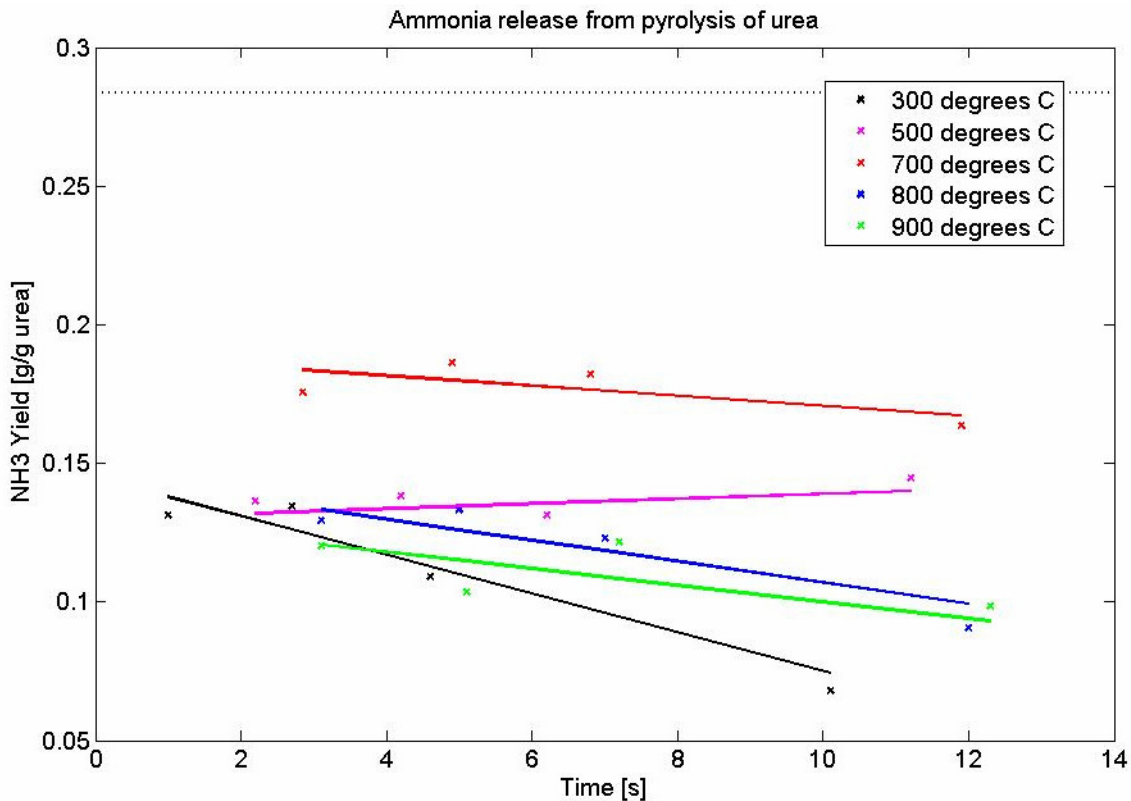

Figure 5.1: Measurement data and least squares fits for pyrolysis of urea.

Melamine

Some experiments with melamine, another model compound, have also been carried out. However, after an experiment the heated grid electrodes and the thermocouple wire that is fixed underneath the grid were stained white, and some melted white substance is left on the grid. The melting temperature of melamine is around 280^OC [28], and around 380^0C all melamine is evaporated. With increasing temperature decomposition of melamine also increases and more white condensate (possibly $C_3H_3N_5$) and ammonia are formed. As a result of the deamination the ammonia yield could also increase with temperature to a certain maximum, after which decomposition of ammonia could take place.

The white substance that is left on the grid after an experiment is thought to be solidified melamine melt, which means that not all melamine evaporated or decomposed. In order for an experiment to be successful all melamine needs to disappear from the grid, either by evaporating or by decomposing. Possibly all melamine will disappear at higher temperatures, but it is not considered as a suitable model in the remainder of this project.

Medium Density Fibreboard, MDF

The results of several experiments for pyrolysis of MDF are presented here in the form of graphs. On the following pages each page shows the temperature of the grid as a function of time at the top, and underneath that is a graph showing the ammonia yield in [mg/g MDF] as a function of time. For practical purposes the temperature and ammonia concentration graphs of one experiment have been place on one page.

The temperature graphs show that the heating up period is equal for all experiments in one graph. After the heating up period, the set temperature is maintained for a certain time, the hold time. After the current through the grid is switched off again the ammonia yield is determined. In the ammonia yield graphs one determined yield corresponds to one temperature-time graph in the figure above it.
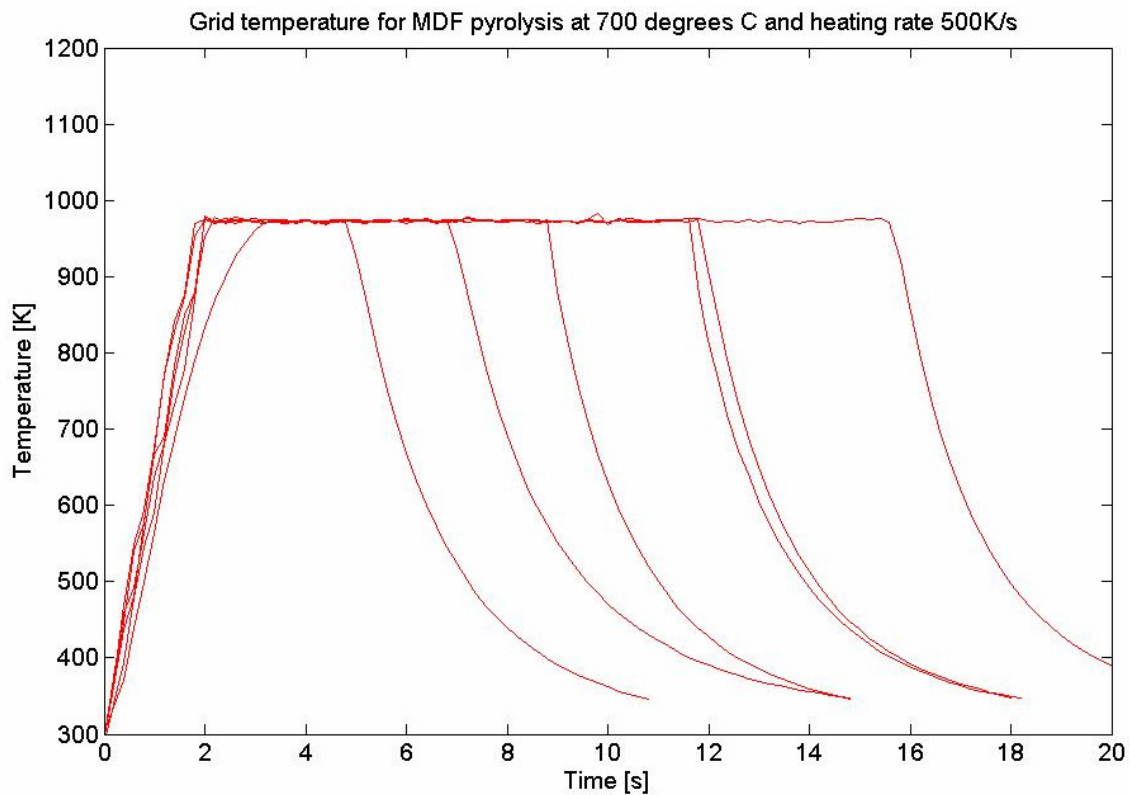
Figure 5.2: Temperature history of pyrolysis experiments of MDF at 700°C and heating up at 500K/s.
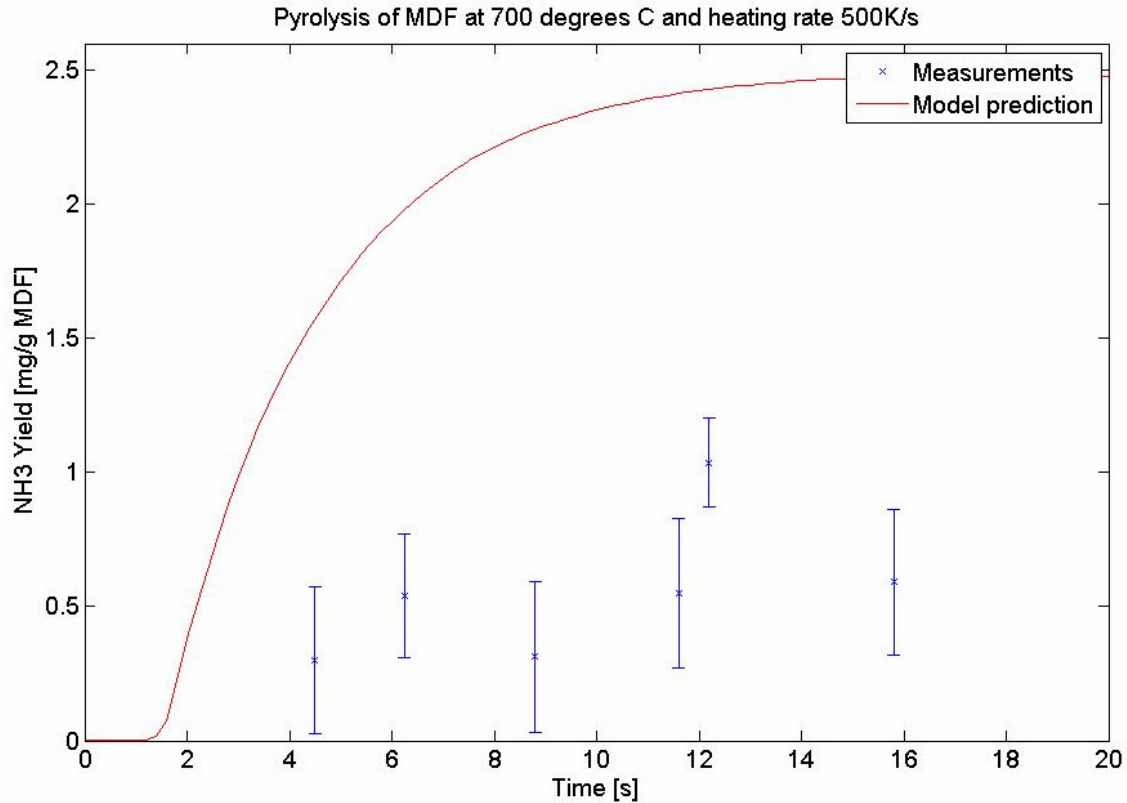

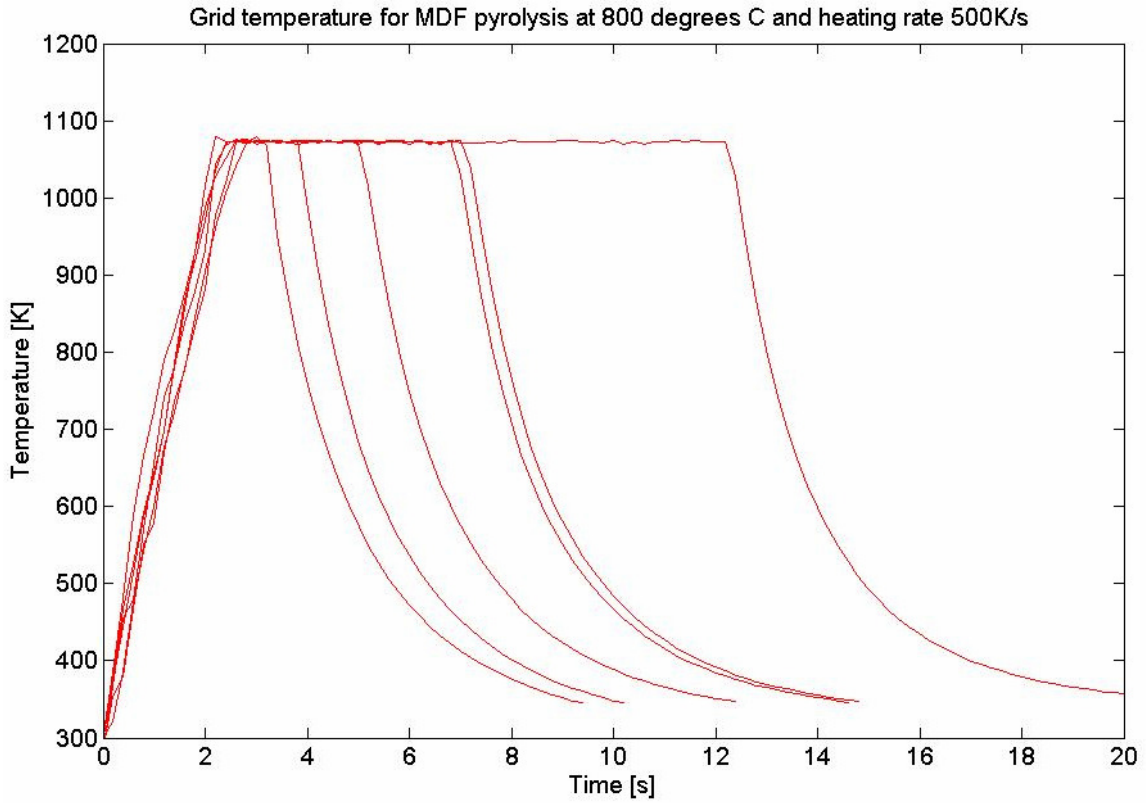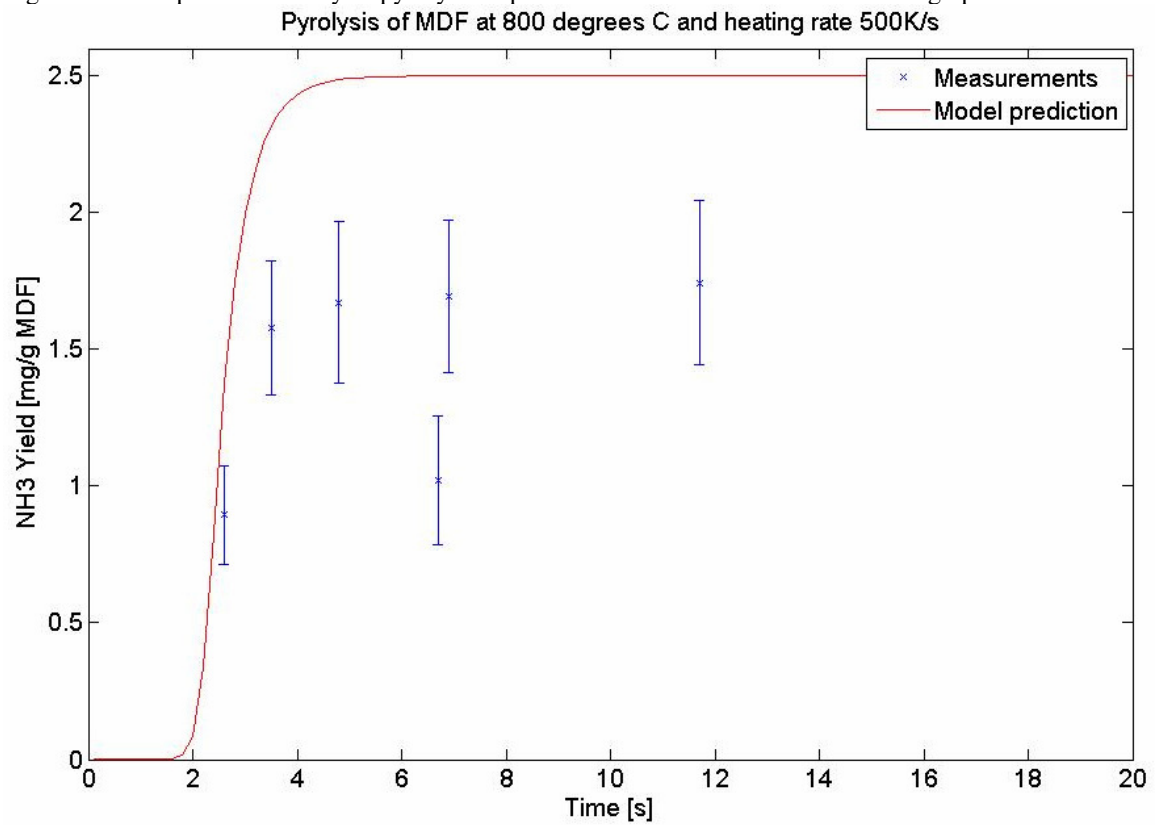Figure 5.3: Normalised measured ammonia yield and maximum yield according to model.

Figure 5.4: Temperature history of pyrolysis experiments of MDF at 800°C and heating up at 500K/s.

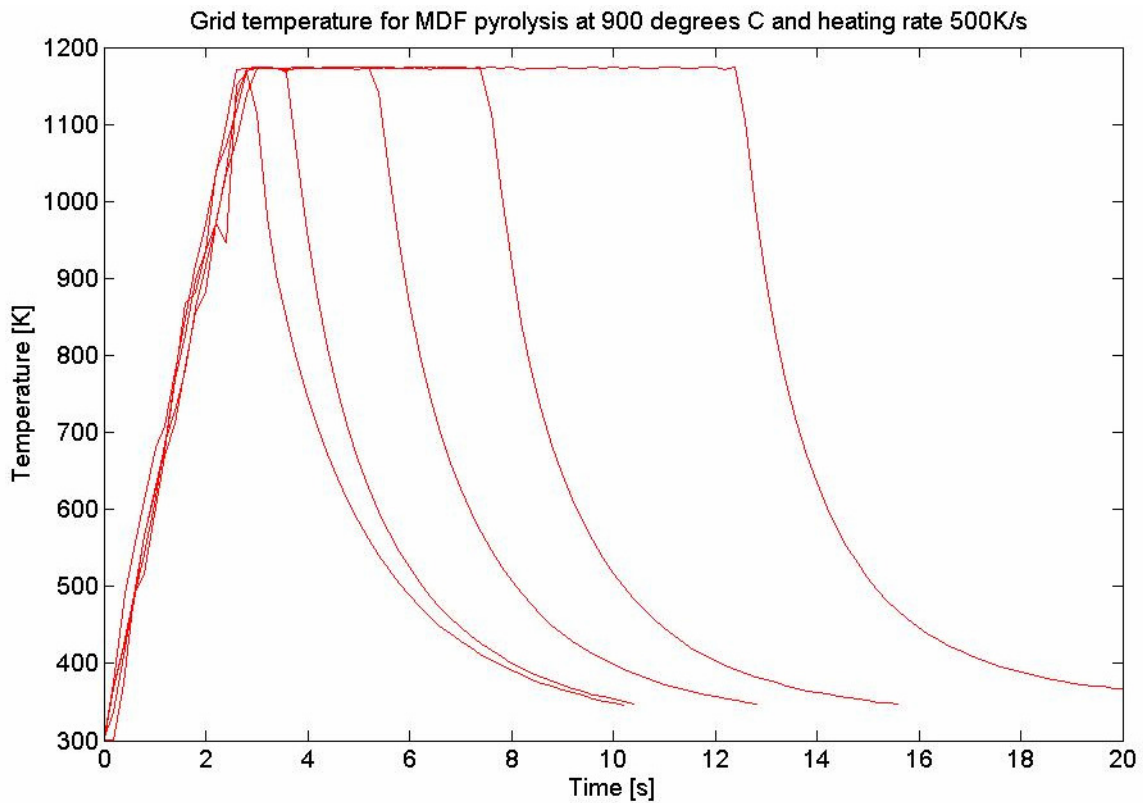Figure 5.5: Normalised measured ammonia yield and maximum yield according to model.

Figure 5.6: Temperature history of pyrolysis experiments of MDF at 900$^{\text{o}}$C and heating up at 500K/s.

Figure 5.7: Normalised measured ammonia yield and maximum yield according to model.
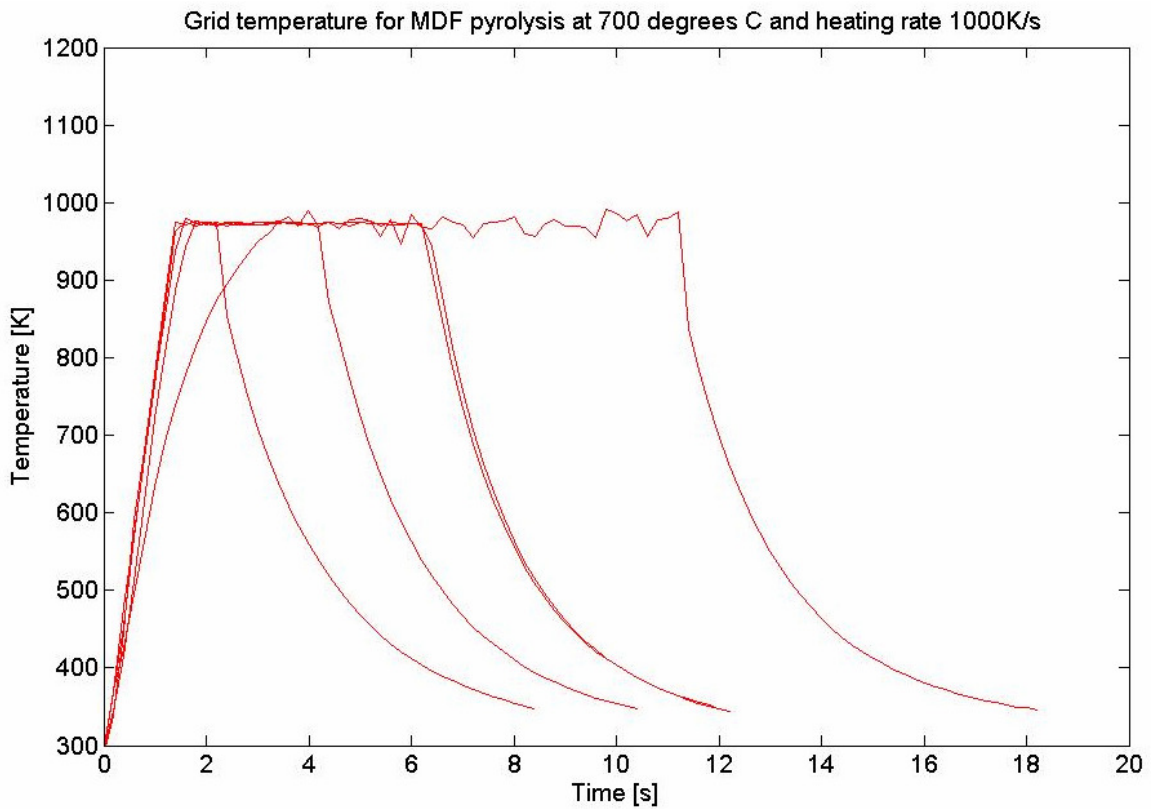
Figure 5.8: Temperature history of pyrolysis experiments of MDF at $700^{O}C$ and heating up at 1000K/s.
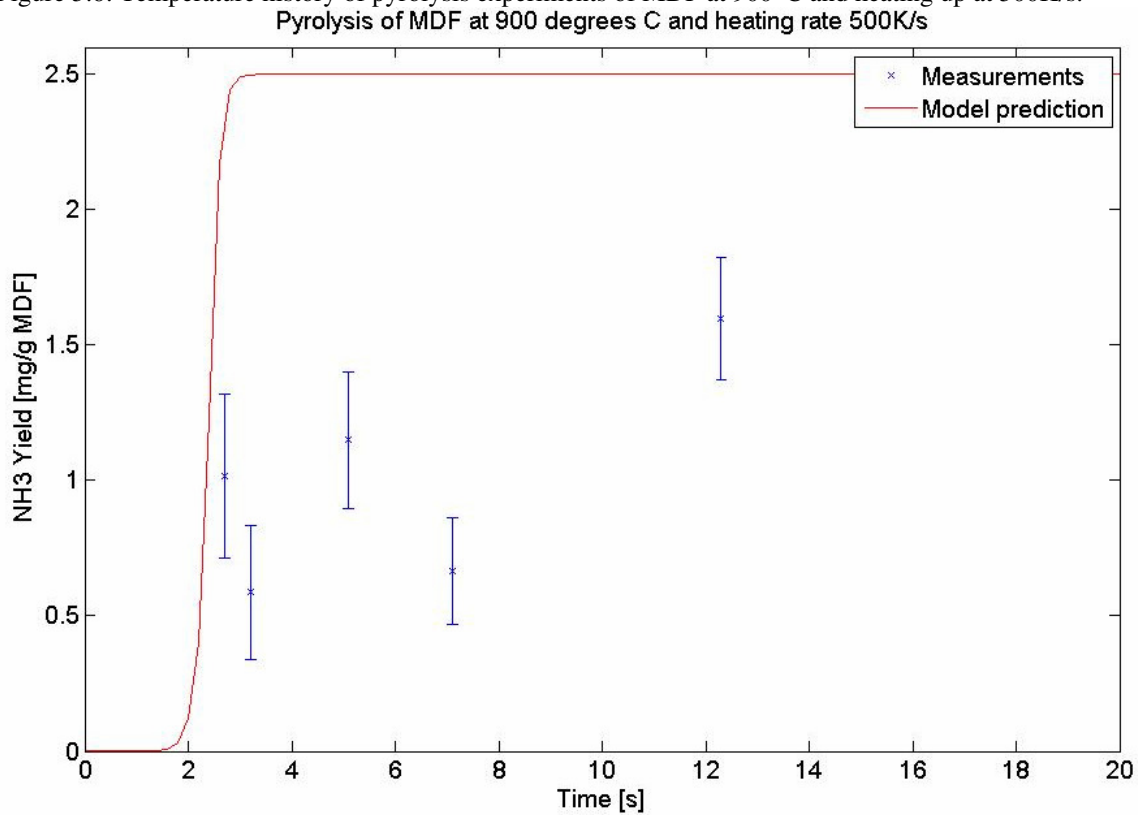

Figure 5.9: Normalised measured ammonia yield and maximum yield according to model.

Figure 5.10: Temperature history of pyrolysis experiments of MDF at $800^{\circ}C$ and heating up at 1000K/s.

Figure 5.11: Normalised measured ammonia yield and maximum yield according to model.

Figure 5.12: Temperature history of pyrolysis experiments of MDF at 900°C and heating up at 1000K/s.

Figure 5.13: Normalised measured ammonia yield and maximum yield according to model..
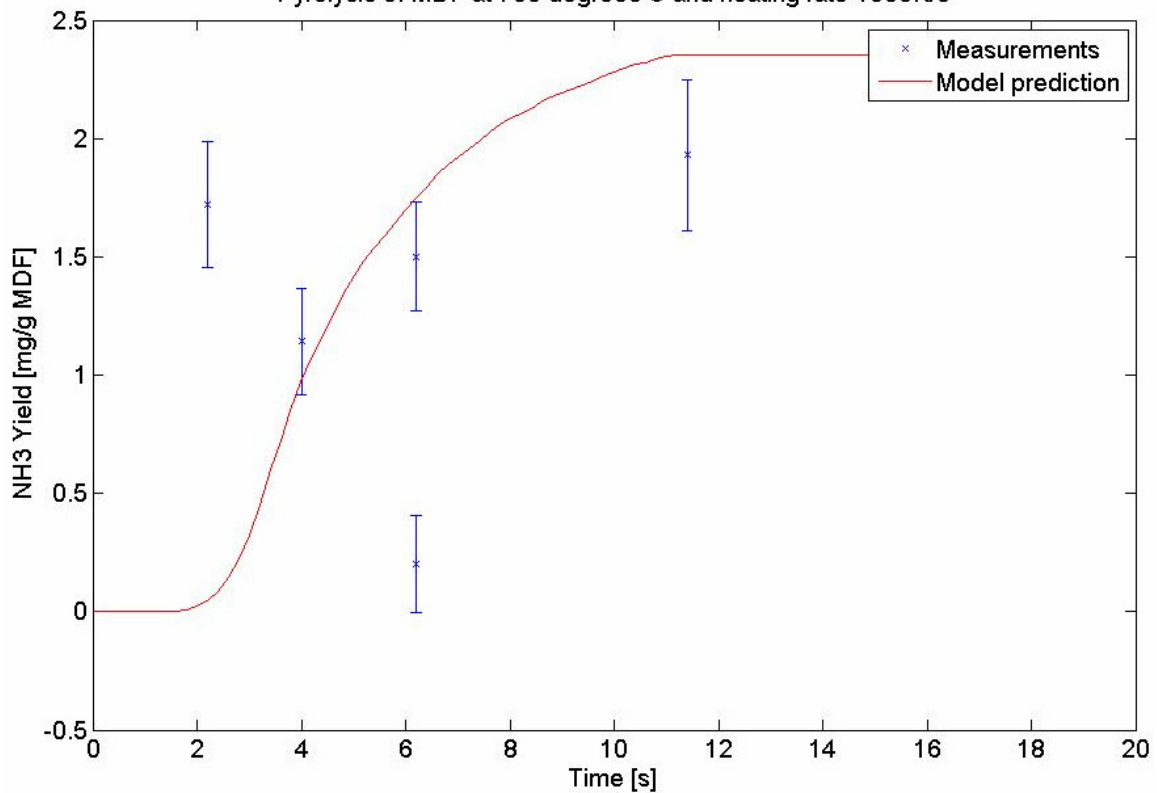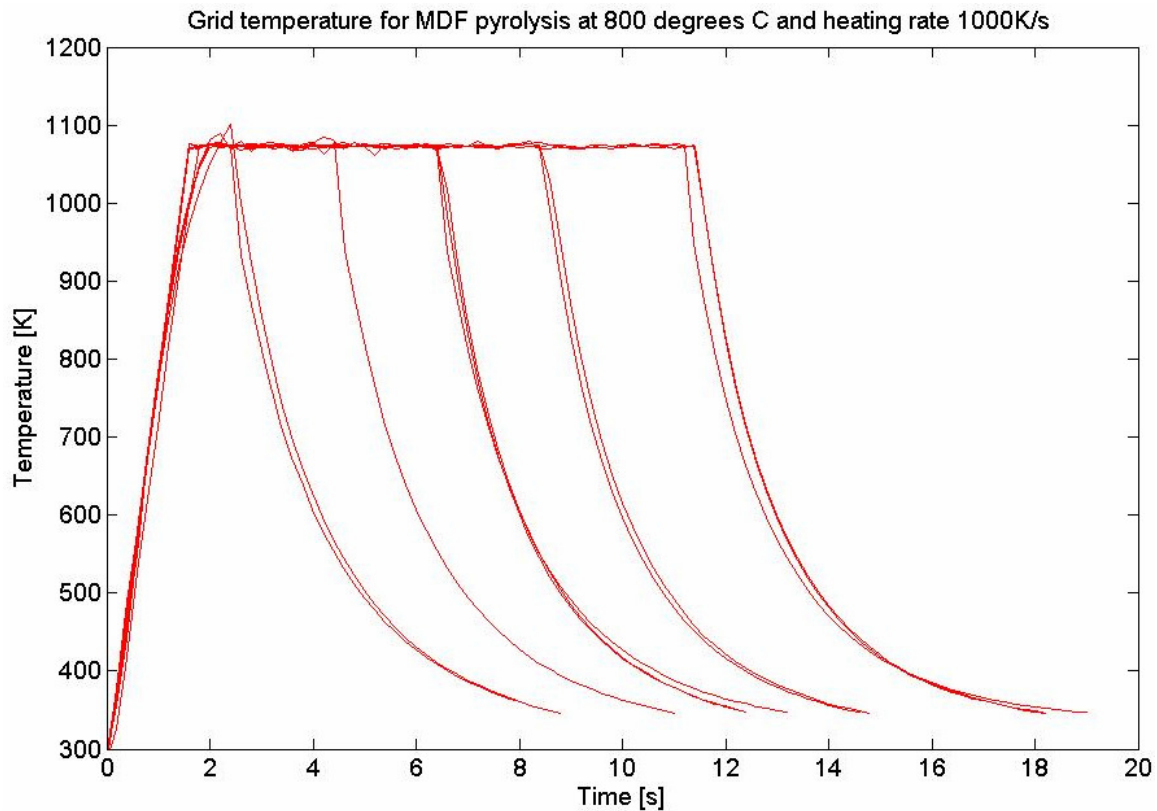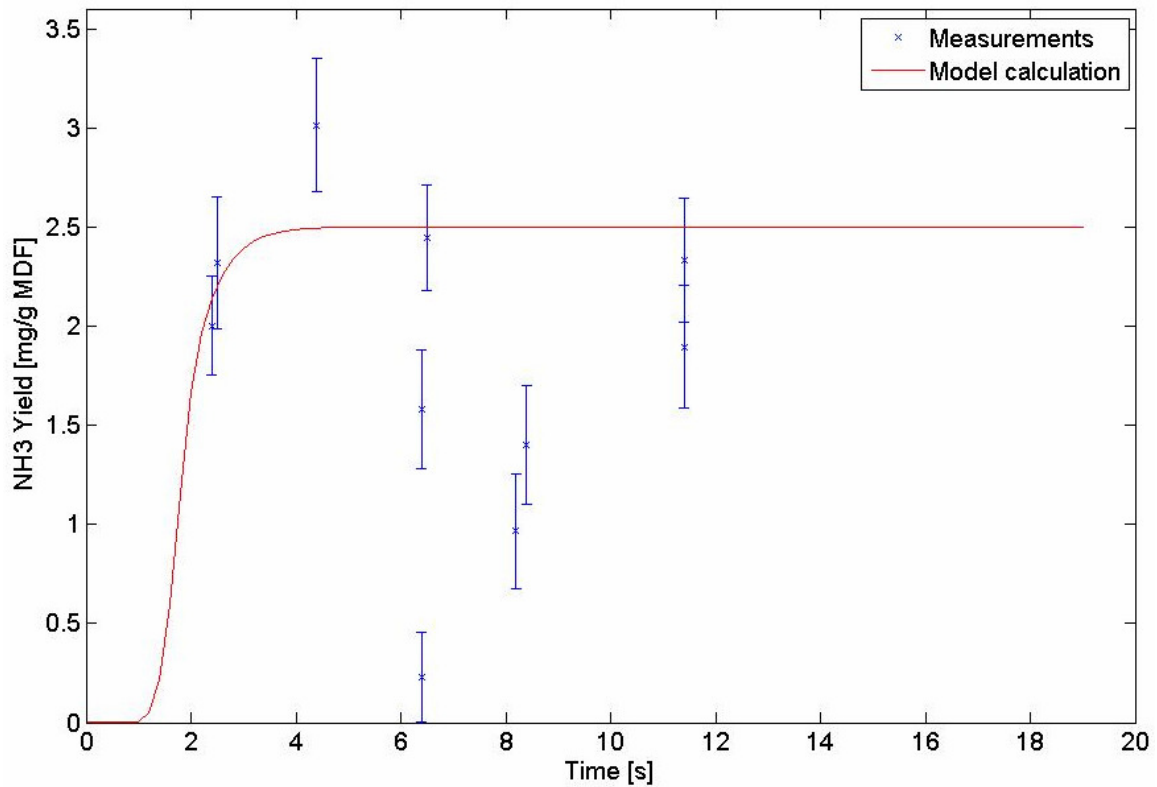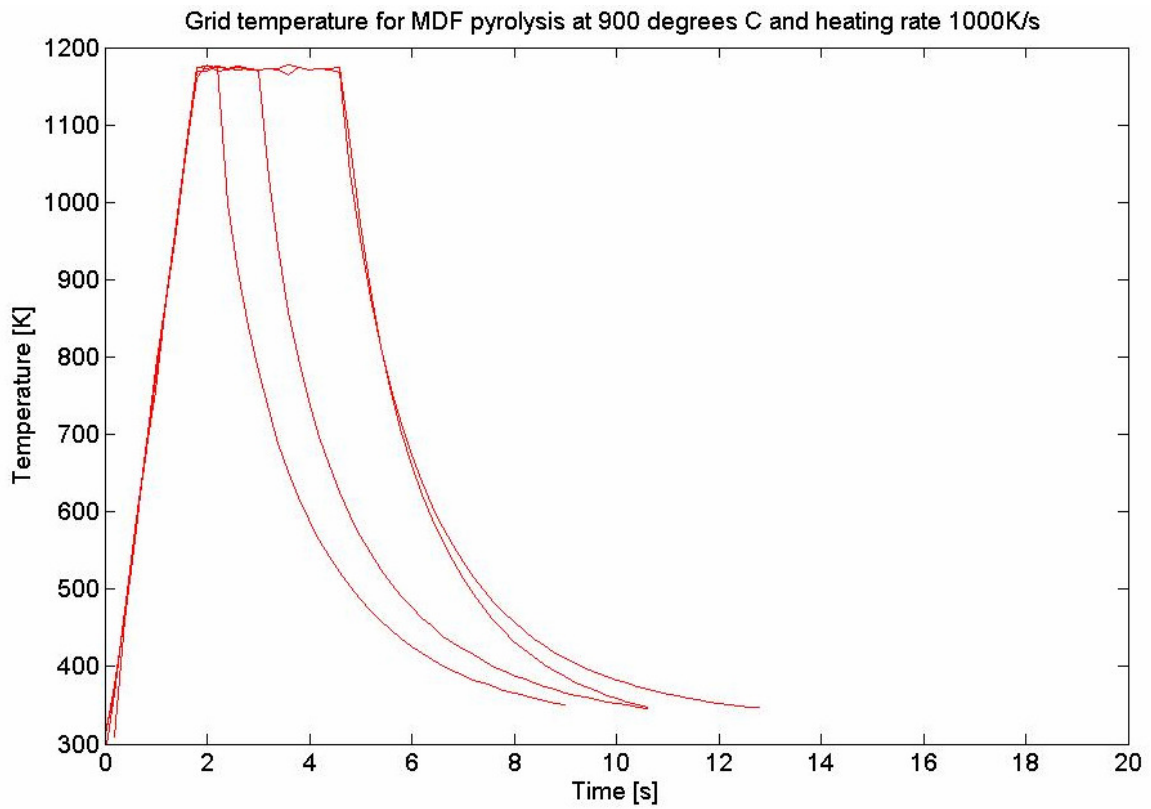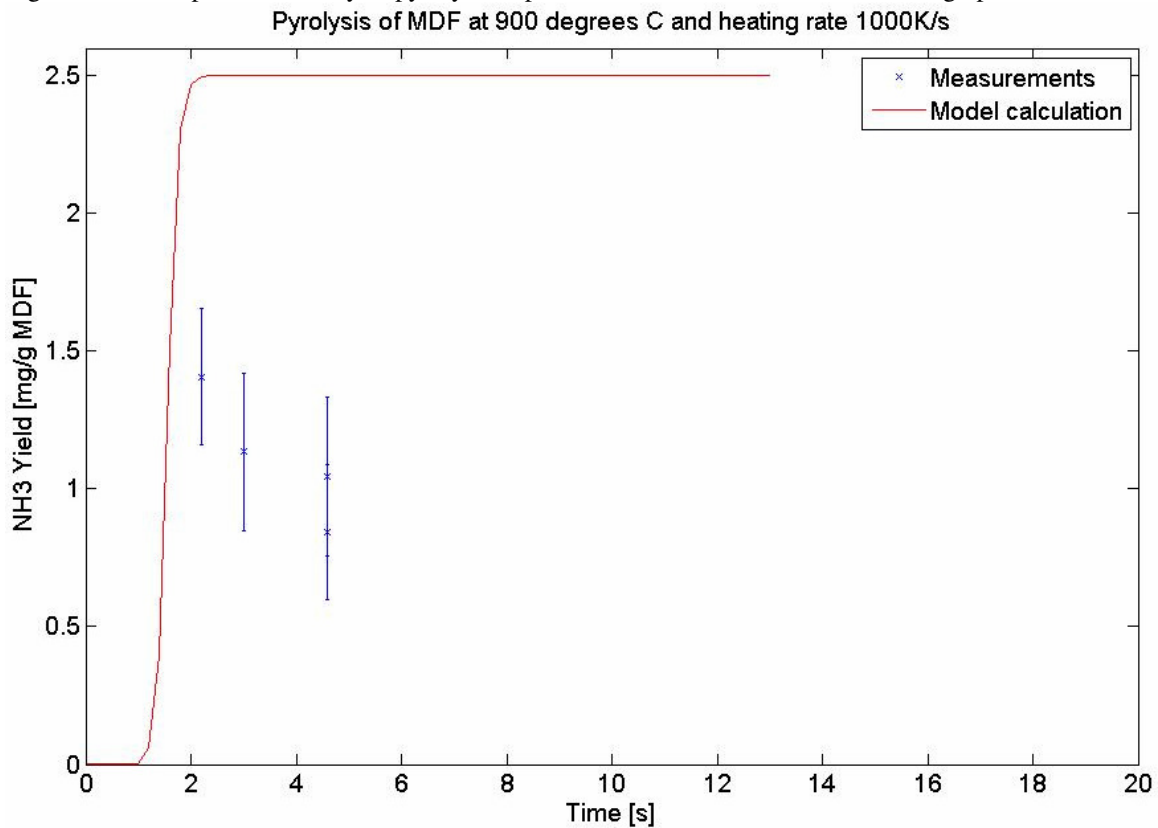
§5.2 Discussion

Urea
As figure 5.1 for pyrolysis of urea shows, the ammonia yield is lowest for 300$^{\text{O}}$C, than increases with temperature (500$^{\text{O}}$C and 700$^{\text{O}}$C) and than goes down again. At 300$^{\text{O}}$C a possible explanation for the low yield of ammonia may be that urea simply vaporizes at this relatively low temperature [24]. As temperature increases more urea will decompose to form products such as NH_3 and HNCO, but also cyanuric acid ($C_3H_3N_3O_3$) and biuret ($C_2H_5N_3O_2$). As temperature increases even further ammination of cyanuric acid may explain the decrease in ammonia yield, as cyanuric acid can bind three ammonia molecules in three consecutive steps to form melamine ($C_3H_6N_6$) and water (H_2O). Another explanation could be that at higher temperatures the conditions are favourable for the thermal decomposition of ammonia, resulting in nitrogen (N_2) and hydrogen (H_2). Thermal decomposition can be explained as follows.

Under certain conditions (on an iron catalyst and at a pressure of 200 bar) the reaction

$$N_2 + 3H_2 \Rightarrow 2NH_3 \tag{5.1}$$

may occur, forming ammonia from nitrogen and hydrogen. Alternatively, when temperature increases this reaction may be inversed, resulting in the thermal decomposition of ammonia. Especially for higher temperatures and longer residence times, i.e. for longer hold times in the experiments, this may occur. The thermal decomposition of ammonia can be explained with the Gibbs free energy and reaction constant for equation 5.1.
The Gibbs free energy is a thermodynamic potential which measures the useful work obtainable from a closed thermodynamic system at constant temperature and pressure. One of the identities of the Gibbs free energy reads

$$\Delta G^0 = -RT \ln(k_p), \tag{5.2}$$

which may be rewritten to

$$-\frac{\Delta G^0}{RT} = \ln(k_p). \tag{5.3}$$

So, if a graph was made with $1/T$ [K] on the horizontal axis and $ln(k_p)$ [-] on the vertical axis and this graph is a straight line, than the slope of the line is $-\Delta G/R$, provided that k_P is greater than 1. When the Gibbs free energy ΔG is below zero, that reaction is favoured and will proceed spontaneously. If ΔG is equal to zero the reaction is reversible and an equilibrium is reached [25].

In case of chemical equilibrium the reaction constant of equation 6.1 may be determined from

$$k_p = \frac{[NH_3]^2}{[H_2]^3[N_2]}. \tag{5.4}$$

In equation 5.4, [X] is the chemical activity of species X. If the value of k_p is above 1, than the reaction as written in equation 5.1 is favourable. If the value of k_p is below 1, the reverse reaction
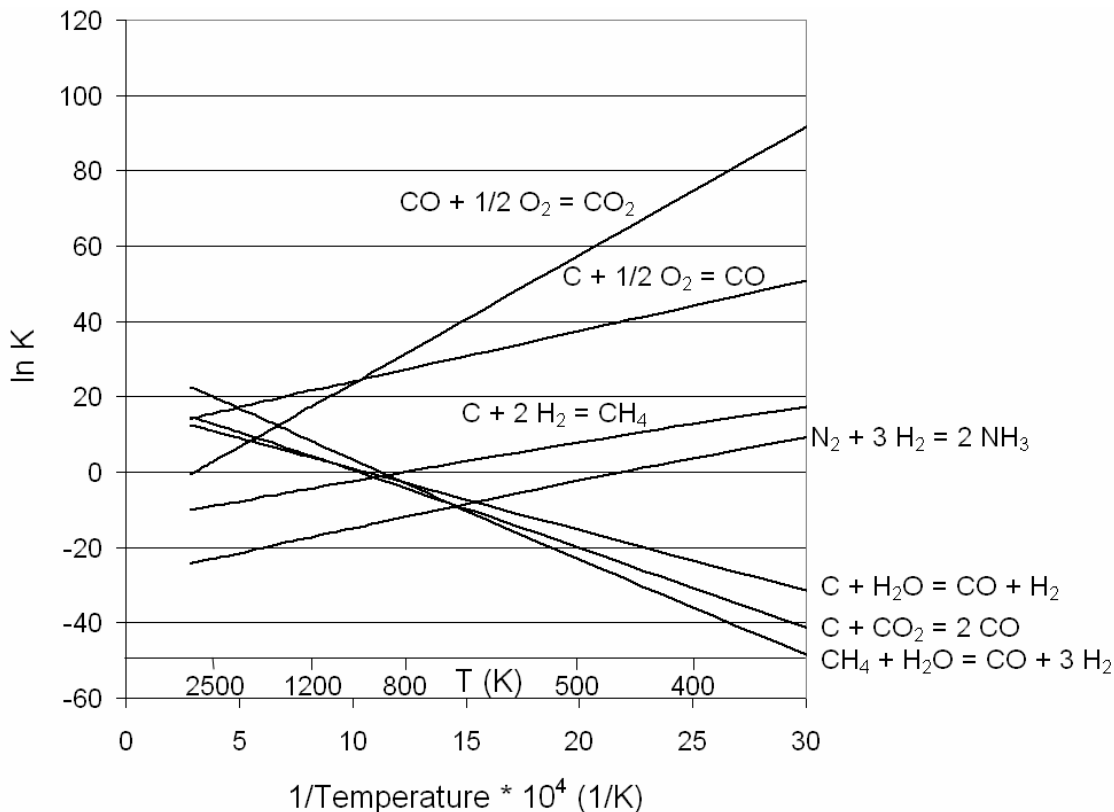
Figure 5.14: Graph of *ln(K)* as a function of *1/T* using the Gibbs free energy, for several chemical reactions.

is favourable, resulting in decomposition of NH_3. With the values for the Gibbs free energy well tabulated for the substances of interest here, the difference in Gibbs free energy ΔG can be determined for equation 5.1 for different temperatures, and the reaction constant k_p can be calculated. This has been done for several reactions, including the one described by equation 5.1 and is depicted in figure 5.14.

As the figure shows, the value of $ln(k_p)$ is zero for a temperature of about 450K, or 180^oC, and has a negative value for higher temperatures. This is a relatively low temperature which is quite likely to be reached in the gas formed by pyrolysis of urea, especially at higher end temperatures and for longer hold times when secondary reactions are more likely to occur. So, thermal decomposition of ammonia could be an explanation for the lower yields than theoretically possible.

Ammonia could also have a tendency to stick to the walls of the reactor, or the gas cell used earlier, which may explain the decrease of ammonia concentration in time.

Furthermore, ammonia pyrolysis at higher temperatures resulting in NH_i radicals and decreasing NH_3 yields is suspected [26] and nickel, which is present in stain less steel, may have a catalytic effect on the decomposition of NH_3 [27].

MDF

For pyrolysis of MDF the conditions that have been investigated were pyrolysis final temperatures of 700^oC, 800^oC and 900^oC, with heating rates of 500K/s and 1000K/s and hold times of 1,3,5 and 10 seconds. About the heating rates it can be said that the ammonia yield increases with heating rate, since the yields at 1000K/s are higher for almost all experiments compared to the rate of 500K/s. This seems to be in accordance with [29].

With respect to pyrolysis final temperature it can be seen that at 700^oC reactions proceed slowly and ammonia yield is far from maximum. With increasing final temperature the kinetics of

ammonia also seems to increase, resulting in higher yields. However, at higher temperatures possibly thermal decomposition or catalytic effects by the grid reduce the ammonia yield, similar to the case for urea.

In most cases a longer hold time results in a higher ammonia yield. Although this is a rather crude method, this may be seen as evidence that off-line determination of ammonia release rate is indeed possible.

§5.3 Modelling

In figures 5.3, 5.5, 5.7, 5.9, 5.11 and 5.13 the result of the simple model by Anthony, et al. [4], see paragraph 2.5, is also drawn. The parameters that are needed for these model results are a maximum ammonia yield V^*, an activation energy E and an apparent frequency factor k_0, also known as pre-exponential factor. The activation energy is a constant for a certain volatile species, and V^* should be constant too. So, once these are determined only the pre-exponential factor k_0 can be used to fit the model to the measurement data. In figure 5.15 this is done for several values of k_0 and the measurement data of pyrolysis of MDF at 800^OC at a heating rate of 1000 K/s.

The parameters that have been found to give the best model results are a maximum ammonia yield V^* of 0.25 wt% and an activation energy E of 153 [kJ/mol] [30]. For the value for the pre-exponential factor k_0 figure 5.15 has been used. This factor has been determined to be 7×10^7 [1/s]. The value for the activation energy is actually for ammonia release from *Miscanthus Giganteus* under slow pyrolysis conditions, but as the graphs show the results are acceptable.
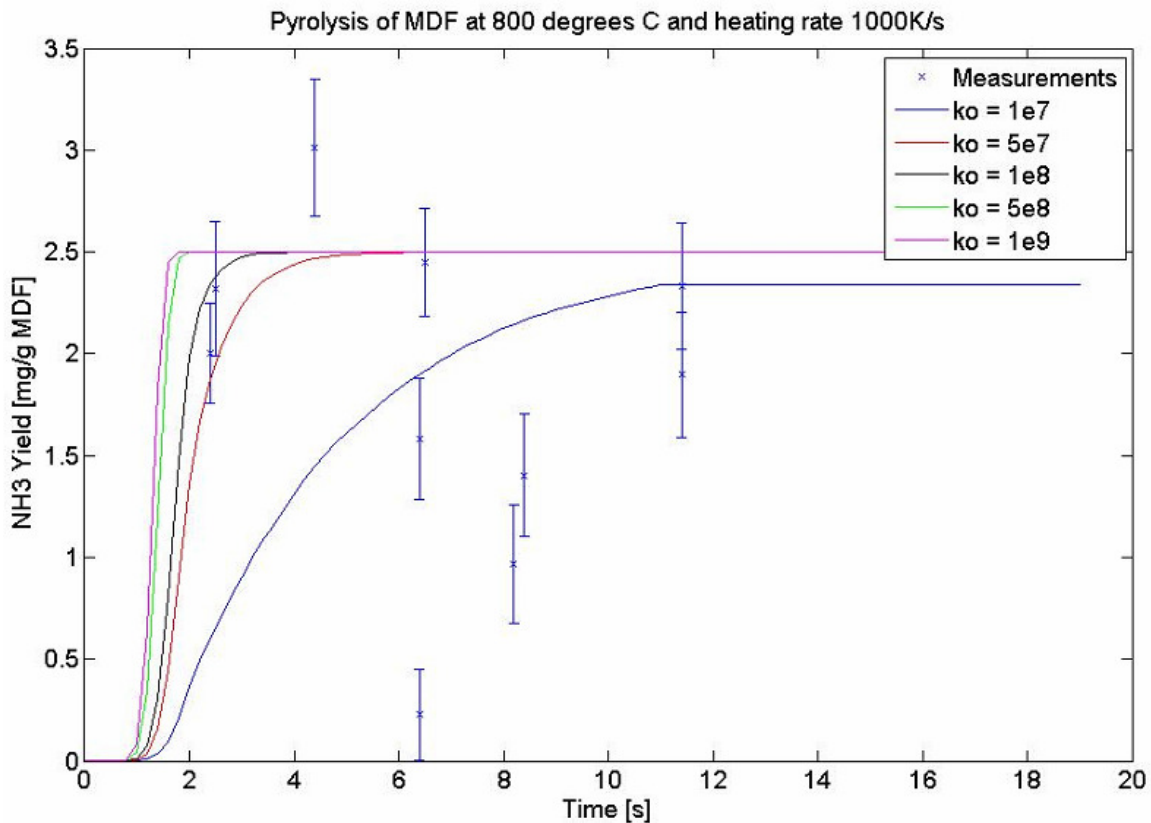

Figure 5.15: Measurement data of pyrolysis of MDF at 800^OC, heating rate of 1000 K/s with model predictions for several values of the pre exponential factor k_0.

44

Table 5.1: Proximate and ultimate analysis of MDF (weight percentages on dry and ash free basis). Analysis performed at IVD – Fuels and Measurement Technology, Institute of Process Engineering and Power Plant Technology, University of Stuttgart [31].

	C	H	N	O	Volatiles	Fixed carbon
MDF	48.45wt%	7.99wt%	3.83wt%	39.73wt%	83.69wt%	16.31wt%

Table 5.2: Some values of molar masses.

Species	Molar mass [g/mol]
Carbon	12.0107
Hydrogen	1.00794
Nitrogen	14.0067
Oxygen	15.9994
Ammonia	17.0304

Maximum yield

All kinds of ammonia yields have been determined during the experiments. For the model described in paragraph 2.5 the value of V^*, the maximum ammonia yield at time t = ∞, needs to be known. From the experiments the most common highest yield of ammonia from MDF has been chosen for V^*. This yield occurs for pyrolysis with an end temperature of 800°C and a heating rate of 1000K/s, and is approximately 0.25wt%, see figure 5.12. If it is assumed that this value of 0.25wt% is indeed the maximum ammonia yield for MDF, than the amount of nitrogen from the sample that is transformed into ammonia can be calculated. First, the molar mass of MDF needs to be calculated with

$$\sum_i X_i \cdot M_X ,$$
(5.5)

where X_i represents the weight percentage of a certain species in the MDF and M_X is the molar mass of that species. From [31] the composition of the MDF that is used can be found, see table 5.1, and in table 5.2 the molar masses of the species of interest can be found.

Substituting the values of tables 5.1 and 5.2 into equation 5.5 results in a molar mass for MDF of

$$\sum_i X_i \cdot M_X = 0.4845 \cdot 12.0107 + 0.0799 \cdot 1.00794 + 0.0383 \cdot 14.0067 + 0.3973 \cdot 15.9994$$
$$= 12.7927[g/mol].$$

So, with a molar mass of 12.7927 g/mol and a nitrogen content of 3.83wt%, there is 0.002994 mol of N in 1 gram of MDF. If this creates 0.25wt% ammonia, that means that 1.4680×10^{-4} mol of ammonia is formed. Dividing these figures than gives the amount of fuel-nitrogen n_{NinMDF} that is transformed to ammonia $n_{ammonia}$

$$\frac{n_{ammonia}}{n_{NinMDF}} = \frac{1.4680 \cdot 10^{-4}}{0.002994} = 0.0490 = 4.9\% .$$
(5.6)

So, a maximum of almost 5% of the nitrogen present inside the fuel is converted to ammonia.

Chapter 6   Conclusions and recommendations

The pyrolysis conditions that have been investigated for this project were pyrolysis final temperatures of 700°C, 800°C and 900°C, with heating rates of 500K/s and 1000K/s and hold times of 1,3,5 and 10 seconds. The samples consisted of MDF in powder form, or urea in the form of small spheres. The use of melamine as a model compound turned out to be difficult in this set up. The yields of ammonia from urea were much higher than those of MDF, as is to be expected considering the nitrogen content of urea (46wt%) and MDF (3.83wt%).

Both MDF and urea showed an increase in ammonia yield with increasing temperature, up to a certain temperature where the yield reaches a maximum. The highest achieved yield was at 800°C for MDF and at 700°C for urea. If the temperature was increased further than these 'optimal' temperatures, the ammonia yield went down again. This may be explained by thermal decomposition of ammonia (see figure 5.2), formation of NH_i radicals by pyrolysis of ammonia [25], the presence of catalytic effects of nickel or possibly other substances in the grid [26,32,33], or by secondary reactions which consume NH_3.

The ammonia yields at 1000K/s are higher for almost all experiments compared to the rate of 500K/s, so higher heating rates seems to result in higher ammonia yields.
With respect to pyrolysis final temperature it can be seen that at 700°C reactions proceed slowly and ammonia yield is far from maximum. With increasing final temperature the kinetics of ammonia seems to increase, resulting in higher yields. However, at temperatures exceeding a certain maximum the ammonia yield goes down again for both MDF and urea.
In most cases a longer hold time results in a higher ammonia yield. Although this is a rather crude method, this may be seen as evidence that off-line determination of ammonia release rate is indeed possible.

The model parameters for the simple first order model proposed by D.B. Anthony in paragraph 2.5 are a maximum ammonia yield V^* of 0.25 wt%, an activation energy E of 153 [kJ/mol] and an apparent frequency factor k, also known as pre-exponential factor, of 7×10^7 [1/s]. The value for the activation energy is actually for ammonia release from *Miscanthus Giganteus* under slow pyrolysis conditions [30], but the results for ammonia release from MDF seem to be acceptable.

The set up that has been built for this project and the method developed to conduct experiments may be used to investigate the release rate of ammonia from MDF and other biomass feed stocks. With the results of experiments it should be possible to improve the prediction of formation of NO_x and NO_x precursors in biomass fueled grate furnaces. With these models the allocation of biomass grate furnaces for generation of electricity is simplified, thus enabling transition to a more sustainable energy supply.

Recommendations for future work

- More measurements may be done to improve the model parameters found in this project. Especially the activation energy may be investigated, since its value is not accurately determined for the conditions of pyrolysis used here. Similarly, the volatile yield V^* at time t $= \infty$ may need to be determined more accurately.
- Experiments using a platinum grid may give higher ammonia yields, as there should be less catalytic effects with a platinum grid.

- Extensions of the quantification method to also determine hydrogen cyanide (HCN) yield would be a great benefit, because than all likely precursors of NO_x can be measured and the model for precursor release could be made more complete.
- The simple first order model could be extended in such a way that k_0 and E are automatically adjusted during the simulated pyrolysis process. Since the composition of the fuel changes during pyrolysis it seems likely that E and k_0 change, and therefore the reaction rate changes. By modelling this behaviour, better simulation results are expected.

Literature

[1]   D.H. meadows, et al., "*Limits to growth*", Universe Books, 1972

[2]   The World Commission on Environment and Development "*Our common future*", Oxford University Press, 1987

[3]   http://navier.ist.utl.pt/opticomb (OPTICOMB project, homepage)

[4]   D.B. Anthony, et al. "*Rapid devolatilization of pulverized coal*", Fifteenth International Symposium on Combustion, The Combustion Institute, Pittsburgh, Pa (1975)

[5]   Picture from http://www.gtsenergy.com/products/solid_fuel/reciprocating.asp , on 9-11-2006

[6]   M. Geurds, "*Spectroscopic gas analysis of slow biomass pyrolysis*", Graduation report June 2004, Report number WVT 2004.05

[7]   A. Bridgwater et al., "*Fast pyrolysis of biomass: a handbook*", Antony Rowe Ltd., 1999, 14-15

[8]   M.J. Aho, J.P. Hämäläinen, J.L. Tummavuori, "*Conversion of peat and coal nitrogen through HCN and NH$_3$ to nitrogen oxides at 800°C*", Fuel 1993 Volume 72 Number 6 837-841

[9]   P. Glarborg, A.D. Jensen, J.E. Johnsson, "*Fuel nitrogen conversion in solid fuel fired systems*", Progress in Energy and Combustion Science 29, 89-113, 2003

[10]   T.B. Reed, "*A survey of biomass gasification II. Principles of gasification*", Springfield: National Technical Information Service, 1979

[11]   M.J. Antal, G. Varhegyi, "*Cellulose pyrolysis kinetics: the current state of knowledge*",Ind. Eng. Chem. Res. 34 (1995) 703

[12]   Alpert, Keiser, Szymanski, *"IR: theory and practice of infra red spectroscopy"*, Second edition, Plenum Press, 1964 (1970).

[13]   C.N. Banwell, *"Fundamentals of molecular spectroscopy"*, Second Edition, McGraw-Hill Book Company, 1972, 65-118

[14]   Rothman, et al., *"The HITRAN 2004 molecular spectroscopic database"*, Journal of Quantitative Spectroscopy and Radiative Transfer 96 (2005) 139-204

[15] Houghton, Smith, *"Infra-red physics"*, Oxford university press, 1966

[16] Smith, "*Fundamentals of Fourier transform infrared spectroscopy"*, CRC press, 1996, 55-85, 139-154.

[17] JavaHAWKS software, uses HITRAN 2004 database, downloadable from http://www.cfa.harvard.edu/HITRAN/

[18] L.S. Rothman, et al., *"The HITRAN molecular spectroscopic database and HAWKS (HITRAN Atmospheric WorKStation) 1996 edition"*, J. Quant. Spectrosc. Radiat. Transfer **60**, 665-710, (1998).

[19] S.S. Penner, *"Quantitative molecular spectroscopy and gas emissivities"*, Addison-Wesley, Reading MA, 1959.

[20] D.P. Edwards, M. Lopez-Puertas, M.A. Lopez-Velverde, *"Non-local thermodynamic equilibrium studies of the 15-μm bands of CO_2 for atmospheric remote sensing"*, J. Geophys. Res. 98, 14955-14977,(1993).

[21] J. Guo, "Pyrolysis of wood powder and gasification of wood-derived char", Technische Universiteit Eindhoven, 2004. Thesis, ISBN 90-386-1935-9.

[22] D. Deen, "*On-line ammonia release rate measurements during biomass pyrolysis*", 2006.

[23] www.DeltaPowerSupplies.com

[24] P.M. Schaber, et al., "*Study of the urea thermal decomposition (pyrolysis) reaction and importance to cyanuric acid production*", American Laboratory, August 1999.

[25] C.G. Hill Jr., "*An introduction to chemical engineering kinetics and reactor design*", John Wiley and sons, Inc., 9-15, 1977.

[26] A.A. Konnov, J. De Ruyck, "*Kinetic modelling of the thermal decomposition of ammonia*", Combst. Sci. and Tech., Vol. 152, 23-37, 2000.

[27] R.W. McCabe, "*Kinetics of ammonia decomposition on nickel*", Journal of Catalysis, 79, 445-450, 1983.

[28] L. Costa, G. Camino, "*Thermal behaviour of melamine*", J. of Them. Anal., Vol. (34), 423-429, 1988.

[29] L.L. Tan, C-Z. Li, "*Formation of NO_x and SO_x precursors during the pyrolysis of coal and biomass. Part II. Effect of experimental conditions on the yields of NO_x*

and SO$_x$ precursors from the pyrolysis of a Victorian brown coal", Fuel 79, 1891-1897, 2000.

[30]   W. de Jong, et al., "*Heated grid flash pyrolysis of Miscanthus with in-situ infrared spectrometry species analysis and comparison with FG-DVC biomass model simulations*", Pyrolysis and gasification of biomass and waste, Proceedings of an expert meeting, 111-123, 2002

[31]   A. Toland, et al., "*Kinetics of CO release from bark and medium density fibreboard pyrolysis*",

[32]   S.M. Beck, "*Cell coatings to minimize sample (NH$_3$ and N$_2$H$_4$) adsorption fr low-level photo-acoustic detection*", Applied Optics, 24, 1761-1763, 1985.

[33]   C.Z. Li, P.F. Nelson, Fuel, 75, 525-526, 1996

[34]   P.M. Morse, "*Diatomic molecules according to the wave mechanics. II. Vibrational levels*", Phys. Rev. 34, 57-64, 1929

[35]   A.S. Filler, "*Apodization and interpolation in Fourier-transform spectroscopy*", J. Opt. Soc. Am. **54**, 762-767, (1964).

[36]   R. H. Norton, R. Beer, "*New Apodizing Functions for Fourier Spectrometry*", J. Opt. Soc. Am. **66**, 259-264 (1976).

[37]   www.thermocoax.com on 17-10-2006.

[38]   User's Manual KUSB3102/8-900-01 Rev. A / January 2005, from www.Keithley.com, or www.keithley.com/search?searchType=general&SearchableText=KUSB+3108

List of symbols

Symbol	Description
B	Spectral intensity
$B_{\eta\eta'}$	Einstein coefficient for induced absorption [$cm^3/(ergs\ s^2)$]
E_η	Lower state energy [cm^{-1}]
J	Rotational energy level [-]
I	(Interferogram-) intensity
I_a	Natural terrestrial isotopic abundance [-]
N_A	Avogadro's number [molecule/mol]
N	Molecular number density [cm^{-3}]
Q	Total internal partition sum [-]
R	Universal gas constant [cm^3 atm/mol K]
$S_{\eta\eta'}$	Spectral line intensity [$cm^{-1}/(molecule\ cm^{-2})$]
a	Absortivity [cm^2/mol]
b	Path length through a (gas) sample [cm]
c	Component concentration [mol/cm^3]
c	Speed of light [m/s]
c_2	Second radiation constant, $c_2 = hc/k = 1.4388$ [cm K]
g_η and $g_{\eta'}$	Lower and upper state statistical weights, respectively [-]
h	Planck's constant [ergs s]
i	Number of components to be analysed [-]
k	Discrete value for wave number σ [cm^{-1}]
n	Discrete value for retardation δ [cm]
n_{air}	Coefficient of temperature dependence of the air-broadened half width [-]
n_η and $n_{\eta'}$	Populations of the lower and upper states, respectively [cm^{-3}]
p_s	Substance partial pressure[atm]
v	Translation velocity of the moving mirror [cm/s]
v	Vibration energy level [-]
x_e	Anharmonicity constant (for rotating vibrator) [-]
$Я_{\eta\eta'}$	Weighted transition-moment squared [ergs cm^3]
Δv	Change in vibrational energy level [-]
ΔJ	Change in rotational energy level [-]
δ	Retardation, optical path difference [cm]
ε_v	Vibrational energy level [cm^{-1}]
λ	Wavelength [μm]
γ_{air}	Air-broadened halfwidth at half maximum [cm^{-1}/atm]
γ_{self}	Self broadened halfwidth at half maximum [cm^{-1}/atm]
υ	Wave number [cm^{-1}]
$\upsilon_{\eta\eta'}$	Spectral line intensity transition frequency [cm^{-1}]
ω_{osc}	Vibrational-rotational frequency [cm^{-1}]
ω_e	Equilibrium oscillation frequency [cm^{-1}]

Appendices

Appendix A   Extending the simple first order model

In biomass pyrolysis a number of reactions like the one described by equation 2.7 occur simultaneously, each with its own values for k_o, E_i and V_i^* as indicated by equation 2.8 and 2.9. By modelling as many reactions as accurately as possible and by summing all these processes, a good estimation of the total pyrolysis yield may be possible. The required values for the variables must be obtained experimentally, and for that the test set-up built for this project can be used. The problem of determining the values of these variables is increased by the number of reactions that occur.

Since a model is being created it is allowed to make simplifications, one of which is to assume that the k_i's (equation 2.8) differ only in activation energy E, and that the number of reactions is large enough to permit E to be expressed as a continuous distribution function [4]. Let F represent the fraction of potential volatile loss V^* which has an activation energy less than E, and let dF/dE equal the distribution function $f(E)$. Now, V_i^* becomes a differential part of the total V^* and may be written as

$$dV^* = V^* dF = V^* f(E)dE, \tag{A.1}$$

with

$$\int_0^\infty f(E)dE = 1. \tag{A.2}$$

The total amount of volatile material yet unreleased can now be obtained by summing the contributions of all reactions, or by integrating equation 2.16 over all values of E using equation A.2. Thus,

$$V^* - V = V^* \int_0^\infty \exp\left(-\int_0^t k(E)dt\right) f(E)dE. \tag{A.3}$$

Distribution $f(E)$ is unknown, but assumed to be Gaussian, with mean activation energy E_o and standard deviation σ. Next it is assumed that the frequency factor $k(E)$ is not a function of E. Equation (A.3) can now be rewritten as

$$V^* - V = \frac{V^*}{\sigma(2\pi)^{1/2}} \int_{-\infty}^\infty \exp\left(-\int_0^t k(E)dt\right) \cdot \exp\left(\frac{(E - E_o)^2}{2\sigma^2}\right) dE \tag{A.4}$$

Note that in the previous equation the lower limit has changed from zero to minus infinity. This has a negligible numerical effect. Substituting equation 2.8 for $k(E)$ finally results in

$$V^* - V = \frac{V^*}{\sigma(2\pi)^{1/2}} \int\limits_{-\infty}^{\infty} \exp\left[-k_o \int\limits_{0}^{t} \exp(\frac{-E}{RT})dt + \frac{(E-E_o)^2}{2\sigma^2} \right]dE .$$

(A.5)

This equation now describes an infinite set of parallel equations, because the single overall activation energy is replaced by a distribution with mean E_o and standard deviation σ. After experiments have been conducted to obtain values for V^*, k_o, E_o and σ for all products formed by pyrolysis, equation A.5 can be used to calculate the total volatile yield of pyrolysis product gas from a certain type of biomass.

Appendix B   Branches

Molecules consist of atoms which are bonded chemically. Due to the elasticity of these bonds the positions of the atoms with respect to each other is not fixed, but may vary by some amount, depending on the energy of the molecule. That the molecular energy may vary is most easily understood by considering the forces at play inside a molecule. There is a repulsive force between the positively charged nuclei of the atoms of a molecule, and also between the negatively charged electron clouds surrounding the atoms. But, there is also an attractive force between the nuleus of one atom and the electrons of another. The atomic distance will be such that these two forces balance each other and the energy of the system as a whole is at a minimum. If the atoms are pressed closed together the energy of the system will increase rapidly by an increase in repulsive force, if the atoms are pulled apart the energy increases due to an increase in attractive force. Either way, changing the mean internulear distance requires an input of energy, as shown in figure B.1 for a diatomic molecule [13].

Figure B.1 shows two atoms, A and B. Atom A is fixed at r = 0, so the position of B oscillates between B' and B" and shows the interatomic distance between A and B. As the figure shows the mean bond length r_{eq} does not change with increasing energy, but the motion of atom B becomes more vigorous.

The frequency at which the atoms vibrate is dependent on the mass of the system and a certain force constant, like in a spring. The oscillation frequency is than given by

$$\omega_{osc} = \frac{1}{2\pi}\sqrt{\frac{k}{\mu}}[Hz].$$
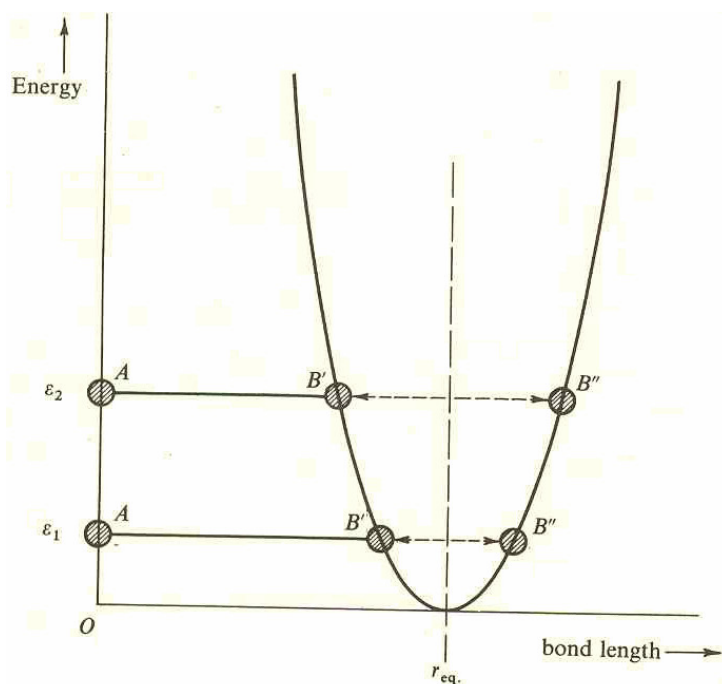(B.1)

Figure B.1: Parabolic curve relating a change in bond length between two atoms to the energy required to change it.

In equation B.1 μ is the reduced mass of the system ($m_1 m_2/(m_1+m_2)$) and k the force constant of the system. In spectroscopy it is common to use wavenumber in stead of frequency. Wavenumber is the number of waves of a certain wavelength in one centimetre. It is sometimes called frequency, since it is directly linked to it, and has unit [cm^{-1}] in stead of the usual unit for frequency, [Hz]. To calculate the oscillation frequency in wavenumber, all that needs to be done is divide the frequency in [Hz] by the speed of light c in [cm/s], resulting in

$$\omega_{osc} = \frac{1}{2\pi c}\sqrt{\frac{k}{\mu}}[cm^{-1}]. \tag{B.2}$$

Like all other molecular energies, vibrational energies are quantised. The Schrödinger equation, describing the space- and time-dependence of quantum mechanical systems, may be used to calculate the vibrational energies for any particular system. For a simple harmonic oscillator the solution is

$$\varepsilon_v = (v+\frac{1}{2})\omega_{osc}[cm^{-1}]. \tag{B.3}$$

In equation (B.3) v is the vibrational quantum number. As the equation shows, the lowest energy level is $\varepsilon_0 = \omega_{osc}/2$ for $v = 0$. This means there is always a certain minimum amount of vibrational energy, the so called zero-point energy, and two atoms are never completely at rest with respect to each other. The zero-point energy depends only on the vibration frequency and hence on the strength of the chemical bond and the atomic masses. Figure B.2 shows some of the solutions to equation B.3.
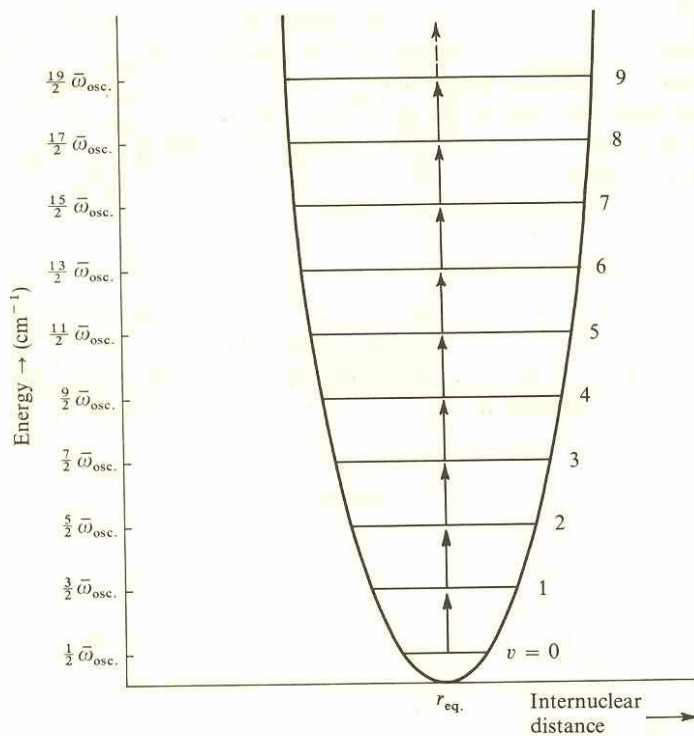

Figure B.2: Allowed vibrational energy levels and transitions between them for a diatomic molecule, undergoing simple harmonic motion.
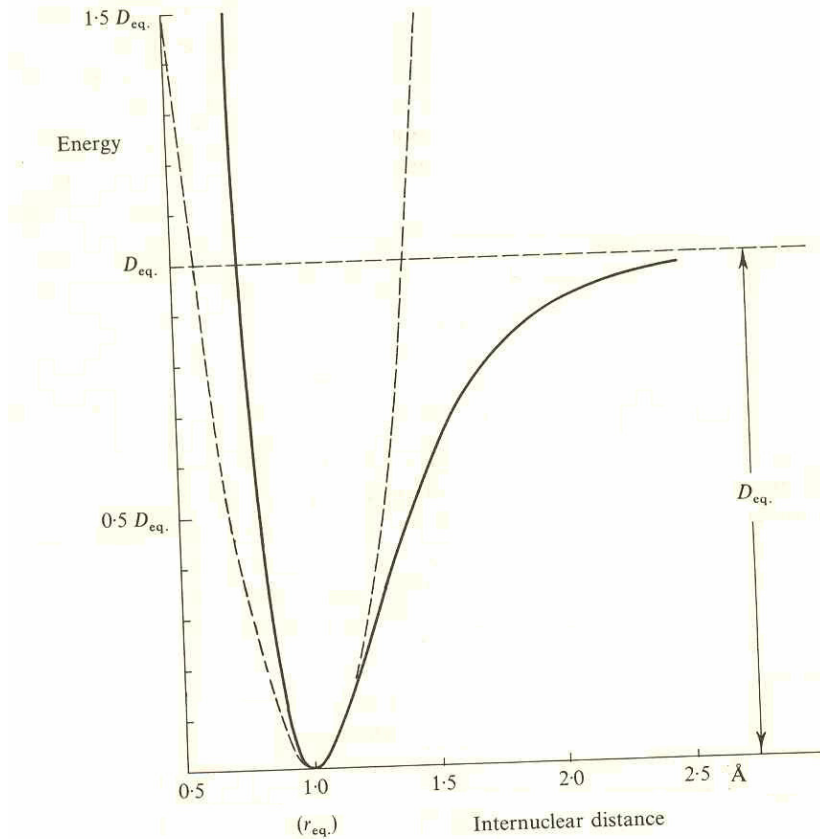
Figure B.3: The Morse curve, the energy of a diatomic molecule undergoing anharmonic vibrations.

Unfortunately, real molecules do not obey the laws of simple harmonic motion exactly, rather their motions are anharmonic. For instance, when the atoms are pulled apart, at some point the bond will break. So, only for small compression and extension the bond may be perfectly elastic, for larger amplitudes more complicated behaviour is expected. Figure B.3 shows a more realistic energy curve for a typical diatomic molecule, called the Morse curve, and the ideal simple harmonic parabola as a dashed line.

The Morse curve shown in figure B.3 is approximated by an empirical expression, derived by P.M. Morse [34]. The Morse curve reads

$$E = D_{eq}[1 - \exp\{a(r_{eq} - r)\}]^2. \tag{B.4}$$

In this equation a is a constant for a particular molecule and D_{eq} is the dissociation energy. More accurate description of the curve requires cubic and higher order terms. These higher order terms are only important for large numbers of v, so they are omitted here for simplicity. Two years after Morse, in 1931, sir John Lennard-Jones derived a similar approximation for the attractive (Van der Waals) forces and repulsive (Pauli-repulsion) forces, called the Lennard-Jones potential.
When equation B.4 is used in the Schrödinger equation instead of the previous parabolic shape for the energy curve, the allowed vibrational energy levels can be shown to be

$$\varepsilon_v = (v + \frac{1}{2})\omega_e - (v + \frac{1}{2})^2 \omega_e x_e, \tag{B.5}$$

where v is the vibrational energy level, ω_e is the oscillation frequency [cm^{-1}] and x_e is the corresponding anharmonicity constant, which is always small and positive for bond stretching vibrations. Because of the effect of x_e the vibrational levels become less far apart for increasing v. Equation B.5 for an anharmonic oscillator can be rewritten and compared with the solution for a harmonic oscillator (equation B.3), which gives

$$\omega_{osc} = \omega_e \{1 - x_e (v + \frac{1}{2})\}. \tag{B.6}$$

In this equation ω_e is the equilibrium oscillation frequency for an anharmonic system. This is a hypothetical value, because the vibrational energy level that is required is $v = -1/2$, setting $\varepsilon = 0$ according to equation B.5. It has already been shown that the vibrational energy can not be equal to zero (see equation B.3). Equation B.6 shows that the anharmonic oscillator behaves like a harmonic oscillator, but with an oscillation frequency that decreases steadily with increasing v. Figure B.4 shows the Morse curve again, but now with vibrational energy levels. As can be seen, the energy difference between vibrational levels decreases for increasing v.

Note that equations B.5 and B.6 show that $\omega_0 = \omega_e (1-x_e/2)$ [cm^{-1}] and $\varepsilon_0 = \frac{1}{2} \omega_e (1-x_e/2)$ [cm^{-1}], so the zero-point energy for anharmonic and harmonic oscillators is not exactly the same.
The value of vibrational energy levels differs a lot from the rotational energy levels. For the purpose of understanding absorption spectra it is assumed that a molecule can execute vibrations
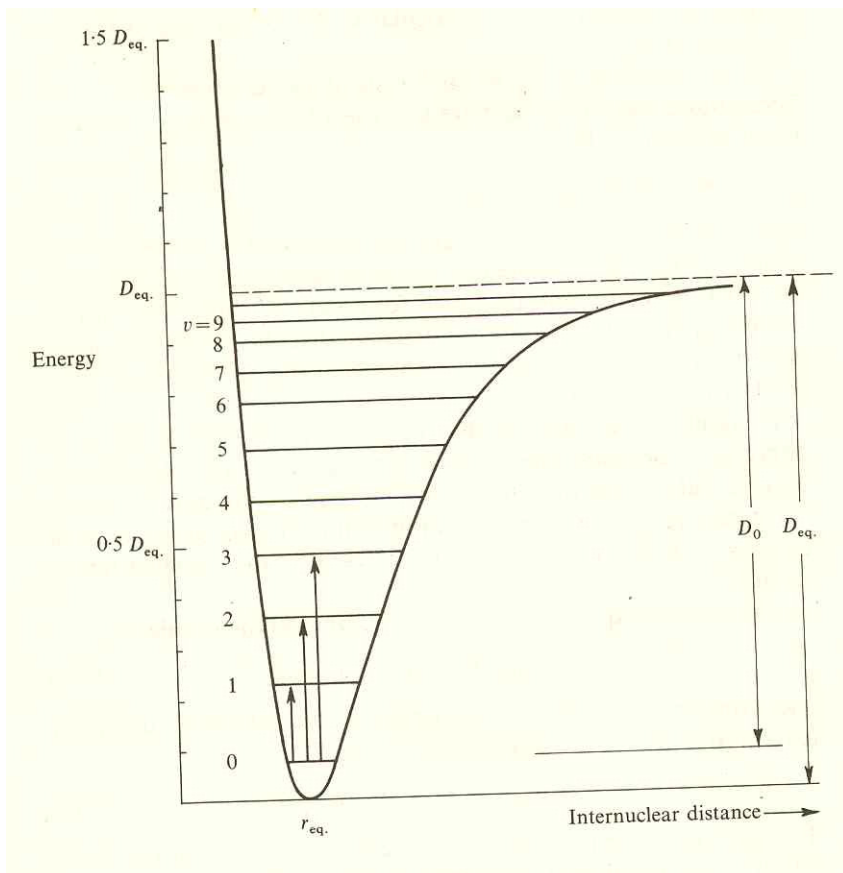

Figure B.4: Allowed vibrational energy levels and for a diatomic molecule undergoing anharmonic oscillations.

and rotations independently, and hence that the combined rotational-vibrational energy of a molecule is equal to the sum of the separate energies. Figure B.5 shows two different vibrational levels (v) of diatomic molecule, and the rotational levels (J) corresponding to these vibrational levels.

The rotational states of the molecule are occupied to varying degrees in any molecular population, which gives rise to different transition intensities. This is shown at the bottom of figure B.6. ω_0 is the vibration frequency corresponding to the ground state, the transitions from the ground vibrational state ($v = 0$) to the first vibrational state ($v = 1$, so $\Delta v = +1$) and from one rotational state to the next higher state ($\Delta J = +1$) are to the right of the ground vibrational frequency and are called the R-branch. Alternatively, the transitions with $\Delta v = +1$ and $\Delta J = -1$ are to the left of ω_0 and are called the P-branch.
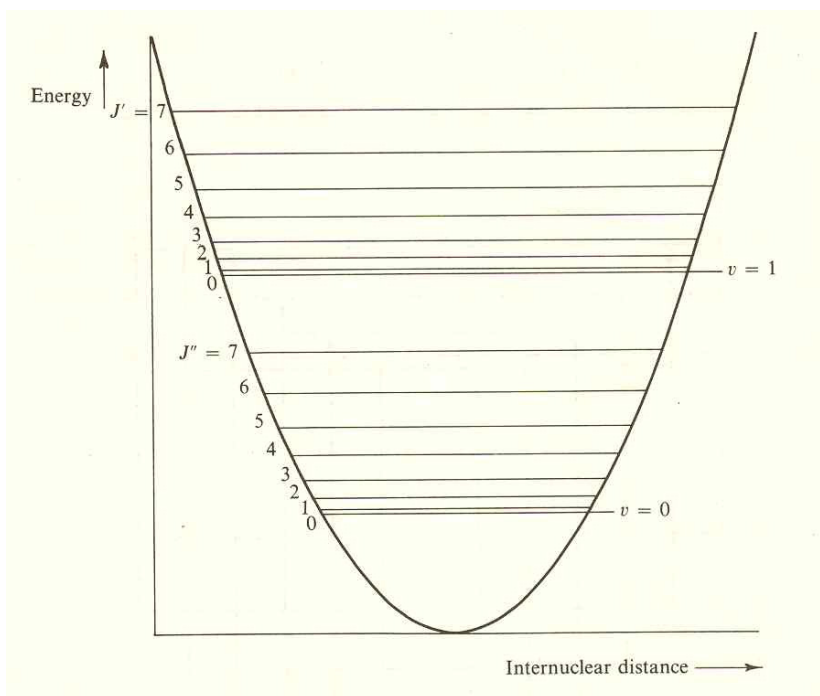

Figure B.5: The rotational energy levels for two different vibrational states for a diatomic molecule undergoing anharmonic oscillations.
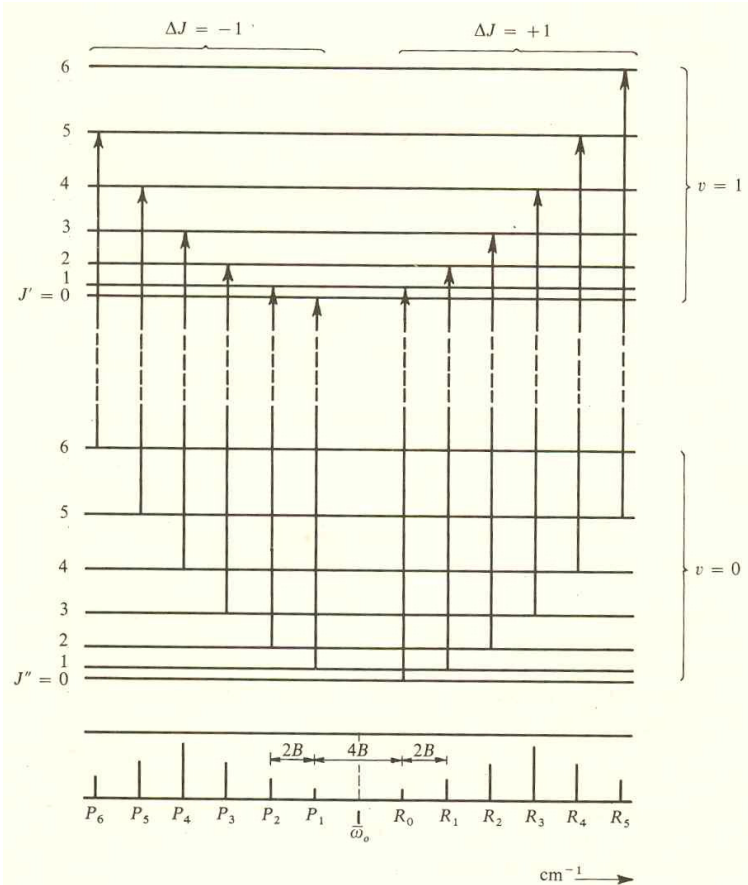
Figure B.6: Transitions between rotational-vibrational energy levels of a diatomic molecule, together with the resulting absorption spectrum depicted at the bottom.

So, the lines on the low frequency side of ω_0 correspond to a lower rotational energy level ($\Delta J = -1$) and are called the P-branch, the lines on the high frequency side of ω_0 correspond to a higher rotational energy level ($\Delta J = +1$) and are called the R-branch. These names seem rather arbitrary, but they are not. When a transition is only caused by a different rotational energy level ($\Delta v \neq 0$, and $\Delta J = 0$) than the resulting absorption band is called the Q branch. For most molecules a change in rotational energy level is accompanied by a change in vibrational energy level, and the two changes can not occur separately, so the Q-branch is not seen very often. Because there is only a change in vibrational energy, all absorption lines are superimposed upon each other, resulting in one very intense absorption line. Figure B.7 shows the Q-branch for HCN. The fact that the Q-branch absorption band is not one peak but shows several partially overlapping each other, and the alternating stronger-weaker absorption lines of P and R branches are caused by the presence of two isotopes of HCN, $^{13}H^{14}CN$ and $^{12}H^{15}CN$, nuclear spin and symmetric top of the molecules. Nuclear spin has an effect on the populations of a molecule in a certain rotational level and thus on the exact position of absorption lines. Symmetric top means that the dipole moment can be changed parallel to or perpendicular to the axis of symmetry of a molecule, resulting in particular distinctive features in an absorption graph.

For this simple example $\Delta v = \pm 1$ was used, but for more complex molecules $\Delta v = 0, \pm 1, \pm 2$ may also exist. The labelling of the line series is than quite consistent, as this table shows.

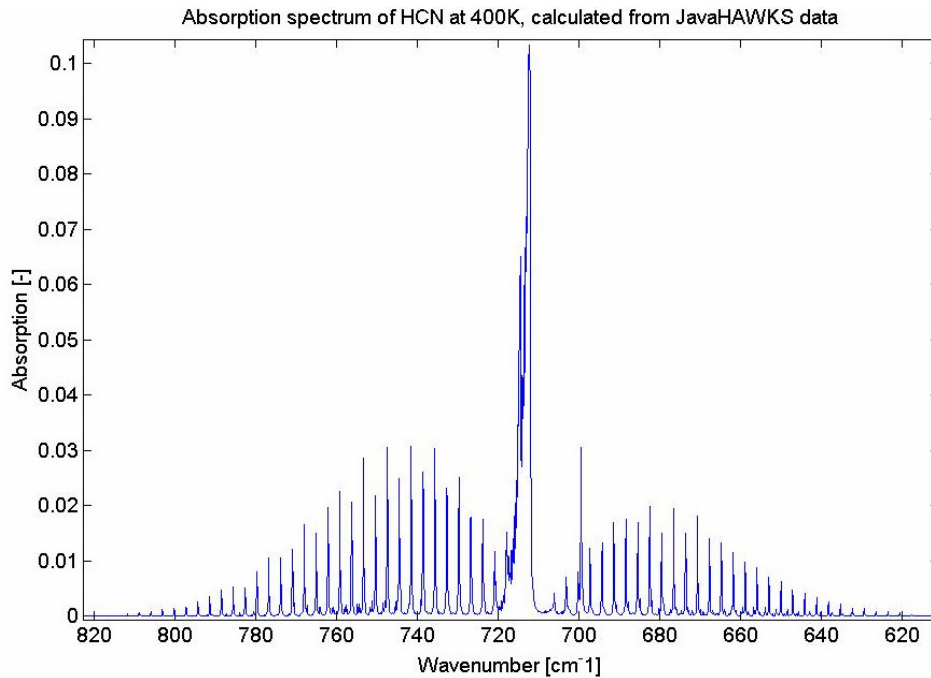| Lines arising from ΔJ	-2	-1	0	+1	+2
Branch name	O	P	Q	R	S

Figure B.7: Absorption spectrum of HCN, created with JavaHAWKS data. The largest absorption peak in the centre of the figure (at 715 cm^{-1}) is called the Q-branch.
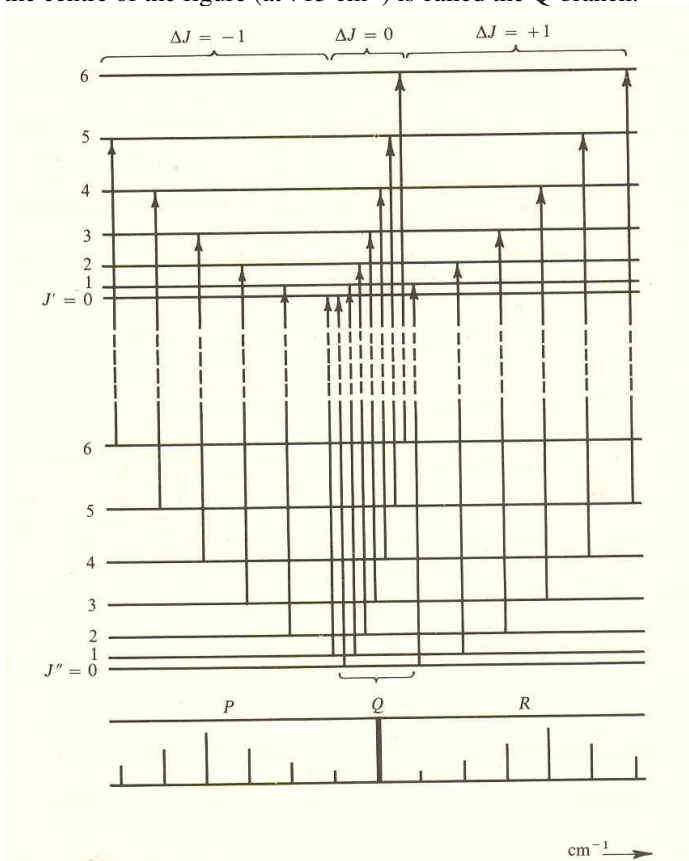

Figure B.8: Rotational energy levels for two vibrational states showing the Q-branch for $\Delta J =0$.
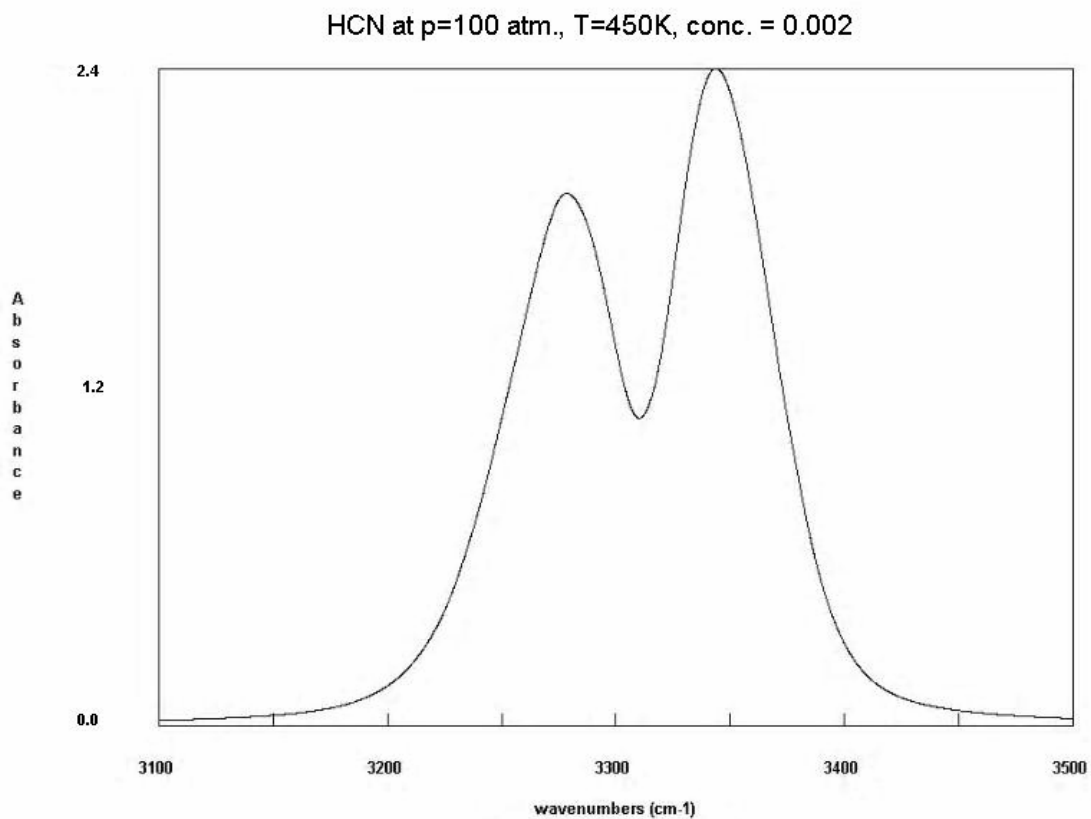
Appendix C   Absorption spectrum of HCN

Figure C.1: Absorption spectrum of hydrogen cyanide at a pressure of 100 atmospheres, a temperature of 450K and a concentration of 0.002, generated with Molspec92. The figure clearly shows that separate absorption lines can no longer be distinguished due to broadening and instead one line connecting the tops of the separate absorption lines is now seen.

Appendix D   Apodization, signal noise and scanning parameters

In principle an FTIR machine obtains an interferogram. By (fast) Fourier transform, this interferogram is changed into a spectral energy graph, showing either absorption or transmittance as a function of wavenumber. At zero path length all waves of the infrared beam interfere constructively, resulting in the so called centerburst as can be seen in figure 3.5. As soon as there is a path length difference (shown on the horizontal axis) the different frequencies in the infrared beam will start to interfere in a destructive way, to a more or lesser degree. With an infinite path length difference the resulting interferogram should show only the centerburst and no other peaks, since there will always be destructive interference between several different wavelengths. However, an infinite path difference is of course not feasible in any real FTIR machine, so instead an interferogram is obtained for a less than infinite path difference and any wobbles in the interferogram are suppressed by multiplying the interferogram with a function. In the following figure a function representing an interferogram is multiplied by such a suppressing function, resulting in suppression of all peaks but the largest one.

The interferogram is multiplied by the function resulting in smaller 'feet' next to the centerburst. Because of the function property that it suppresses these 'feet' the group of functions that is used is called apodization functions, from the Greek α πωδωσ ('a podos', without feet). As figure D.1 shows the highest peak is unchanged in height by the apodization, but the base of the peak is broadened. This also happens when an interferogram is apodized, resulting in loss of spectral resolution. When very fine structure is investigated it is in principle advisable to use an unapodized interferogram.

Most spectroscopists will use the apodized transform of an interferogram because it is much smoother than the unapodized transform and therefore easier to work with. Drawback of using apodization functions though, is that they result in a loss of resolution. To limit this loss of
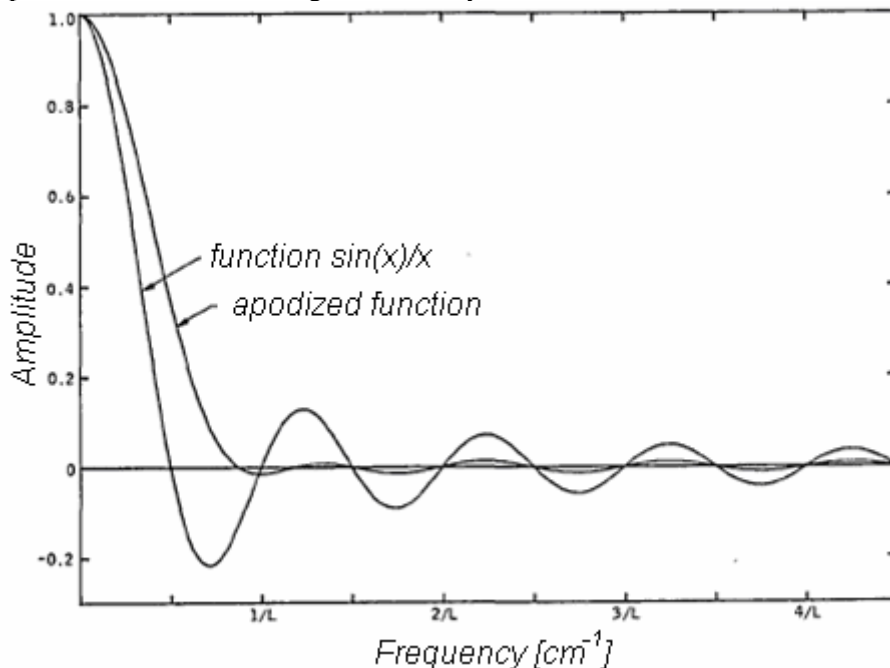

Figure D.1: The original function *sin(x)/x*, and the same function but now after apodization [36].

resolution the choice of apodization function used is very important. Filler and Norton and Beer have done a lot of research in apodization functions in general [35] and finding more suitable apodization functions [36], respectively.

Filler constructed the so-called Filler diagram, shown in figure D.2. On the horizontal axis is set out the half width after apodization, devided by the half width of the *sin(x)/x* (sinc) function. This is denoted by W/W_0. On the vertical axis is set out the absolute size of the largest secondary maximum relative to the sinc function, denoted by h/h_0.

Each V-shape shown in the graph is from one function family where only one parameter is changed. Note that all results are in the upper right corner of the graph, as if there is a boundary that can not be crossed. Norton and Beer verified this result empirically and found three functions, denoted by weak, medium and strong, which are all on or very close to this boundary and may therefore be the best choices in apodizing functions. Figure D.3 shows the location of these functions in the Filler diagram.
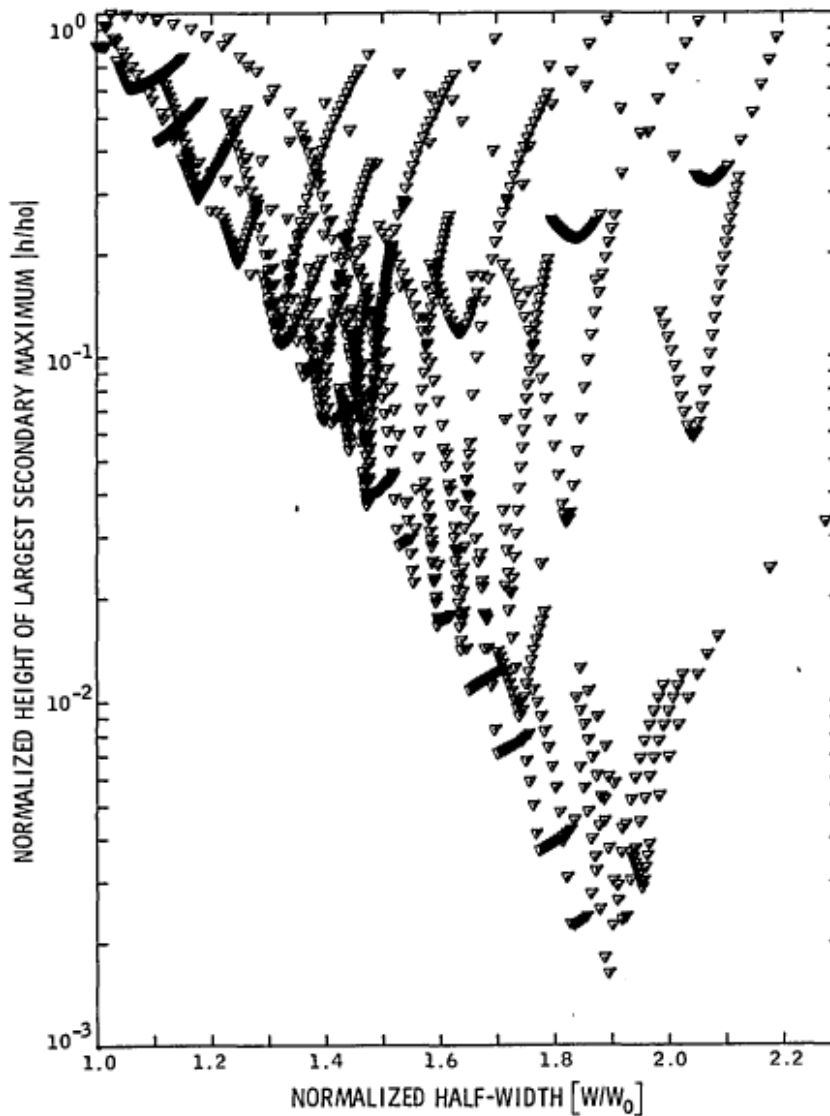

Figure D.2: Filler diagram for about 1150 apodizing functions. Note that larger suppression of the secondary peaks (on vertical axis) results in more peak broadening (horizontal axis) [36].
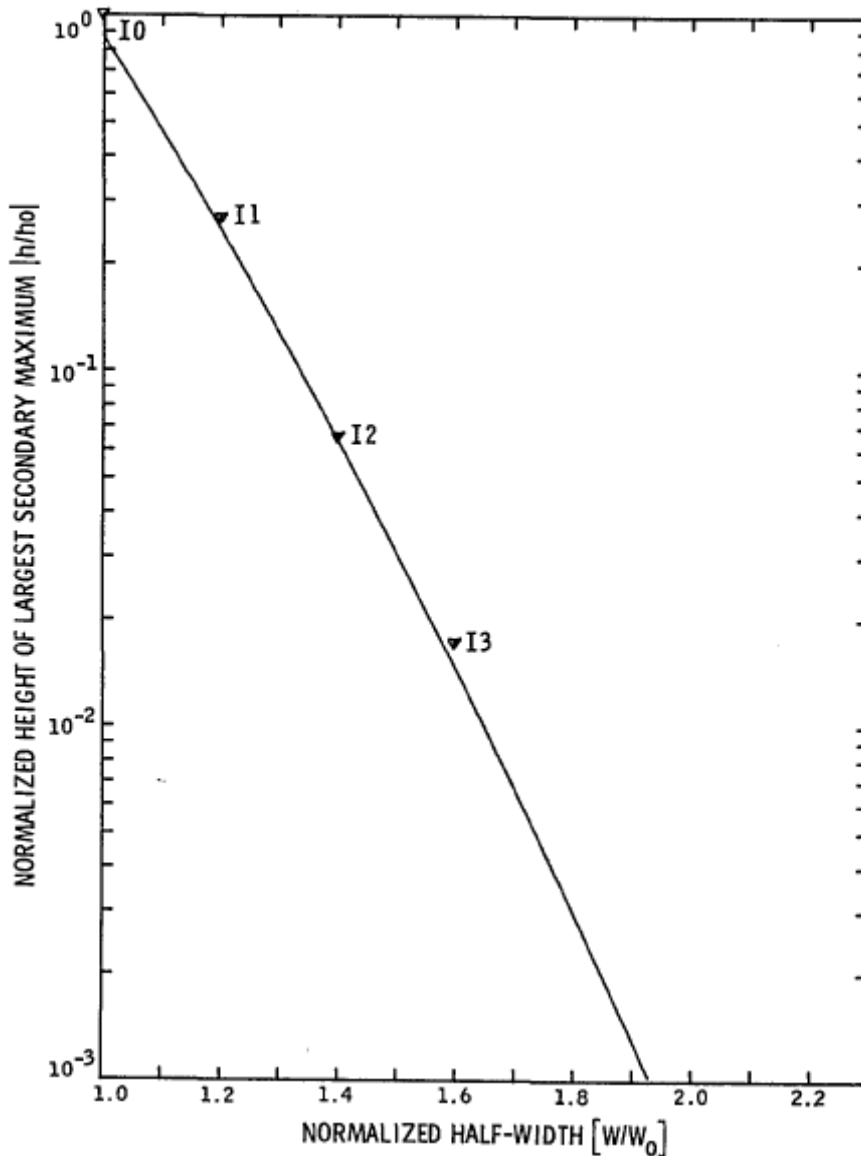
Figure D.3: Filler diagram, indicating the location of the weak (I1), medium (I2) and strong (I3) Norton/Beer apodization functions [36].

The choice in apodization function influences the shape and peak height of the Fourier transform, which is subsequently used for quantitative analysis. Since the quantification takes place on the basis of the peak height of the absorption peaks, the apodization function used should be the one that leaves the highest possible resolution in the graphs. In the following paragraph the scanning settings that were found to be optimal for this machine and this application are treated, including the apodization function that seems to give the best results.

Signal noise and scanning parameters

Whenever a measurement is done the question that should be asked is if the quantity that is measured is the same as what you want to measure. Usually there are sources of noise that offset

the value of interest. The measurements with the FTIR are no different. The most important sources of noise in the FTIR are the translating of the moving mirror in the interferometer and the number of scans made for one measurement. Also, the measurement resolution has an influence on the noise level.

Number of scans
When a measurement is done with the FTIR the number of scans is one of the parameters that need to be specified. What the machine does is make a scan of whatever is in the sample compartment, obtain its interferogram, and finally transform this into an absorption graph. When one measurement is made it is easy to see that there is a lot of noise on the signal, since the graph looks like a sine wave along some mean value. When the number of scans is increased, this spread around a mean value decreases, as can be seen in figure D.4. This can be explained by taking the signal s that is measured as being composed of the actual value v_a that needs to be measured and noise n in the signal,

$$s = v_a + n. \tag{D.1}$$

The sign of the noise n can be positive or negative. This means that when more measurements are added together and divided by the number of measurements, the noise can cancel itself out and what remains is the (mean) value of the signal, which is the value of interest.
The spread of signal values around a mean value is called standard deviation and can be defined as

$$s = \frac{1}{N} \sum_{i=1}^{N} \sqrt{(x_i - \bar{x})^2} \ . \tag{D.2}$$

In the above equation N is the number of measurements, x_i is one of the measured values and $\bar{x}$ is the mean value of the measurements. The value $1/N$ is a constant and can be placed underneath the square root sign. It is than easy to see that the standard deviation (or noise as it can be
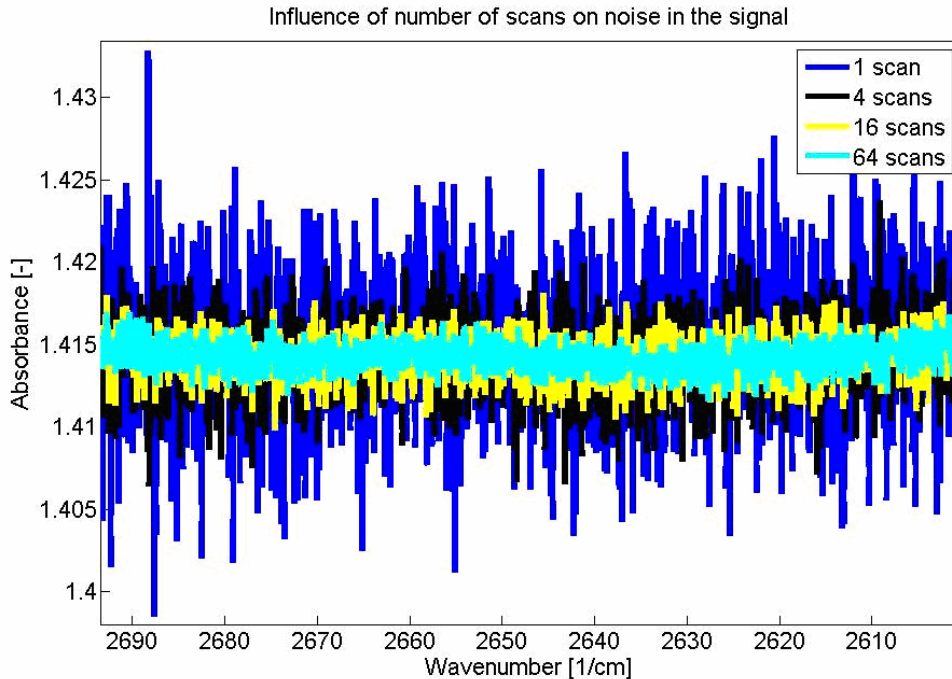

Figure D.4: Measured signal for several different number of scans.

considered here) is proportional to the inverse of the square root of the number of measurements. An illustration of this can be seen in the figure D.4. It shows the signal that is measured with the FTIR and it is clear from the graph that the noise reduces with increasing number of scans. In fact the relationship that the noise reduces by $\sqrt{1/N}$ can be seen. The blue line shows a part of the spectrum measured with one scan. The standard deviation is approximately 0.01. Next is the spectrum measured with four scans, which means the standard deviation should be $\sqrt{1/4} = 1/2$ of that of the spectrum measured with one scan. The standard deviation turns out to be approximately 0.005, which is indeed half of that of the spectrum with one scan. Similarly, the spectrum with 16 scans shows a standard deviation of approximately one quarter, and the spectrum of 64 scan approximately one eighth of the standard deviation of the measurement with one scan.

So, for a measurement to be as accurate as possible, the number of scans needs to be as high as possible. Measurements have been done with 16 scans, which gave good results. However, it takes this FTIR about five minutes to do one measurement with 16 scans. From experiments it is known that, for yet unknown reason, the ammonia concentration decreases in time. In order to prevent too much loss of ammonia the number of scans that are averaged needs to be limited. This means that only 4 scans will be averaged for one measurement. As will be clarified in the next paragraph this is not a very big drawback.

Mirror velocity

As mentioned in paragraph 3.2, the FTIR houses an interferometer which has a moving mirror for modulating the IR beam. The distance this mirror moves is always the same, so naturally a measurement can be done in less time when the mirror translates faster. However, increasing the mirror velocity, also called optical path difference velocity or OPD velocity, creates more vibrations in the mirror and thus more noise in the signal that is being measured. Trial and error have shown that the amount of noise created by vibrations of the moving mirror is much larger than the noise from taking fewer scans. Therefore choosing a small OPD velocity is more important than taking more scans. In figure D.5 the effect of different mirror velocities is shown.

As can be seen in the figure, the noise in the measurement with a mirror velocity of 5.0 cm/s is very high. There is even so much noise, that features like the small crests in the figure around 2950 cm^{-1} are hardly distinguishable. As expected, with decreasing mirror velocity the noise in the signal also decreases. The difference between 0.1 and 0.2 cm/s is very small, so the 'fastest' of these two is chosen for the measurements: 0.2 cm/s.
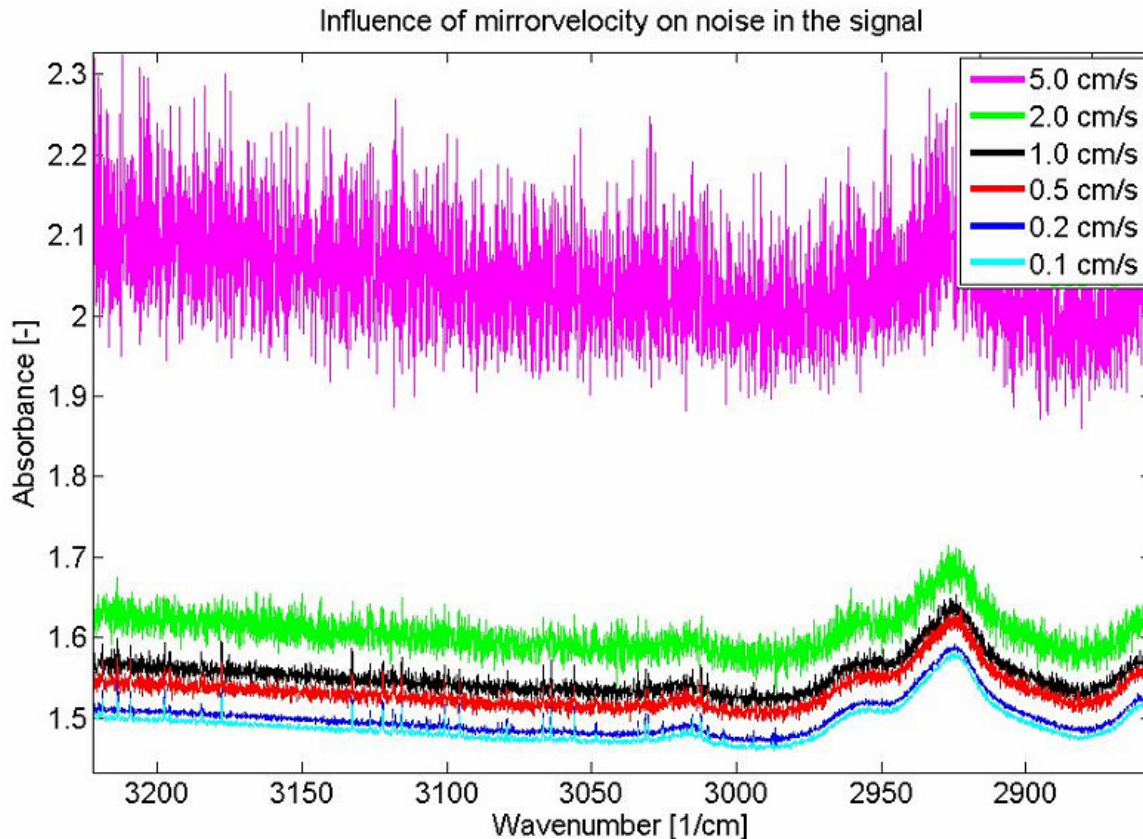
Figure D.5: Influence of mirror velocity on signal noise.

Apodization function

The apodization function has already been explained at the beginning of this paragraph. In general there may be no such thing as the best apodization function for all purpose use. However, for this specific application it should be able to find one. In the Spectrum software that comes with the PerkinElmer FTIR that is used in these measurements there are eight different apodization functions available, namely: boxcar, Norton-Beer (NB) weak, NB medium, NB strong, triangular, raised cosine, Kaiser-Bessel and Filler. Figure D.6 shows all these. The Kaiser-Bessel function is probably best for suppressing the side lobes of an interferogram. However, the peaks this function produces are also among the lowest of these functions. The boxcar function doesn't suppress the side lobes very well, but shows the highest peaks and the highest resolution, since the peaks are hardly broadened by this function. This can be seen in figure D.6 and table D.1 which contains data from the Spectrum GX FT-IR User's Guide. Because the spectra that are measured will be used for accurate quantification of ammonia concentration it is important that the peaks are as distinct and as high as possible. This is achieved with the boxcar apodization function, so this function will be used for the measurements.
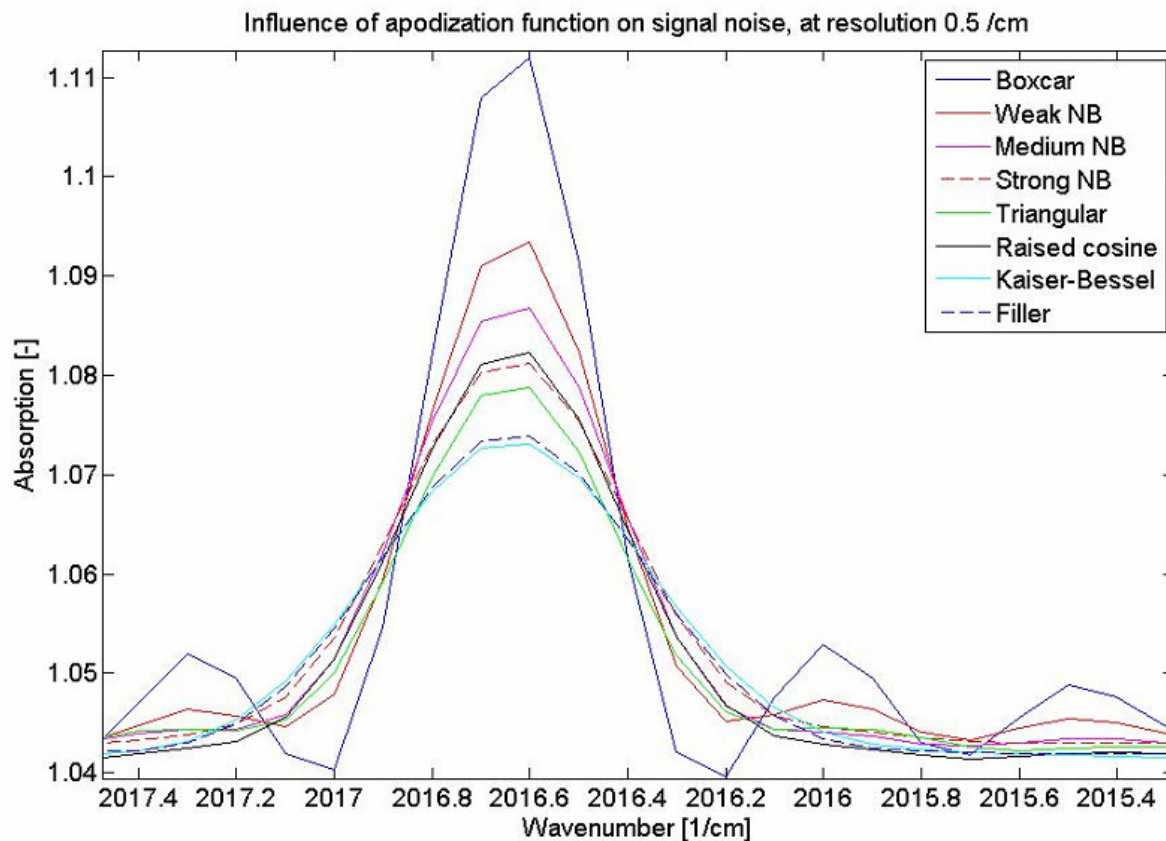
Figure D.6: Influence of apodization function on peak height.

Table D.1: Data on the available apodization functions, for Spectrum User's Guide.

Function name	Relative width	Largest sidelobe	Feature
Boxcar	0.603	0.217	Best resolution
Weak	0.724	0.058	Good resolution
Medium	0.844	0.014	General purpose
Raised cosine	0.907	0.0073	General purpose
Strong	0.965	0.0037	General purpose
Kaiser-Bessel	1.19	0.0005	High accuracy
Triangle	0.885	0.047	Good convergence
Filler	1.16	0.0009	High accuracy and convergence

Resolution

Another source for faulty measurements is the resolution used for the measurements. The resolution is determined by the J-stop of the FTIR and should, theoretically, be as low as possible when the spectra of gases are being measured, because gases have very distinct and narrow absorption lines. The lowest possible resolution that the available FTIR can measure with is 0.2 cm^{-1}. For greater values of resolution distinct features of the spectrum may be lost, as can be seen in figure D.7. Unfortunately, at the lowest value of the resolution the signal noise is relatively large too. Another drawback of the lowest resolution of 0.2 cm^{-1} is that it is no longer possible to use the 'align' function in the FTIR software. This may be caused by the J-stop size now being so small that the amount of radiation that goes through is very small, and the detector can not detect
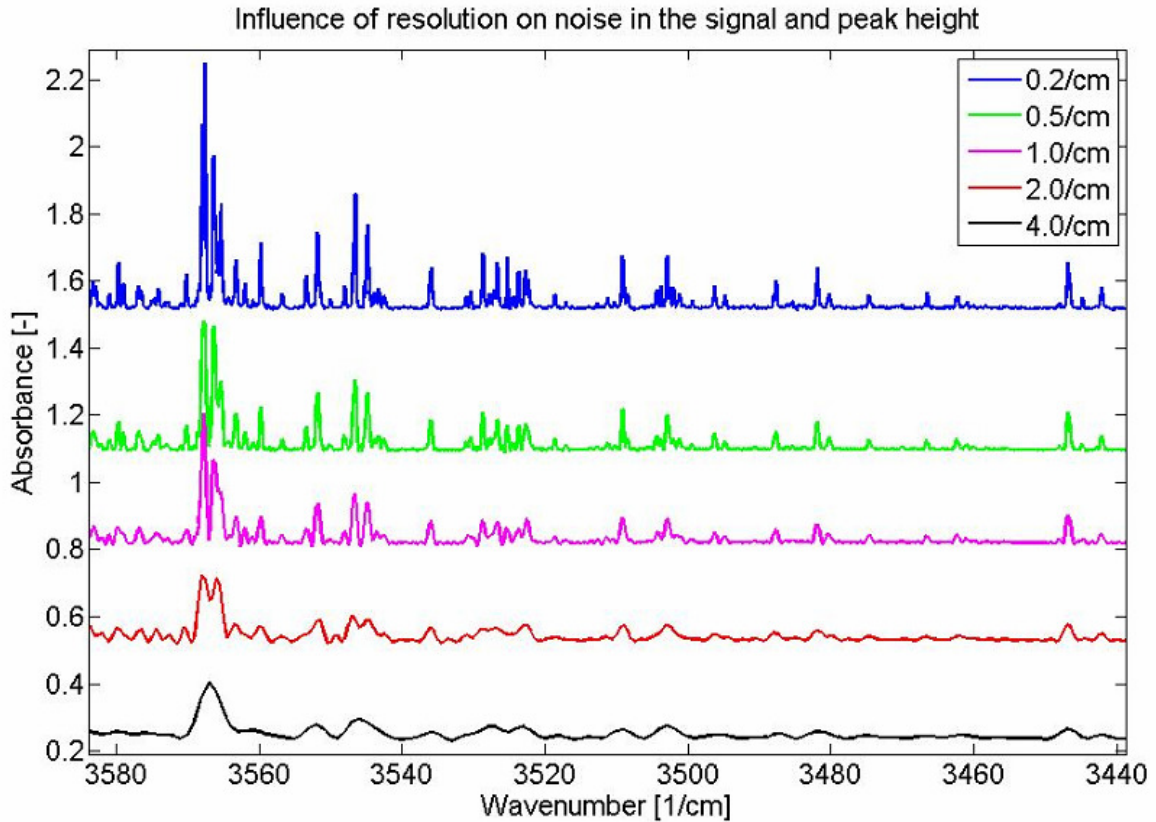
Figure D.6: Influence of resolution on measurements.

the small differences in energy level before and after aligning. Because there are moving parts in the FTIR it is necessary to align all the optical components before every measurement, thus ensuring that the starting point for a measurement is always the same. The optimal resolution is found to be 0.5 cm^{-1}.

Concluding

Summing up this section, the measurements done in Eindhoven were conducted with a resolution of 0.5 cm^{-1}, an OPD velocity of 0.2 cm/s, averaging over 4 scans and using the boxcar apodization function.

Appendix E   Spectral manipulation

After the sometimes tedious work of obtaining an absorption spectrum most software will have several options for manipulating the spectra, such as spectral subtraction, baseline correction, smoothing and deconvolution.

Spectral subtraction is a convenient tool for obtaining the spectrum of a component in a mixture. For example, when a test set up using a gas cell is ready for use, first the spectrum of the background is obtained. The background spectrum now quantifies the influence of all factors that contribute to a spectrum, such as the presence of certain species in the background (e.g. atmospheric water vapour and carbon dioxide, see figure (E.1)), windows that the IR beam passes through, etc. Basically the background spectrum is the spectrum of everything except the sample of interest. Than, the spectrum of an unknown gas is taken. By subtraction of the background spectrum from the sample spectrum, a spectrum of only the sample is obtained, without the influence of the background. This spectrum is much easier to analyse, and certain features that were previously almost invisible can now more easily be seen.

Another feature which can be helpful at times is the baseline correction. Due to sample scattering, inappropriately chosen background or instrument drift the baseline of a spectrum may be sloping or curved. The baseline can be adjusted such that it becomes flat again, however this is not without risk, because if the correction is not done properly spectral artefacts are introduced which may lead to incorrect interpretation.
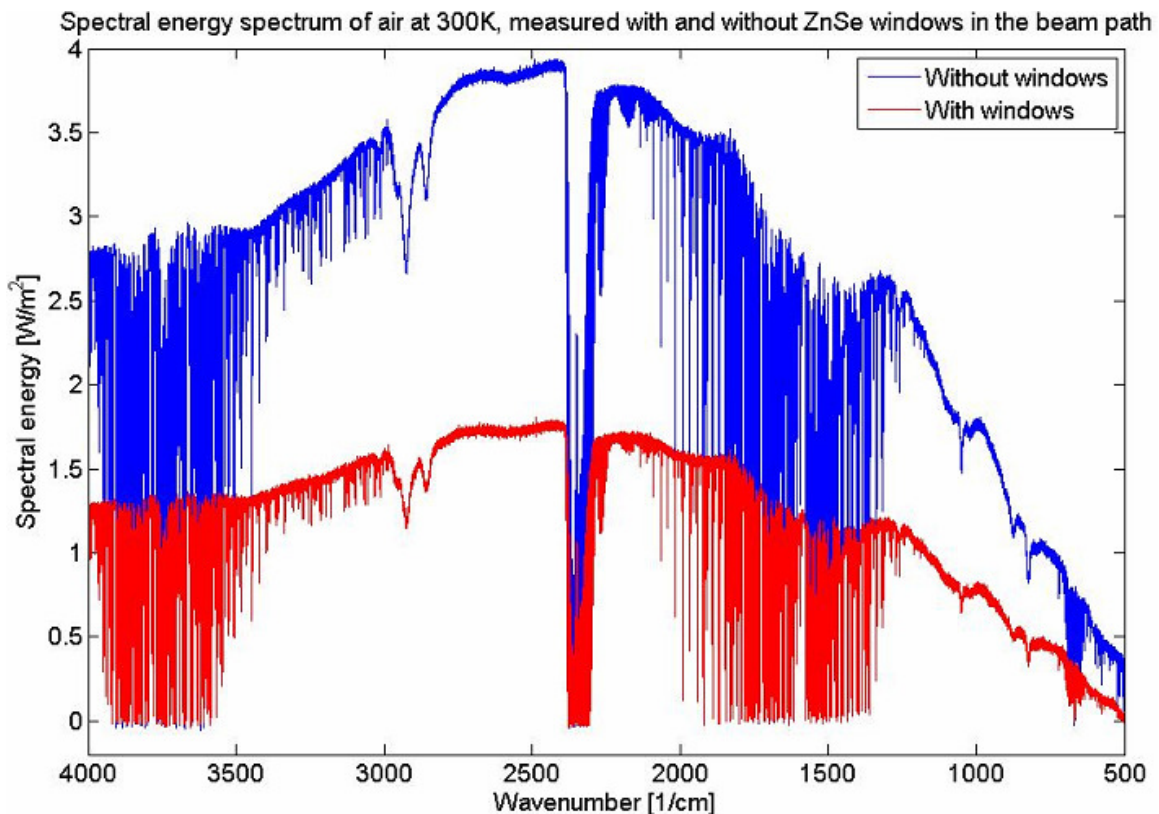

Figure E.1: Background spectrum in air. The absorption bands around 1500 and 3700 cm^{-1} are caused by water vapour, the band at 2400 cm^{-1} is caused by carbon dioxide. The shape of the spectrum is influenced by all obstacles in the beam's path, such as in this case the KBr beam splitter and the ZnSe windows of the reactor, or the lack thereof.

Smoothing can be used to reduce the noise in noisy spectra, thus uncovering features that were previously hidden under the noise. There are several methods to do this, but all use some form of averaging to reduce the noise. Because noise can have positive and negative values with respect to the actual signal, averaging will cancel out most of the noise. The same averaging that reduces the noise in a spectrum also reduces the resolution. This is a natural outcome of the averaging process, and this renders smoothing is therefore unsuitable for quantitative analysis.

Deconvolution is a helpful tool which mathematically enhances the resolution of a spectrum. It is particularly helpful when several narrower bands overlap to form one broad band, for example in case of an unknown gas mixture. Deconvolution can help to determine the number and positions of overlapped bands. In the deconvolution process peak height information is retained, but peak areas and peak shapes are altered, so deconvolution too should not be used on a spectrum which is used for quantitative analysis.

Concluding, when working with standards and unknown gases of which the concentration of a certain species needs to be determined, avoid spectral manipulation (except subtraction). Manipulation of one of the spectra is difficult to reproduce on the other spectra, and the result will no longer be suitable for quantitative analysis.

Appendix F   Quick JavaHAWKS manual

The software package JavaHAWKS is a programme that is used to perform basic operations, such as filtering by means of frequency, molecule, isotope, band system, etc. on the HITRAN molecular spectroscopic database. JavaHAWKS is also used for plotting the line-by-line or cross-section data, and for various other database management functions. It can be downloaded from the Harvard University website, see [17] for instructions.

Using JavaHAWKS is easy and straightforward. After installation of the HITRAN data file and the JavaHAWKS software on a computer, JavaHAWKS can be started up. Of the seven menus in the start up window, only two are important for novel users: Select and Plot (and possibly Help). By clicking Select a pop up menu appears, for this option showing only *Select*. Click this option and the HAWKS Select dialog appears. In this dialog all input concerning the species and its conditions can be given.

First of all, check whether the programme uses the correct input data file (this needs to be done only the first time). Click *HITRAN Filename* in the Set Filenames menu. In the now appearing Select HITRAN Format Input File dialog choose the first option, *HITRAN File From Local Computer*. Click on the *Select a local file* button to see which file is used now and to change this file. For the 2004 edition of JavaHAWKS this data file should be HITRAN04.par

Now that the data file is chosen the scoll menu in the Set Filenames menu can be used to specify what type of file the programme should create. Choose *Hitran Output* (*.out) when the results will only be used and visualised using JavaHAWKS. When *Comma sep Output* (*.csp) is chosen a comma separated output file is created which can not be visualised by JavaHAWKS, but can more easily be used by, for instance, Matlab. Be aware that of the *.csp file only the 3rd through 10th column contain important data to be used in Matlab (see paragraph 3.4), so the other columns (which do not always have the same number of rows, which is a problem for Matlab) can be deleted before using these files in Matlab. When option *Both* is chosen in the scroll menu both *.out and *.csp files are created.

Next, click the *Output Filename* button to specify the output file name of the files that JavaHAWKS will create. Make sure to add the .out and/or .csp extensions to the file name, otherwise the files are not usable.

Now that the output file names have been specified, the parameters for the simulation can be set. In the Selection Parameters menu click the *Spectral Range* button to specify the range of wavenumbers for which the simulation needs to be done. Choose a large range when the results are not yet known, for better graphs a smaller range is probably clearer. Smaller wavenumber range graphs can be plotted at a later time. There is a *Toggle Wavenumber to Wavelength* button in case the exact wavenumbers/lengths for the range are not known but the wavelengths/numbers are.

With the *Molecule* button in the Selection Parameters menu the molecule for which the simulation should be run can be chosen. The 2004 edition has 39 molecules to choose from, see [17]. Make sure to choose only one molecule if the output file is going to be used for further calculations, since the values in the output file are not separated into the different molecules any more.

With the *Isotopologue* button in the Selection Parameters menu the different isotopes that are found in nature and their percentages of the entire amount of molecule that is chosen are stated. This button need not be used.

With the *Temperature* button in the Selection Parameters menu the simulation temperature of the gas can be set. This is important because at different temperatures the distribution of states of the molecule will also be different, thus causing a different absorption spectrum, as mentioned in paragraph 3.1.

The *Band* and *Cutoff* buttons in the Selection Parameters menu can be used to select specific absorption bands and intensity cut-off, respectively. These buttons have not been used.

All parameters that JavaHAWKS needs to run the simulation have now been given, so the *Run Select* button can be pressed. A HAWKS Run Select Info pop up will appear, summarising all the parameters that have been set and their values. A message will appear at the bottom of this window if the specified output file name already exists. Clicking the OK button will start the calculation.

Plotting the *.out files

As mentioned before, JavaHAWKS can only plot the *.out files. This can be done in the following way.

After a simulation finishes, click the *Cancel* button of the HAWKS select menu and close the *HAWKS - selecting* window that showed the progress of the calculation. In the JavaHAWKS start up window click the Plot menu and choose the *Plot Line by Line* option. In the following *Select New Plot* menu several options for plotting a file are given.

First, in the Select Parameters menu click *Select File to Plot*. In the following Select HITRAN Format Plot File pop-up window choose the first option, *HITRAN Format File From Local Computer* and click the *Select a local file* button. If the file that is shown in the next pop up window is the file that you want to plot, simply click *Yes*. If this is not the file you want to plot, click *No* and a browse window appears from which the file can be chosen.

After choosing the file to plot, the *X-Axis* and *Y-Axis* buttons can be used to change the default Auto Scale function. This is usually not necessary, but may be convenient when from a larger wavenumber range a particular area of interest needs closer examination. Remember that JavaHAWKS uses quantum mechanic calculations for most of its results, so very fine lines can be found in the spectral intensity plots (wavenumbers specified with up to five decimal numbers). The *Difference Plot* button has not been used.

In the Select Plot menu several options are available of what should be shown in the plots. For absorbance plots it's informative to look at the intensity plots. Click the *Intensity* button when x-axis and y-axis values have been set, or choose *Intensity-Entire Range* button when the entire range of the simulation needs to be shown. A pop up window appears showing the spectral intensity graph for the specified options.
The buttons shown in the Select Plot menu for the other parameters have not been used.

Even though the spectral intensity graphs from JavaHAWKS are not yet absorbance graphs, the position of the lines does not change very much, so for an indication of where to expect the absorption lines these plots are probably good enough.

Appendix G — Calculating absorbance spectra under non-LTE conditions.

Under non-LTE conditions the partition of population between states no longer follows the Boltzmann statistics and equations 3.16 are no longer valid. The line intensities under these conditions may be obtained directly from the weighted transition-moment squared $Я_{\eta\eta'}$ [18] or by correcting the HITRAN calculated intensity $S_{\eta\eta'}(T_{ref})$ [20]. The latter method is described here.

Radiative transfer theory for two levels of vibrational-rotational transition defines the general molecular absorption coefficient $\kappa(v)$ as

$$\kappa(v) = \frac{B_{\eta\eta'}}{Nc}\left(n_\eta - n_{\eta'}\frac{g_\eta}{g_{\eta'}}\right),$$

(G.1)

with $B_{\eta\eta'}$ [cm^3/(ergs s^2)] the Einstein coefficient of induced absorption, N is the molecular number density [cm^{-3}], c the speed of light [cm/s], n_η and $n_{\eta'}$ [cm^{-3}] are the populations of the lower and upper states respectively, g_η and $g_{\eta'}$ [-] are the state statistical weights (including electronic, vibrational, rotational and nuclear statistics).

Under conditions of LTE, the Boltzmann factor Γ gives the ratio between populations in lower and upper levels at the layer kinetic temperature T_K,

$$\Gamma = \frac{\overline{n_2}g_1}{\overline{n_1}g_2} = \exp(-hcv/kT_K),$$

(G.2)

where the overbar indicates the quantity in LTE. Now, the absorption coefficient of a transition can be related to it's LTE value by a factor $\alpha(v)$, by

$$\alpha(v) = \frac{\kappa(v)}{\overline{\kappa}(v)} = f_q\frac{n_1}{\overline{n_1}}\frac{\left(1-\frac{n_2 g_1}{n_1 g_2}\right)}{(1-\exp(-hcv/kT_K))} = f_q r_1\left[\frac{1-\Gamma r_1/r_2}{1-\Gamma}\right].$$

(G.3)

In (G.3) $r_1 = n_1/\overline{n_1}$ and $r_2 = n_2/\overline{n_2}$, and factor f_q account for the departure from LTE of the transition. Factors r_1 and r_2 are used to calculate the non-LTE populations of lower and upper state of the transition, and the quantity in brackets on the far right side of (G.3) stands for the effect of non-LTE due to stimulated emission. Under LTE conditions $\alpha(v)$, r_1 and r_2 are all unity.

Similarly, the radiative transfer equation for the non-LTE situation can be written as

$$I(v)_l = I(v)_{l-1}\exp\left(-\sum_{ij}\alpha(v)_{l,ij}\,\overline{\kappa}(v)_{l,ij}\,u_{l,j}\right) + \beta(v)_l\,B(v,T_{Kl})\left[1-\exp\left(-\sum_{ij}\alpha(v)_{l,ij}\,\overline{\kappa}(v)_{l,ij}\,u_{l,j}\right)\right]$$

(G.4)

with

$$\beta(\nu)_l = \frac{\sum\limits_{ij} r_{2l,ij}\,\overline{\kappa}(\nu)_{l,ij}\,u_{l,j}}{\sum\limits_{ij} \alpha(\nu)_{l,ij}\,\overline{\kappa}(\nu)_{l,ij}\,u_{l,j}} \; . \tag{G.5}$$

In (G.5) the sum in the numerator accounts for the change in the source term $B(\nu,T_K)$ due to non-LTE effects, and the sum in the denominator accounts for the corresponding change in layer opacity. Thus the no-LTE situation of radiative heat transfer is related to the LTE case by two factors, $\alpha(\upsilon)$ and $\beta(\upsilon)_l$.

Appendix H   Welding thermocouples to the grid

In the gridreactor that is used for this project a thermocouple is used to measure the grid temperature. This thermocouple needs to be fixed to the grid, and considering the high temperatures involved, the only means for this is by welding. Previously, when a thermocouple had to be welded to a grid, the thermocouple and grid were taken to the communal technical service GTD of the TU/e. Drawback of this procedure is that GTD building and the thermo fluid dynamics (TFE) laboratory are a little distance apart, and most importantly that it usually takes a couple of days before the grid is ready.

After some closer inquiry it turned out that the workshop of the TFE laboratory also owns a point welding machine, namely a Messer Griesheim PECO Typ 1. With another apparatus also present there the thermocouples themselves could be made and then welded to the grid with the point welder. Mister Henry Vliegen has done the welding for this project. The machine settings are discussed next.

At the top of the machine there is a knob with which the pressure on the electrode, needed to initiate the welding, can be set. Since welding of thermocouples is a rather delicate job, this pressure knob was set to 2, see picture H.1 for a schematic representation of the machine. The other settings used for the machine for welding 0.2 mm diameter platinum/platinum-rhodium wire to a stainless steel grid, using electrodes with a contact diameter of 3 mm, are

Table H.1: Point welding settings for 0.2 mm diameter Pt, Pt-Rh10% wire (S-type thermocouple) to stainlees steel grid.

Stromzeit per.	½
Leistung	6
Sek. Spannung	0,75

For other materials and wire diameters other setting will be necessary, these are easily obtained by trial and error. On the next page the settings for K-type thermocouples can be found.
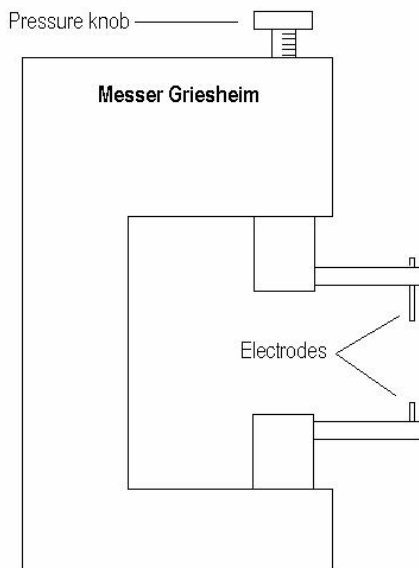

Figure H.1: Schematic representation of the point welding machine of the TFE workshop, with spring pressure knob indicated.
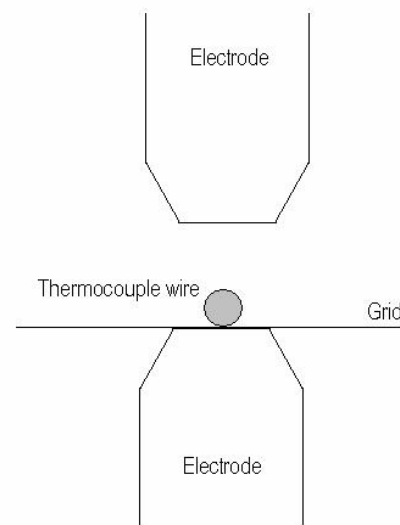
Figure H.2: Close up of electrodes, with grid and thermocouple wire in place.

The first test for determining the point welding settings were done with S-type thermocouple because this wire was available at the workshop of the TFE laboratory. The settings and hardware that is used in the test set up however is suitable for K-type thermocouples. The thermocouple wires for K-type thermocouples are made from Alumel and Chromeland have a measurement error of approximately 0.75% [37]. Chromel is an alloy, consisting of 90% Ni (nickel) and 10% Cr (chrome) and is the positive potential part of the thermocouple. Alumel is an alloy consisting of 95% Ni (nickel), 2% Mn (manganese), 2% Al (aluminium) and 1% other, and is the negative potential part of the thermocouple. For welding a K-type thermocouple to a stainless steel grid the pressure knob is set to 3, and the other settings are

Table H.2: Point welding settings for 0.2 mm diameter Alumel/Chromel wire to stainless steel grid.

Stromzeit per.	1
Leistung	10
Sek. Spannung	0,75

For welding a K-type thermocouple (Chromel/Alumel) to a platina grid the pressure knob is set to 2, and the other settings are similar to table H.2.

The point welding electrodes of 3 mm contact diameter have not been changed (see figure 2).

Grid material

The grid material commonly used is stainless steel. This grid has a wire thickness of 40 μm and an interstice distance of 62 μm (this is commonly used for screen printing). Alternatively platina can be used, but the available grid is less fine with a wire thickness of about 90 μm and an interstice distance of about 225 μm. From the same company a wire mesh made of NiChroom, called Haynes 25 alloy, can also be purchased. This has properties similar to stainless steel, except that it is better resistant to higher temperatures, up to about 1000$^{\text{O}}$C.

A company that specializes in fine grids is

Metaalgaasweverij BV
Anholtseweg 10
7090 AA   Dinxperloo
Tel.   0315 659800

Appendix I Keithley card specifications

The readings that are necessary to operate the power source are done by a Keithley module, the KUSB_3108. The measured temperature values are used in the control loop of the grid, and since the grid needs to reach a certain set temperature really quickly, typically within 1 second, the sampling rate needs to be very high. The KUSB_3108 has the following key features (from the KUSB_3108 manual, [38]):

Table I.1: Key Features

Module	# of Analog Inputs	Sample Rate	# of Analog Outputs	# of DIO Lines	# of Counter/ Timers
KUSB-3108	16 single-ended/ 8 differential/ or 7 thermocouples and 1 CJC	50 kS/s	2	8 in, 8 out	2

The KUSB-3108 provides input gains of 1, 10, 100, and 500 to support thermocouples and low-level analog input capability.
Further more, it has the following major features:
• USB compatibility;
• Software configurable termination resistance for differential
inputs on a channel-by-channel basis.
• Continuously paced and triggered scan capability;
• A 32-location channel-gain list that supports sampling analog
input channels at the same or different gains in sequential or
random order;
• Internal and external clock sources for the analog input
subsystem;

• Digital TTL triggering for the analog input subsystem;
• One 8-bit digital input port and one 8-bit digital output port; the
digital input lines can be included as part of the analog input
channel-gain list to correlate the timing of analog and digital
events; digital outputs can drive external solid-state relays; and
• One dynamic digital output line;
• Two 16-bit user counter/timers programmable for event
counting, frequency measurement, rate generation (continuous
pulse output), one-shot, and repetitive-one shot pulse output
operations.
• Programmable gate types and pulse output types.
• Software calibration for the analog I/O subsystems.